

# **Low temperature electroplating for highly conformal x-ray phase contrast gratings**

Zur Erlangung des akademischen Grades  
**Doktor der Ingenieurwissenschaften**  
der Fakultät für Maschinenbau  
Karlsruher Institut für Technologie (KIT)

genehmigte  
**Dissertation**

von

Dipl.-Ing. Maximilian Amberger

Tag der mündlichen Prüfung: 09. Januar 2018  
Referent: Prof. Dr. Jan Korvink  
Korreferent: Prof. Dr. Jost Göttert



---

*“It’s still magic even if you know how it’s done.”*

Terry Pratchett

# 1 Kurzfassung

Die Röntgen-Phasenkontrastbildgebung gilt als vielversprechender Zweig der medizinischen Bildgebung, der hohe Auflösung mit hervorragendem Weichgewebekontrast kombiniert. Die dafür notwendigen Röntgengitter gehen an die Grenze dessen, was derzeit als Aspektverhältnis und lateraler Auflösung durch das LIGA Verfahren hergestellt werden kann. Diese fragilen Resiststrukturen stellen aber neue Anforderungen an die Galvanik. Das thermische Budget der noch nicht metallisierten Strukturen ist sehr gering, so dass ein neues Gold Galvanikbad für eine noch präzisere Fertigung notwendig wird.

Dazu wird ein neues Sulfid- basiertes Gold-Galvanikbad entwickelt, das bei einer Temperatur von 30 °C betrieben wird. Zugprüfungen und thermische Analysen des Resists nach den Fertigungsprozessen zeigen, dass dieser eine höhenabhängige Vernetzung aufweist, die unterschiedliches mechanischen Verhalten von nominell gleich prozessierten Resiststrukturen hervorbringt. Der Vernetzungsgradient baut zudem mechanische Spannungen zwischen Gitter und Substrat ab. Zum ersten Mal kann gezeigt werden, dass bei 50 °C ein Übergang zu plastischem Bruchverhalten eintritt, was die Verformung im Standard Galvanikbad, das bei 55 °C betrieben wird, erklären kann.

Dieses Wissen und das neue Galvanikbad wurden schließlich genutzt, um bisher unerreichte nahezu perfekte Gitterstrukturen ohne jede Verstrebung herzustellen, die bei Testuntersuchungen die höchsten bekannten Signal-zu-Rausch Werte liefern konnten.



## 2 Abstract

X-ray phase contrast imaging is seen as a very promising new approach in medical imaging, combining high spatial resolution with high soft tissue contrast. This method applies x-ray gratings that are produced in a way that both aspect ratio and lateral resolution are at the border of what can be achieved today with x-ray lithography. These highly fragile resist structures then define new requirements to the electroplating environment. Especially the thermal budget of the not metalized structures is exceptionally low, so a new kind of gold electroplating bath was necessary for a more precise fabrication of gratings.

In the wake of this thesis, a new, sulfite based gold electroplating bath is developed which can be operated at a temperature of 30 °C. Additionally it is shown that only a profound knowledge of the lithography - electroplating interface will further help to reach the desired precision in the structures. Therefor investigations on the chemical and mechanical properties of the resist material after lithography are performed. Those illustrate that the resist has a height dependent state of crosslinkage, a possible root cause of grating deformation. It can also be shown that at 50 °C a transition in the mechanical characteristics appears, what could be an explanation for the deformation of samples in the regular electroplating bath operated at 55 °C.

With this knowledge and the new electroplating bath it becomes possible to fabricate nearly perfect gratings. Those do not need any supportive structures and therefor feature previously unreached signal-to-noise ratios in x-ray tube measurements.



# Danksagung

Im Laufe von fast 8 Jahren haben mich sehr viele Kollegen und Freunde bei der Durchführung der Arbeit unterstützt. Ihnen möchte ich hier an dieser Stelle besonders danken.

Zuerst möchte ich mich bei Prof. Jan Korvink und Prof. Jost Göttert für das Referat meiner Arbeit bedanken. Ohne die Hilfe und Zusammenarbeit mit meinem Betreuer, Hr. Dr. Mohr, wäre diese Arbeit ebenfalls nicht denkbar gewesen. Mein herzlicher Dank gilt speziell auch für die Unterstützung nach der Zeit am IMT sowie die kritische, aber immer konstruktive Herangehensweise an die kleinen und größeren Herausforderungen der Dissertation.

Meine beiden Zimmergenossen Johannes Kenntner und Jan Meiser werden mir immer in Erinnerung bleiben. Ohne die Gitterfertigung der beiden wäre keine *Kalte Galvanik* denkbar. Aber auch die Sekretariatsarbeit für beide habe ich sehr genossen. Angerufen haben fast immer auch jene, denen ich für die Mithilfe bei der Gitterfertigung danken möchte: Heike Fornasier, Christin Straus, Alexandra Karbacher, Julia Wolf, Marie Christin Nees und Alexander Bacher. Bei der Röntgenoptikgruppe des IMT, bei Danays Kunka, Pascal Meyer, Frieder Koch, Martin Börner und Klaus Bade möchte ich mich für die Unterstützung in den unterschiedlichsten Aufgabenstellungen bedanken.

Ein ganz spezieller Dank geht auch an die Arbeitsgruppe von Prof. Frank Pfeiffer an der TUM, mit denen zusammen die Gitter untersucht wurden. Mit Hilfe von Julia Herzen, Marian Willner, Alex Hipp, Lorenz Birnbacher wurde es erst möglich, die unterschiedlichen Gitter zu testen.

Für die wissenschaftliche (und manchmal nichtwissenschaftliche) Begleitung der Arbeit möchte ich mich für die vielen interessanten Diskussionen mit allen Mitarbeitern des IMT bedanken, speziell bei den Zimmernachbarn Thomas Grund, Markus Simon, und Felix Marschall.

Zu guter Letzt möchte ich mich noch von tiefstem Herzen bei meiner Frau Laura und meiner Tochter Hannah bedanken, die in all den Jahren mich tatkräftig unterstützt, aufgebaut und manchmal auch ertragen haben.

Karlsruhe, im September 2017

*Maximilian Amberger*

# Contents

<b>1</b>	<b>Kurzfassung</b>	<b>i</b>
<b>2</b>	<b>Abstract</b>	<b>iii</b>
<b>3</b>	<b>Introduction</b>	<b>1</b>
3.1	Motivation	1
3.2	Outline	3
<b>4</b>	<b>LIGA gratings for x-ray phase contrast imaging</b>	<b>5</b>
4.1	X-ray differential phase contrast imaging	6
4.2	The LIGA process	10
4.3	Material properties of mr-X resist	14
4.4	Microstructure fabrication and defects	18
4.5	Interaction of x-ray lithography and electroplating	26
4.6	Importance of environmental conditions	28
4.7	Visibility simulations to predict grating behavior	29
4.8	Simulations as a tool for layout generation	32
4.9	Solutions against resist deformation	34
<b>5</b>	<b>Mechanical resist behavior in the electroplating solution</b>	<b>37</b>
5.1	Tensile tests on mr-X resist	37
5.2	Mechanical parameters of mr-X resist	39
5.3	Impact of humidity on mechanical stability of mr-X resist	45
5.4	Heated tensile tests on mr-X resist	46
5.5	Thermal expansion of mr-X resist	47

5.6	Differential Scanning Calorimetry . . . . .	50
5.7	Demonstration of a gratings mechanical instability . . . . .	52
5.8	Conclusions drawn from the mechanical characterization . . . . .	54
<b>6</b>	<b>Room Temperature Gold Electroplating . . . . .</b>	<b>57</b>
6.1	Standard LIGA electroplating . . . . .	58
6.2	Impact of lower temperatures on an electroplating bath . . . . .	63
6.3	Low temperature gold sulfite plating bath for flat specimen . . . . .	65
6.4	Low temperature electroplating of UV- and x-ray samples . . . . .	79
<b>7</b>	<b>Low temperature gratings used in phase contrast imaging 91</b>	
7.1	Characterization of gratings at x-ray sources . . . . .	91
7.2	Tools for grating quality evaluations . . . . .	92
7.3	Measurements at the HAR-WI II beamline . . . . .	94
7.4	Visibility measurements at the x-ray tube at TUM . . . . .	97
7.5	Comparison of gratings from low temperature and regular electroplating bath . . . . .	99
7.6	X-ray imaging with low Temp. electroplating gratings . . . . .	102
<b>8</b>	<b>Summary and outlook . . . . .</b>	<b>103</b>
<b>A</b>	<b>Appendix . . . . .</b>	<b>109</b>
A.1	Performance criterion table . . . . .	109
A.2	Duty cycle correction . . . . .	109
A.3	Interferometric investigation of grating period and grating errors . . . . .	111
A.4	Starting growth behavior in nickel electroplating . . . . .	112
A.5	Integrated Anodes for more homogeneous current distribu- tions . . . . .	113

## 3 Introduction

### 3.1 Motivation

"Don't talk to me about X-rays. I am afraid of them" [25]. Whilst this statement by Thomas A. Edison with the wisdom of hindsight was clearly true for his time, it certainly is outdated nowadays. More than 100 years after the discovery of the x-rays [76], even if their field of application has not changed since, security regulations did.<sup>1</sup> And with the deeper knowledge about the risks of x-rays and how to manage them, they could be put to full use in a number of applications, but most prominently in medical imaging [36].

X-ray imaging still accounts for about two thirds of the annual medical imaging examinations, making them the by far most prominent methods used [69]. Imaging methods using x-rays have seen a lot of improvements over the years, steadily increasing the information that can be gathered with these instruments. Most prominent development steps were the use of digital photo plates, enhanced x-ray sources, the use of both for 3D tomography in contrast to single projection imaging and the introduction of contrast agents for functional imaging. Latest developments in x-ray imaging include spiral image acquisition, the use of two photon sources and multi spectrum imaging.

When looking at its closest competitor, Magnetic Resonance Imaging (MRI),

---

<sup>1</sup> Roentgen himself got lucky when dealing with x-rays as he used zinc boxes and lead plates to shield his photographic plate from accidental exposure, which by chance also protected him. Other researchers weren't as lucky and skin burn, hair loss and cancer was found among those working with x-rays. Typically, researchers and engineers showed a happy-go-lucky attitude towards their experiments. So one of the first applications of x-rays was hair removal.

there are two distinct disadvantages in x-ray imaging and tomography. The first is the x-ray dose applied to the patient, which cannot be neglected. The second is MRI's ability to distinguish between soft tissue even without the use of contrast agents. This drawback is being addressed by x-ray phase contrast imaging, the latest development in x-ray imaging, which is already in development to be implemented into medical diagnostics.

This radically different approach to x-ray imaging not only measures the attenuation of the x-rays through a sample but also the phase of the x-rays. Attenuation in classical x-ray imaging allows to distinguish between materials with high x-ray absorption (bones, teeth) and low x-ray absorption (soft tissue). Phase contrast imaging can additionally measure both the phase of the x-rays penetrating the object as well as the dark field. One important aspect of this approach is that in contrast to absorption, phase shift can be quite different also for various soft tissues, making it possible to distinguish soft tissue from each other. And with dark field imaging, which especially accentuates x-ray scattering, a third kind of differentiation in an image is possible. X-ray phase contrast imaging can therefore achieve excellent contrast between various tissues in medical samples combined with the high resolution known from conventional x-ray imaging [4].

For this, principles from conventional optics have been successfully transferred to the x-ray spectrum. The technique is based on phase contrast imaging via diffraction gratings, which was demonstrated in the visible spectrum by Frits Zernike in 1942 [96]. Among others, the today most promising approach for phase retrieval called Grating Based Imaging (GBI) uses gratings designed for the x-ray spectrum and conventional x-ray sources to create a periodic pattern which allows the measurement of phase shift and absorption of the investigated object. One of the main technological challenges for GBI is to produce gratings that are able to absorb a sufficiently large fraction of radiation in their absorbing structures, while being fully transmissive in the spaces in between. While the first gratings used were made with classical silicon micromachining [17][91], subsequent experiments typically relied

on gratings fabricated with the LIGA<sup>1</sup> technique that allowed for unprecedented grating heights and aspect ratios. With rapid development in the fabrication of grating structures by LIGA, aspect ratios (width to height ratio of a single grating line) of 1:100 and heights of 200  $\mu\text{m}$  and more could be achieved [45]. But with growing height more and more structural deviations stemming from the fabrication processes became apparent during the electroplating step. The aim of this work is to provide a profound insight into the interplay of lithography (including development and bake steps) and electroplating to identify the root cause of the structural deviations. Main focus will be put into a deeper understanding of the resist material, the way it reacts to the processes and its state when it enters electroplating. In a second step, to avoid thermal stresses during electroplating which are among the most likely candidates for the deviations, a low temperature gold plating bath for the production of absorption gratings shall be formulated. The resulting gratings will provide the information, whether low temperature gold electroplating can be a viable route to even more precise grating fabrication.

## 3.2 Outline

At the beginning, basic principles of x-ray phase contrast imaging and the LIGA process will be discussed in chapter 4. There, especially the close connection of grating quality and imaging results will be highlighted. After giving a short summary of the previous work on grating quality improvement, the two main foci of this work are introduced, which are a profound understanding of the resist material and the second a deformation free electroplating process.

In chapter 5, the new mr-X resist material will be investigated concerning its basic mechanical properties. A special focus will be on changes in these properties during different mechanical and chemical surroundings, giving new insight into the material during lithography and electroplating steps.

---

<sup>1</sup> Abbreviation: Lithographie (lithography)- Galvanik (electroplating)- Abformung (molding)

Whilst in the previous chapter the root causes for some of the deformations are defined, in chapter 6 one possible countermeasure is introduced, namely the use of a low temperature electroplating bath. The impact factors of a reduced bath temperature will be theoretically investigated. Afterwards, in a three-step approach, a low temperature electroplating bath formulation will be defined, refined and tested. Those tests will also include grating structures.

In chapter 7 those gratings will finally be put to use to demonstrate the new possibilities of this enhanced bath formulation. Emphasis will be on demonstrating the high structural conformity of these low temperature gratings. The last chapter will sum up the results that have been achieved during this thesis and will give a short outlook to some future topics of research that arouse in the course of this work.

## 4 LIGA gratings for x-ray phase contrast imaging

Whilst LIGA processes and final structure quality have been thoroughly investigated over the years, the knowledge about the processes involved have to be refined continuously to fabricate complex and demanding structures. Depending on the final use of a LIGA fabricated product, structural quality can have a range of meanings and implications. For example, in the fabrication of watch parts, sidewall roughness of the final metal parts is considered most critical [26]. For other applications like x-ray lenses, the spatial conformity of the designed layout with the final polymer structures is of critical importance [84]. Most of those structures typically rely on only a few but individual critical process steps which define the respective quality. Process interactions on the other hand are quite difficult to understand and quantify but can play critical roles for the desired fabrication results. So as a reference system for the understanding of the structural quality regarding the interaction of lithographic and electroplating steps, gratings for x-ray phase contrast imaging are chosen for the following reasons:

- Fabrication is on the edge of what is currently possible with LIGA
- specifications from x-ray imaging on gratings imposes the fabrication of highly fragile structures, which are especially prone to deformation through any kind of mechanical stresses
- Gratings for x-ray phase contrast imaging have seen a high demand over the last few years [10] [65], giving statistics about fabrication variance in all fabrication steps

- Deviations over large scales can be visualized by generating large area performance indicators
- Provide an outlook to small scale mass fabrication of LIGA structures and the challenges for this task.

The following chapter will give a short overview of grating use, fabrication, the main structural deviations and their potential root causes.

## 4.1 X-ray differential phase contrast imaging

Grating based X-Ray Differential Phase Contrast Imaging (DPCI) is a rather new technique that enables the acquisition of phase shift [17], dark field signal [71] and attenuation of x-rays passing through irradiated material simultaneously by using the Talbot-Lau effect [86]. This effect describes the appearance of a self-repeating spatial pattern (Talbot effect) in the x-rays intensity after passing a phase-shifting grating (also called phase grating or G1) if the incident beam has enough spatial and temporal coherence. For large sources (i.e. spatially incoherent) a second grating (called G0) can be used to overcome this limitation [72] (Talbot-Lau effect [50]).

A grating for x-ray phase contrast imaging is defined as a periodic geometry (typically a line and space configuration), which contains acting structures and a free (or transparent) space in between. The acting structures can either shift the phase of the incident beam or attenuate the x-ray intensity. The main challenge for grating fabrication is the low absorption of x-rays in most materials, making grating fabrication one of the critical steps in the development of this technique.

When an additional object is inserted behind the phase grating it distorts the phase information defined by the grating and therefore alters the resulting intensity distribution. This new interference pattern now also carries information about the phase and attenuation of the object placed inside. But as typical pixel sizes of x-ray detectors are in the range of a few  $\mu\text{m}$  up to

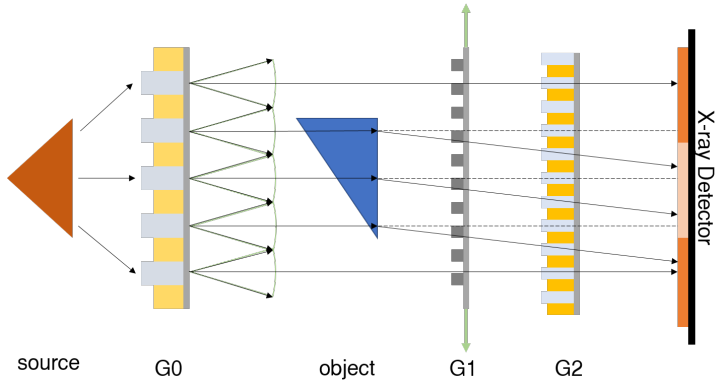


Figure 4.1: Schematics of a DPCI setup with an incoherent x-ray source. The phase grating for this kind of setup could be placed on either side of the object.

1 mm, they are too large to resolve this new interference pattern directly. Instead, the alteration can be detected by placing another absorption grating (called G2) at exactly the Talbot distance, the plane where the self-image of the phase grating appears. By stepping the grating within this plane in steps smaller than the grating pitch, one can resolve the "black and white" pattern of the phase grating's self-repetition as well as any distortions stemming from objects in the beam. The intensity measured during the stepping in each of the pixels resembles a sine wave with a constant positive offset and a random (for an empty setup) but repeatable phase angle. When an object is inserted into the beam, an object dependent shift in phase is added so that the altered beam has a slightly different phase than the previously recorded reference. The intensity for one pixel during these steps is displayed in figure 4.2. The blue line resembles a reference measurement with a sinusoidal fit of the original, noisy data. The green graph, which represents a measurement with an object included, has a shift in phase, an overall loss of intensity (equals increased absorption) and a decrease of the sinus' amplitude, which corresponds to a loss of visibility ( $V$ ). This system param-

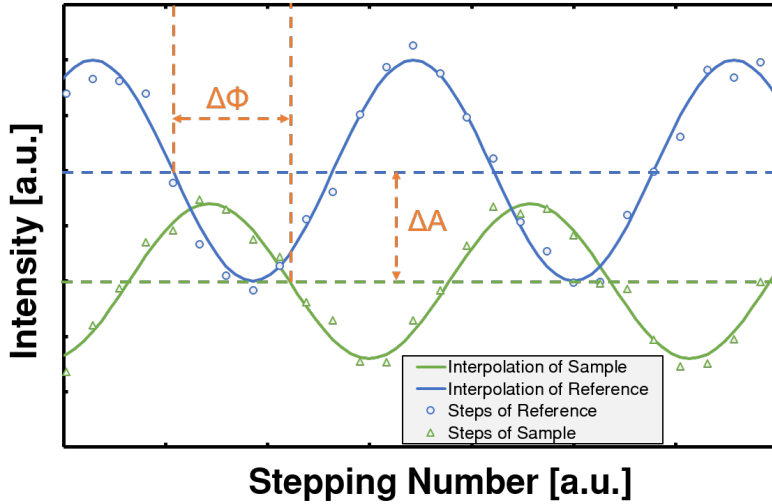


Figure 4.2: Intensity values measured along several acquisition steps, giving the characteristic sinusoidal intensity variations. Phase difference  $\Delta\Phi$  and absorption difference  $\Delta A$  are highlighted.

eter called visibility is used to characterize the ability of a setup to measure the encoded phase signal. The visibility is calculated as the difference of the minimum and maximum intensity levels for each pixel during the scanning steps, normalized by the sum of both signals: [1]

$$Vis = \frac{I_{max} - I_{min}}{I_{max} + I_{min}} \quad (4.1)$$

The differential phase  $\Delta\Phi$  is measured by subtracting the phase angles of reference ( $\Phi_0$ )- and sample ( $\Phi_1$ ):

$$\Delta\Phi := \Phi_0 - \Phi_1 \quad (4.2)$$

The differential phase of an x-ray beam can give high contrast for materials where absorption based imaging can't, as materials with similar attenuation

might hold distinctive phase shifts [64]. Also, materials with small absorption coefficients in the x-ray spectrum (e.g. soft tissue) can yield sufficient phase shift, which allows for a significantly enhanced degree of differentiation in comparison to regular x-ray imaging. But in addition to the detection of phase differences, it is also possible to calculate the absorption ( $A$ ) within such a sample by using the mean value of all steps for each single pixel.

$$A = -\ln \frac{m_0}{m_1} \quad (4.3)$$

In equation 4.3,  $m_0$  and  $m_1$  represent the mean intensity values of a single pixel for all steps with and without an object. A third kind of contrast, which can be obtained with such a setup is the dark field signal. It is defined as the ratio of a setups visibility value with and without an object [57]. Just like dark field imaging in conventional microscopy, it is highly sensitive to scattering within the sample, especially highlighting interface regions [71].

$$D = -\ln \frac{Vis_{object}}{Vis_{reference}} \quad (4.4)$$

For grating evaluation, another factor is of importance, which is the number of photons. When the dose for a sample object is fixed, the number of photons reaching the detector is mostly influenced by two factors: absorption in the gratings lamellas due to microscopic distortions and absorption in the grating substrates. Absorption in the gratings after the examined object is problematic, as for equal intensity at the detector the flux has to be increased, which also means higher dose applied to the sample. To factor in the flux ( $f$ ) for characterization, one can use the signal-to-noise ratio (SNR) [32]. The SNR gives a more complete picture of the imaging quality of a grating instead of visibility, as it also takes photon flux into account.

$$SNR \propto Vis * \sqrt{f} \quad (4.5)$$

The use of x-rays on the one hand combined with finely structured absorbing gratings on the other hand creates unique specifications on the gratings. And the gratings for such an imaging setup have to be fabricated as precise as possible. Even the slightest deviation of the gratings' duty cycle, period or also an undulation of the grating lines will produce artifacts in the signal. Additionally, due to the energy of the x-ray photons, strongly absorbing materials have to be used in gratings with high aspect ratios (ratio of a gratings line width to grating height) to achieve sufficient attenuation. The grating period is defined by the desired setup geometry and setup sensitivity [88]. To be implemented into current medical x-ray imaging system geometries, grating periods of  $5\ \mu\text{m}$  or less are required. Considering the photon energies of x-ray applications ranging from  $10\ \text{keV}$  in some medical imaging setups to  $200\ \text{keV}$  for material science applications, gold absorber heights of up to  $20\ \mu\text{m}$  to  $500\ \mu\text{m}$  thickness are potentially needed to achieve adequate attenuation [42].

Fabrication errors will result in a loss of visibility due to geometric deviations. Typically, distortions also reduce flux, but in some cases will increase visibility (e.g. smaller grating periods without deformation or smaller G2 absorption). It is also possible to increase flux, for example by reducing the metal height in G2 gratings, but this will reduce visibility. This again highlights the usefulness of an SNR comparison, as geometric deviations can increase visibility or flux, but not both. In this case, their trend points in opposite directions and SNR is ultimately lower. As a summary: For grating fabrication, it is of utmost importance to maximize visibility and minimize absorption in the setup.

## 4.2 The LIGA process

All the boundary conditions noted in the previous chapter for phase contrast setups limit the number of manufacturing methods for x-ray gratings. There are two main fabrication schemes for x-ray gratings [58]. In addition to

conventional silicon etching [16] a second method for grating fabrication is the Direct-LIGA technique, where only x-ray lithography and electroplating are used for the production of gratings [5]. Four typical process steps of the LIGA technique are pictured in figure 4.3.

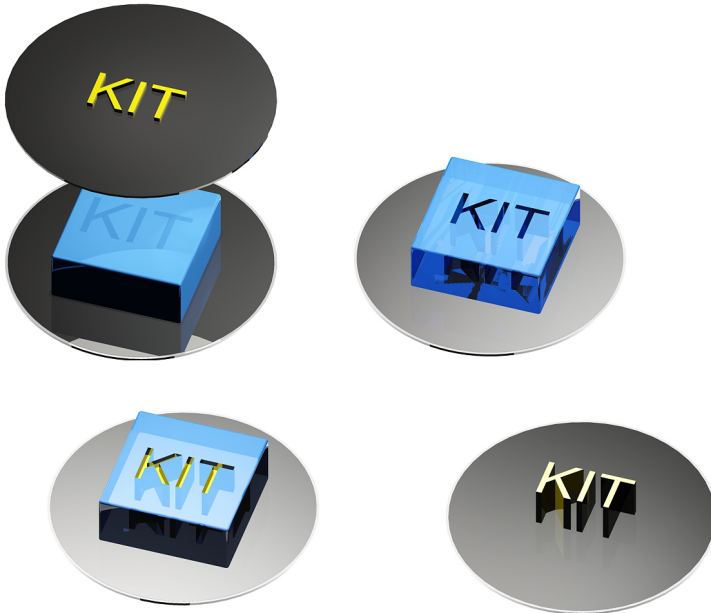


Figure 4.3: Schematics of the Direct-LIGA process: Step 1: Exposure of a resist layer through x-ray lithography Step 2: Chemical development of the resist to remove uncrosslinked material Step 3: Electroplating of a metal into the insulating polymer mold Step 4: Removal of the surrounding resist to obtain the metal microstructure

In the LIGA process applied for grating fabrication, a substrate is coated with a thick layer (up to  $100\ \mu\text{m}$  or more) of a negative tone resist that can be patterned by x-rays. During the exposure, the x-rays (typically with a photon energy in the range of  $1\ \text{keV}$  to  $10\ \text{keV}$ ) have to pass a working mask that contains highly absorbing gold structures. This mask is fabricated by e-beam or direct laser write lithography. A master mask is copied via lithog-

raphy into a working mask with higher gold thickness. For the typical resists (including SU-8 and mr-X, see section 4.3) a post exposure bake (PEB) is done to activate and complete crosslinkage after lithography. As only negative tone resists are used for grating fabrication, exposed areas can be developed afterwards by dissolving uncrosslinked parts of the polymer. The gratings itself are typically made of resist lines with high aspect ratios (AR). Depending on the aspect ratio and the processing, there have to be a number of transversal structures to support the grating lines.

With a conductive substrate, the polymer mold can then be filled by electrodeposition with a range of metals. In grating fabrication, these metals are gold for absorption gratings and nickel for phase shift gratings. As additional phase shift is not desired, the resist mold is removed for the phase gratings, as their metal structures have lower aspect ratios and therefor are mechanically stable without the polymer in between. In the G0 and G2 gratings, mold is typically not removed as it stabilizes the metal microstructures and is almost transparent for x-ray photons. Samples fabrication in this work represents state of the art LIGA processing in 2013 and has been described in detail by Kenntner [45], Meiser [58] and Koch [47]. Therefore, only a short summary is given in the upcoming sections.

### **4.2.1 Sample processing prior to and after exposure**

Starting base are  $\text{TiO}_{2-x}$  coated wafers which are one of the standard substrates for high aspect ratio LIGA structures. They are prepared by sputter depositing  $2.5\ \mu\text{m}$  of Ti onto  $525\ \mu\text{m}$  thick silicon wafers. To create a nanostructured surface which promotes adhesion, the coated wafers are oxidized in a sodium hydroxide / hydrogen peroxide mixture for 2.5 min [63]. Those surfaces yield both high adhesion of the resist on the substrate as well as a sufficiently conducting surface. As metallic Ti is present at or right below the surface, there are enough nucleation spots to start the electroplating. Thinner silicon substrates (e.g. to reduce absorption when used in

x-ray phase contrast imaging) are fabricated by mechanical backgrinding to a thickness of 200  $\mu\text{m}$ .

Resist is then applied by spin coating with a resist thickness conformity of 5 % or better. Subsequently a heating step (called *soft bake*) follows to decrease the resists solvent concentration to less than 3 % to 5 % of weight, which is controlled by measuring the wafer mass before and after the process step. Drying through heating is done in a vacuum oven at 95 °C. Already after softbake, the resist layers contain significant intrinsic stresses which are relieved at elevated temperatures [47] or by prolonged room temperature relaxation, as was shown by Lemke [51]. Therefore, the wafers should not be used right after spin coating and drying but usually after at least one day of relaxation. Prolonged storage does not harm the exposure afterwards, but the viscoelasticity of the samples can lead to a reflow of the resist when not stored properly (e.g. in an upright position the resist flows downward, creating a slope in resist height).

After exposure (see chapters 4.4.1 and 4.2.2), the samples are put into the oven again for a second baking step (*Post Exposure Bake* or *PEB*), this time to initiate and catalyze the crosslinkage reaction. Typical parameters used in this work are 75 °C for 140 min [58] followed by a very slow cooling ramp down to room temperature.

### **4.2.2 X-ray lithography of mr-X resist**

X-ray lithography is performed at both the *Litho 1* and *Litho 2* beamlines at the ANKA (*Angströmquelle Karlsruhe*) facility of the KIT. Most characteristic for the *Litho 1* beamline is its relatively low energy of 2 keV [58], which results in a strong difference in the dose applied to the resist at its top and at the bottom close to the substrate. Due to the high absorption in the resist, a dose difference (also called top-to-bottom-ratio) of 3 or more is typical. Regarding the mechanical state of the resist, a lower top-to-bottom ratio would be preferred. For the production of gratings with small periods,

only low energy x-ray sources are feasible, as high energy x-rays lead to stronger crosslinkage in the unexposed areas. This limits the usability of high energy beamlines like *Litho 2* at ANKA for the production of gratings to periods in the range of 5  $\mu\text{m}$  or larger. Typical grating structures are fabricated at the *Litho 1* beamline with a bottom dose of  $120 \frac{\text{J}}{\text{cm}^2}$  to  $140 \frac{\text{J}}{\text{cm}^2}$  and a top-to-bottom-ratio of 3.

One important factor that links fabrication issues in x-ray lithography with electroplating is the unwanted application of additional dose to the top surface of the resist layer through photo electrons of the masks metalization layer ( $\text{Ti}/\text{TiO}_{2-x}$ ). This effect can be reduced with thin Kapton foil filters to absorb parts of the misplaced dose. But these filters also create undesired side effects like particles or resist sticking to Kapton foil. So, depending on the exposure conditions, small skins of crosslinked material on top of the structured area can be found. This "skin-effect" effectively hinders the metal growth by building a barrier to the electroplating liquid. If it is thin enough, this skin layer can be removed with an additional directional etching step (D-RIE), which also removes residue on the bottom of the cavities stemming also from secondary effects (photo electrons and fluorescence) in the  $\text{TiO}_2 - x$  layer of the substrate.

### 4.3 Material properties of mr-X resist

For the fabrication of all microstructures, a new SU-8 based negative resist called mr-X (from micro resist technology, mrt, Berlin) is used [27]. In previous work at the IMT it was shown by Kenntner et. al [45] that mr-X has favorable mechanical stability concerning the fabrication of grating structures with very high aspect ratios of 100 or more via the LIGA technique.

As the resist material plays a crucial role in understanding deformation mechanics, the basic crosslinking mechanism and the reaction dependent mechanical parameters of this new resist will be introduced. Afterwards a com-

parison of SU-8 and mr-X concerning their mechanical properties will be made.

### 4.3.1 Crosslinkage reaction during X-ray and UV exposure

Being a SU-8 based negative tone resist, mr-X mainly consists of epoxy resin mixed with a suitable solvent (for mr-X:  $\gamma$ -Butyrolactone -GBL), which is also the most commonly used solvent for SU-8. Both resists contain small quantities of a photoactive agent, also called PAG (photo acid generator), that releases Lewis-acids upon the absorption of energy (not necessarily a photon) [12]. In the case of mr-X, the aromatic groups in Triarylsulfonium hexafluoroantimonate are supposed to absorb photons and then release  $\text{HSbF}_6$ , an acid that can easily induce a ring-opening polymerization of the epoxy groups. As it is not consumed during the polymerization (unlike the Triarylsulfonium group), it acts as a catalyst for the polymerization. The reaction has to be further assisted by thermal treatment of the exposed material. In contrast to UV lithography, X-ray exposure can release the photoacid in several different ways, including acid generation by fluorescence of the surrounding material or the breakup of the PAG caused by low energy secondary electrons. These release mechanisms are both only partly localized (e.g. the fluorescence is absorbed in the resist within a certain distance), which is the main reason for LIGA's rather coarse resolution compared to UV lithography.

During the post-exposure-bake step, cationic polymerization is initiated. This crosslinkage is controlled by both the diffusion length of the generated protons as well as the rearrangement speed of the monomers. Crosslinkage therefore only happens if both a proton and two matching monomers are present. Whilst this probability during the starting phase of the PEB process is high at some point of time the increasing mechanical stabilization due to the growing network hinders the polymer chains in their movements

and finally inhibits any further reaction [44]. This so-called *cage effect* will prevent a 100 % conversion of all reaction sites for crosslinkage even after extremely long times of baking. Also, depending on the PEB duration, significant amounts of monomers are trapped within the polymers network. Due to the increasing degree of crosslinkage the glass transition temperature ( $T_G$ ) rises [24]. As the  $T_G$  of the uncured resist before PEB is around 50 °C, significant polymerization cannot start below that temperature, even if the protons' diffusion length is quite large in the time between exposure and PEB. Below the glass transition temperature, most of the monomers are frozen in place, which reduces the probability for the nucleophilic attack to almost zero.

Uncrosslinked resist in not illuminated areas can afterwards be removed by various solving agents like PGMEA (Propylenglycolmonomethylether) or GBL ( $\gamma$ -Butyrolacton).

### **4.3.2 Mechanical properties of crosslinked SU-8 and mr-X**

As the resist material is still under development, only a few preliminary results have yet been published. Most of them [51] indicate that mr-X matches the desired mechanical characteristics of SU-8 very closely for the applied process parameters.

One important aspect for mechanically unstable results when using mr-X resist is its viscoelastic nature. This viscoelastic behavior leads to a mechanical reflow, if the material undergoes long-time stresses like after soft-bake or PEB. As was shown previously by Lemke [51], during a time span of 8 h the bending of a wafer caused by solvent evaporation can be reduced significantly. This effect is attributed to stress relaxation in the resist material due to a viscoelastic reflow processes.

As there is no other data reported, it is assumed that mr-X has similar mechanical properties to SU-8. A thorough and detailed analysis of SU-8 has been done by Feng [24], who performed among others measurements of

stress vs. strain, glass transition temperatures and dimensional changes during processing, the effect of humidity on residual stresses and DSC (*Differential scanning calorimetry*) measurements. All those experiments are done for different processing conditions, most notably variations in PEB time and temperature. Some of the reported values can be found in table 4.1.

Properties of SU-8	Value	$T_{PEB}$	Reference
Young's Modulus	$2.5 \pm 0.5$ GPa	95 °C	Feng 2003[24]
	4.02 GPa	95 °C	Lorenz 1997 [53]
Tensile Strength	60 MPa	standard	Data Sheet [60]
	105 MPa	not published	Feng 2002 [23]
Elongation at Break	6.5 %	standard	Data Sheet
	11 %	not published	Feng 2002 [23]
Residual Film Stress	16 MPa to 19 MPa	95 °C	Lorenz 1998 [54]
	11 MPa to 16 MPa	70 °C	Schütz 2004 [83]
	10 MPa to 25 MPa	40 °C to 100 °C	Keller 2008[44]
Glass Transition Temperature	50 °C	after Softbake	LaBianca [49]
	>200 °C	after Hardbake	LaBianca [49]
Coefficient of thermal expansion	52 ppm/K	95 °C	Lorenz 1998 [54]
	200 ppm/K	200 °C	Feng 2002 [23]
Volume shrinkage	7.5 %	not published	Guerin [31]
Young's Modulus	2.5 GPa	65 °C	Lemke 2010 [51]
	3.4 GPa	not published	Grimm 2010 [51]
Residual Film Stress	<1 MPa	unexposed resist	Lemke 2010 [51]
	$6 \pm 3$ MPa	70 °C	Lemke 2010 [51]

Table 4.1: Summary of the mechanical properties of SU-8 and mr-X

Wouters [94] has already shown that the uptake of water into SU-8 is minimal and only leads to minor swelling of the crosslinked polymer. No data is available for mr-X, but it is assumed that it behaves accordingly. Nevertheless, even very small water content can lead to noticeable changes in the mechanical behavior of SU-8, as was shown by Schmid [80]. He states

that whilst Young's Modulus is hardly affected by moisture, residual stresses are significantly lower in high humidity atmosphere, which equals more water/moisture in the structures. Also, elevated temperatures increase the influence of water on the mechanical stability of SU-8. The mechanical investigations in chapter 5.2 will highlight whether any of these factors mentioned might play a critical role for the processing of x-ray gratings.

### **4.3.3 mr-X resist inhomogeneities**

Like all SU-8 based resists, the mr-X resist shares one common problem, which is the epoxide content of the resist. These epoxides cannot be bought in perfectly reproducible quality, which essentially shows in batch to batch fluctuations of their molecular weight distribution [67]. Especially the high molecular weight components differ from sample to sample. Those differences in composition can finally lead to changes in the materials properties due to their different reactions during crosslinkage, which will become apparent for structures that are mechanically fragile. Therefore, most experiments have always to be done with the knowledge in mind that process variations are related to properties that can ultimately not be accounted for. Close process observation and detailed sample analysis help to differentiate those variations from process induced sample variations. Also, having statistically relevant sample sizes helps to differentiate effects from batch variations. For this, the strong demand for gratings in x-ray imaging setups has been helpful to gain statistically relevant data regarding those fluctuations.

## **4.4 Microstructure fabrication and defects**

### **4.4.1 UV lithography**

As structures are needed to investigate the performance of gold electrolyte formulations, UV-lithography as a faster alternative to x-ray LIGA is em-

ployed. With mr-X it is possible to fabricate microstructures with moderate aspect ratios (AR up to 10 [51]). To determine the dose necessary to obtain well defined structures, a set of samples are illuminated with different dose values. The mask contains finger like structures (see fig. 4.4) going from the 100  $\mu\text{m}$  range down to feature sizes below 1  $\mu\text{m}$  in both negative and positive tone. For the lithography of micron sized structures, a 365 nm filter ("I-Line") is used. Large scale (>1 mm) sample structuring is done without any filters with the full spectrum beam using film masks printed on regular inkjet printers.

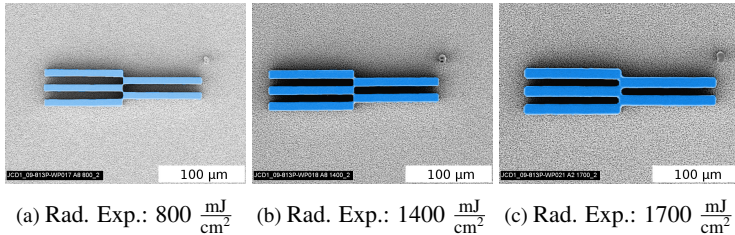


Figure 4.4: Structures with radiance exposures of 800, 1400, 1700  $\frac{\text{mJ}}{\text{cm}^2}$  from left to right, showing an increasing crosslinkage in shadowed areas and rounding of the edges

As a result, it is found that the radiant exposure<sup>1</sup> of 1.4 J/cm<sup>2</sup> leads to stable structures without creating resist skins on the bottom due to backscattering or rounded edges (see fig 4.4). The most suitable exposure level is also tested for the creation of the microstructure test pattern explained in chapter 6.4.1. In order to fabricate those structures, a line and space mask of 50  $\mu\text{m}$  wide gold lines and 30  $\mu\text{m}$  spacing was used. To create hollow structures, two exposures are done where the second exposure is performed orthogonally to the first one to create the square pattern. As the resist is double exposed, the radiance exposure is lowered to 1.1 J/cm<sup>2</sup> per single lithography step to avoid crosslinkage in the pillar-shaped voids.

<sup>1</sup> In contrast to X-ray lithography, only the total energy flux and no dose can be given for this particular setup, as the reflection and absorption coefficient of the  $\text{TiO}_{2-x}$  substrate is not known and therefore no dose in resist can be calculated.

### 4.4.2 Grating fabrication and layouts

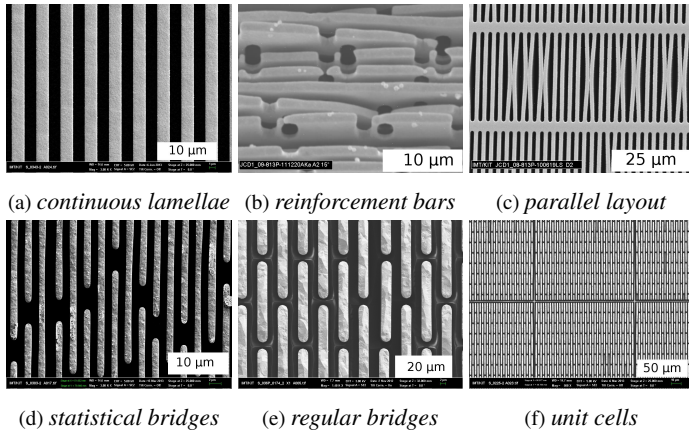


Figure 4.5: Different layouts used for grating fabrication. All pictures show electroplated gold gratings (bright regions) except for the parallel layout in fig. 4.5c, where only the resist structures appear bright. The sunray grating in fig. 4.5b is viewed from a tilted position to highlight the holes that before resist stripping have been holding the reinforcement bars.

Over the years a range of grating layouts has been established at the IMT. Figure 4.5 gives a graphical overview of the typical layouts used. For most of them the goal is to steadily increase structural stability while sticking as close as possible to a perfect line and space grating pattern. These grating designs all show different characteristics in those fields: mechanical stability, crosslinkage in shadowed area, duty cycle compliance, electroplating start and tendency for overgrowth. Each of these affects grating quality before and after electroplating.

Whilst continuous lines (fig. 4.5a) are the ideal form according to their imaging performance, their mechanical stability is rather poor [45]. CTE mismatch, resist shrinkage and also capillary forces all contribute to deformation of the lamellae (in grating fabrication, the metal grating lines are also referred to as lamellae). One way to stabilize the structures is via rein-

forcement bars that penetrate the lamellae in an  $45^\circ$  angle (fig. 4.5b) [30]. This approach leads to homogeneous structures, but the fabrication process is quite time-consuming as it involves three lithography steps including at least one change of the mask after the first step. To fabricate gratings in a single exposure step but with increased mechanical stability, resist bridges between the lamellae are used as bracing, although they decrease the visibility of such a grating significantly<sup>2</sup>. Those interconnections between the resist lamellae help to stabilize the structures but also introduce significant lateral forces that can distribute over the entire wafer. Therefore, bridge designs show significant distortions when going to larger continuous grating areas.

One way to overcome this problem is to use a *parallel layout* (fig. 4.5c). In those tensions in the resist lamellas are decreased, as no connections are made at the middle of the lamella, its weakest spot. However, the lamellae are now free standing over their entire length, which decreases their mechanical resistance to bending via capillary forces during development. Intersecting layouts with *statistically distributed* (fig. 4.5d) or *regular* (fig. 4.5e) reinforcement bridges reduce the transversal forces, but can create stress gradients in the grating. Another way to overcome large area distortions are bridged layouts with separation lines between the single cells (fig. 4.5f). The dimensions of a cell of connected grating lines usually is  $100\ \mu\text{m} \times 10000\ \mu\text{m}$ .

### 4.4.3 Grating Defects

Like all manufacturing methods, the LIGA technique has some characteristic flaws regarding the fabrication of grating structures. A detailed analysis of grating errors including their impact on imaging has been done by Kenntner [45]. Whilst he mainly focused on errors stemming from x-ray lithogra-

---

<sup>2</sup> a quick estimate of relative visibility loss would be the ratio of resist bridge to metal lamella, which is typically 10 %

phy and its pre- or postprocessing steps (e.g. soft- and post-exposure-bake), little mention was made of errors resulting from electroplating or the interplay of electroplating and the preceding processes. A short summary of the described grating errors will be given.

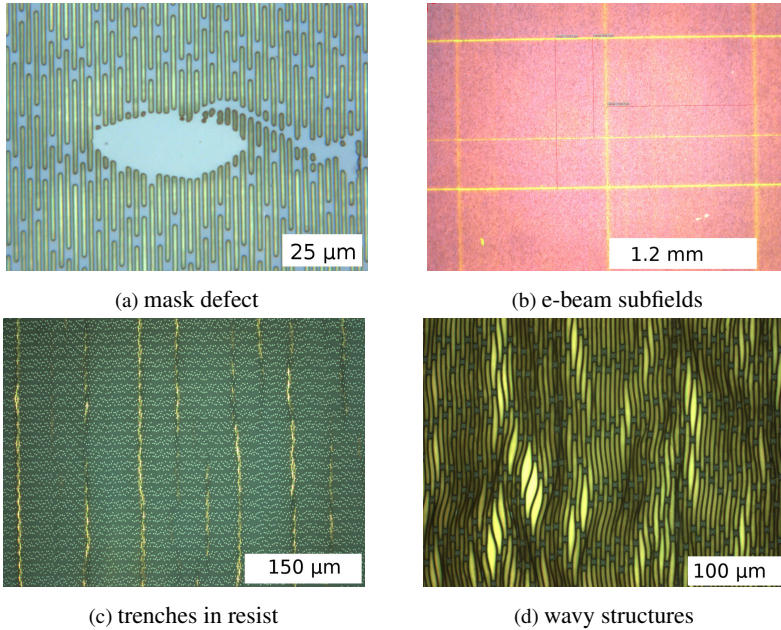


Figure 4.6: Microscope images of 4 typical types of errors found in grating fabrication. All structures are examined after electroplating, thus giving yellow patches for gold and blue/red/gray colors for the resist

One possible way to classify grating errors is to categorize them according to their impact on the final phase contrast image. The first class of errors includes all kinds of effect which produce localized small error regions. Those defects can be the result of particles or mask errors, where small pieces cover the mask or the substrate (see fig. 4.6a). Typical size is up to  $100\ \mu\text{m}^2$ , which can make these defects indistinguishable in an x-ray setup from the background noise. This effect is also depending on the size

of the particle in relation to the pixel size of the detector. Errors like these are usually of minor concern, as they can be controlled through the process by taking special care, if defect-free gratings are required. When apparent they result in a slight local drop in visibility.

The second error class proves to be more troublesome as it contains all large-scale errors. Those can also be created by local inhomogeneities or weaknesses in the resist, but are able to cover the entire grating area. LIGA grating aberrations are mainly caused by two principle effects, but can show up in various forms depending on the processing parameters. The first one is already incorporated into the mask and caused by local misalignments of the electron-beam writer when creating a mask. To structure large areas, the machine stitches its  $1\text{ mm} \times 1\text{ mm}$  sized writing field, but with a slight misalignment from fields to field. This creates a square pattern of locally weakened grating structures, which then get bent during the process steps. They act like predetermined breaking points, usually only getting bent but not broken.

The second source of large-area distortions are intrinsic stresses. Those forces can result in structures that are entirely bent (fig. 4.6d) or show trenches (fig. 4.6c). The probability, whether trenches or full bending appears depends on the resist's and the layout's ability to withstand deformation. If the resist is strong enough to overcome bending, it can still show trenches. To fabricate highly regular grating patterns, it is one of the main work topics of this thesis to understand the origin of these stresses and if possible overcome them or at least reduce their impact.

#### **4.4.4 Mechanical simulations for layout stability prediction**

To investigate the stability and performance of a new grating layout the typical work flow is to create a mask with the desired structures and test it by fabricating a set of gratings in all requested resist heights. As mask

fabrication is expensive and time-consuming, an alternative approach is investigated that allows for faster testing of a larger set of grating variations without the necessity to fabricate a new test mask for each iteration. The use of simulations is a widely adapted tool and in this case, is sought to supplement or even replace parts of the development process.

For this means, 3D models are created in AutoCAD and imported to Ansys as igs files. Meshing is done using the *MultiZone* method producing mostly cubic blocks. And especially the meshing of the gratings proves to be among the most critical points within the process. Precise control over the meshing

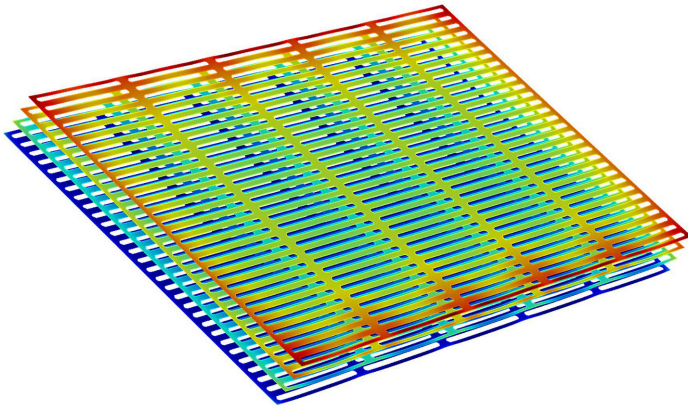


Figure 4.7: Four 2D slices extracted from a deformed grating for further processing in a separate matlab script. Colors indicate the degree of lateral deviation (blue=no/little deviation, red=strong deviation)

process is needed, as the structures are extremely critical for meshing failure. Also, wrong meshing parameters drastically increase computing time. Another reason for fast and reliable meshing is the need for the simulation of large-scale grating structures, as symmetries are limited to a maximum of two planes. To mimic the usual grating defects (see section 4.4.3), an inhomogeneity is incorporated into the resist mold, so the simulated grating has to be defined at least with the dimensions of a unit cell. This inhomogeneity

is a zone of weaker material, where the Young's Modulus is decreased by 10 % to 20 %. For a typical defect grating area, the distance between the trenches is 100  $\mu\text{m}$  to 500  $\mu\text{m}$ , or 40 to 200 periods. This spacing also defines the gratings cell size in the simulations. Along the grating lines the dimensions of the simulated cell were 5 to 10 times the length of a lamella. A set of initial simulations has shown that even for 200  $\mu\text{m}$  wafers instead of the usual 550  $\mu\text{m}$  no significant differences in grating distortions are to be expected. Therefor as a boundary condition the bottom of the grating wafer is implemented as fixed, (i.e. no wafer bow is assumed).

For a mechanical simulation of grating structures, two factors are considered important when looking at deformations: The first factor is the geometric deformation of the resist material stemming from resist shrinkage and the second one is temperature differences in processing which lead to thermal expansion. Those two effects basically point into opposing directions, as a temperature increase implies an expansion of the material, whereas shrinkage reduces the size of the resist structures after the postbake process. In mr-X resist material, shrinkage (2 % to 5 % volumetric shrink) by far outweighs thermal expansion (0.35 % to 1 % for 50 K of temperature difference). But one has to keep in mind that both shrinkage and thermal expansion are interconnected.

It is assumed that both shrinkage and expansion can be added up into one effect to simplify the simulation. Thermal expansion is modeled using a temperature dependent CTE parameter, where the shrinkage is already factored into the coefficient [8]. This coefficient is valid for all temperatures except for the reference temperature, as the simulation, based on the thermal expansion equation:

$$\frac{\Delta L}{L} = \alpha_t * \Delta T \quad (4.6)$$

always gives zero expansion for  $\Delta T = 0$ . The value used for thermal expansion is the measured value of 4 ppm/K. Linear shrinkage is assumed to be 2 %, which equals 6 % of volumetric shrink. For the further processing,

only the deviations in a plane perpendicular to the beam axis are calculated and plotted.

For visibility predictions (see section 4.7), a number of deformed 2D slices through the grating structures parallel to the substrate are extracted and further processed using a matlab script.

To obtain results that are as closely as possible related to the gratings structures, mechanical parameters like Young's modulus that are generated by measurements are fed into the simulations parameter set. This need for precise mechanical parameters is also one of the driving elements of the mechanical investigations on mr-X resist. The Young' Modulus that has been used for all simulations in this thesis is 3.0 GPa.

## **4.5 Interaction of x-ray lithography and electroplating**

Unlike other LIGA samples, grating structures that via microscopic examination seem intact after x-ray lithography, PEB and development show serious bending or waviness when electroplated. Those errors can at first not be addressed to one of the well-known electroplating defects (for those see chapter 6.1.2). Precisely because electroplating on its own has only a limited amount of specific and characteristic errors that can appear during grating fabrication, the origin has to be found in another aspect that so far was not considered in detail for the microfabrication process: It is the impact of the electroplating bath's chemical and physical environment on the crosslinked polymer material.

In general, there are considerations regarding the chemical stability of resist to certain pH values found in electroplating baths [79] or swelling of resist due to the uptake of the electroplating bath's solvent [94]. Most general examinations of the resist-electroplating interplay are centered on the pH dependent adhesion to the substrate [61]. But overall not much effort was put into the interplay of electroplating and lithography for SU-8 type resists

as it is known that SU-8 is chemically stable, shows little swelling [93] and a good compatibility with the pH values of the electroplating baths used in the LIGA process. Own hands-on-experience on the other hand is that SU-8 based grating structures are highly sensitive to the electroplating process, bending or ripping up during electroplating. So, for the fabrication of x-ray gratings the processes have to be tailored to having a minimal impact on structural integrity. To reach this, one has to understand how lithography and electroplating interact with each other.

One of the challenging aspects in the fabrication of defect free LIGA samples is that deformations can be caused and/or exposed by almost all of the process steps. Main source are mechanical stresses which are generated by resist shrinkage, thermal expansion, swelling [29], capillary forces or a CTE mismatch of resist and substrate. As thermal differences can be found in almost all fabrication steps, a thorough study on the influence of temperature and temperature differences during electroplating will be found in chapter 4.4.4. Capillary forces appear both during evaporation after development as well as during all immersion steps in electroplating. Whilst the final polymer structures are quite resistant to capillary forces in aqueous fluids, during development and sample cleaning liquids with higher surface tensions than aqueous solutions are used [45]. Those create stronger capillary forces which finally can lead to the structural breakdown of unsupported or weakened lamellas. One way to overcome this is freeze drying [46]. Another possible source for deformation is resist shrinkage during the crosslinkage reaction of the resist polymer. Typically, one would assume that resist shrinkage should not be a main source of deformation during the electroplating process, as crosslinkage is supposed to be completed after the hardbake. But in a later section (5.5) it is shown that the crosslinkage reaction can still go on during electroplating, possibly causing further shrinkage in the heated bath surrounding.

## 4.6 Importance of environmental conditions

Although gratings are highly susceptible to mechanical and physico-chemical influences, they are not the best tool to analyze the importance of these factors for defect free structures. This is due to the fact that visible errors can be attributed to several different root causes, which makes it impossible to tell which of these is the source of the aberrations. Later on, a number of experiments will be described where these processes are tested individually. As an example, non-electroplated samples with rather fragile structures (*statistical layout*, see section 4.4.2) are exposed to either heat, water or a combination of both. It can be seen in fig. 4.8e that the sample that has been immersed and subjected to heat for a short time does show significant deformation. A second grating that has been immersed in electrolyte at room temperature for prolonged time in contrast has no visible geometric distortions. Whilst the diffusion of water into the resist matrix even over an extended timespan of three days does not lead to any significant deformation, just five minutes at elevated temperatures (figure 4.8e) are enough to introduce waviness and buckling in the resist. The immersion temperature of 55 °C is equal to the operation temperature of the standard gold plating bath used for LIGA structures. So, it is likely that the outcome of this experiment in the electroplating bath would have been the same. This demonstrates that decreasing bath temperature is one of the key factors to enhance structural stability.

As the sample that has been immersed in water (fig. 4.8c) has been taken out of the bath repeatedly for the measurements, the grating structures also have been subjected to a series of evaporation and immersion steps. Each time capillary forces for adjacent lamellae are created and enhanced through differing liquid filling levels. So at least for this set of bridge layout gratings, capillary forces can also be ruled out as a dominant factor in grating deformation. But one has to keep in mind that alternative grating layouts can still be highly susceptible to capillary deformation during the electroplating process, especially those with long, unsupported lamellae.

As a summary from these first tests it is expected that capillary forces during the electroplating process are of a minor concern as gratings are typically already reinforced to withstand those forces acting perpendicular on the lamellas. Main focus should be put onto thermal processing of the samples and the impact of temperature on mr-X resist. These two issues will be addressed in the following chapters, starting with a mechanical characterization of the resist and subsequently the setup of a low temperature electroplating bath.

## 4.7 Visibility simulations to predict grating behavior

To demonstrate the impact of those deviations on x-ray imaging, a tool is created to help identify how the interplay of nonconforming gratings and detector pixel size can influence the visibility. A detectors pixel size is mimicked by taking the mean of the intensity over a certain area. Typically, in the simulation images a factor called *Binning*<sup>3</sup> is given, which is the ratio of the detector pixel size and the grating period. For this intensity data, two grating pictures are superimposed to each other. Typically, there are 10 to 30 different superpositions, each with a slowly increasing offset perpendicular to the grating lamella. The stepping's sinusoidal brightness data in each pixel is then used to calculate visibility according to equation 4.1. While one of the superimposed gratings is a 2D representation of the absorption grating (e.g. a gray scale image), the second one represents the x-ray intensity distribution at the (fractional) Talbot distance. For the superposition, in spaces where white spaces from grating one (i.e. high x-ray intensity) meets a white space of grating 2 (i.e. transmitting part of the grating), full intensity is recorded. For all other combinations, no intensity is the signals outcome.

---

<sup>3</sup> *binning* in this thesis always refers to the binning of calculated matrices. One bin forms one detector pixel by calculating the mean value of a selected area of the intensity matrix. It does not relate to the binning of detector pixels, which is commonly used at setups to increase sensitivity at the expense of spatial resolution.

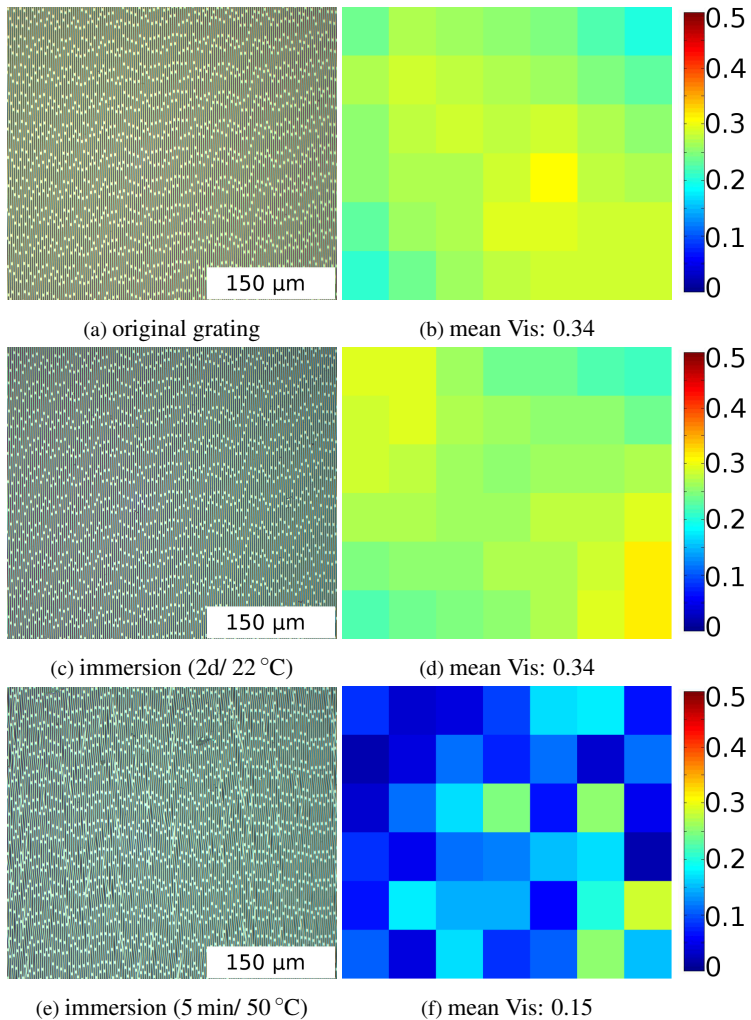


Figure 4.8: Three microscope pictures of resist grating structures with varying immersion times and temperatures (left column). Right column shows their respective visibility simulations. The period to pixel ratio of these simulations is 30:1, so one pixel has a size of 80 μm. As expected, the distorted grating (bottom left) from fig. 4.8e shows a massive drop in visibility compared to the other two gratings.

This simulation setup allows for the demonstration of grating distortions (grating two) and their relative impact on the visibility of a setup.

This perfect virtual grating setup includes a parallel, monochromatic wavefront, no scattering processes and two gratings with a perfect continuous lamella phase grating. As a model for the gratings both microscope and artificial images of distorted and undistorted structures can be used. Gray-scale images are chosen as a 3D representation, where the gray level indicates the relative absorption of the grating at the particular spot in the image plane. Whilst cumulative absorption is easily predictable for gratings with equal electroplating height, control of a single lamellas' transparency can also be used to model gratings that are non-uniform along the beam axis. To obtain those gray scale representations of gratings, regular SEM and microscope pictures are taken. Brightness and contrast are adjusted in such a way that the brightest and darkest parts correspond to the desired absorption of the grating.

Starting with deformed FEM models, this can be achieved by creating a few grating slices through the FEM model perpendicular to the beam axis with small shifts to each other (see fig. 4.7). Those 2D slices are superimposed so that at the lamellas' edges a transition from black to white emerges that simulates different gold structure height and thus differences in absorption. This model does not take into account the lateral dimension of the Talbot pattern along the beam axis. It just assumes that the entire grating with all containing slices are placed at the specific (fractional) Talbot Distance. Such a grating model roughly equals a transmission image from a single grating, integrating the absorbing parts along the beam axis. This also assumes a perfectly oriented grating which has no deviation from the plane of the Talbot image (i.e. no wafer bow or warp).

An example of such a conversion of microscope images into visibility maps can be seen in fig 4.8. The simulations confirm that gratings with those deformations will strongly degrade visibility when used in an imaging setup.

## 4.8 Simulations as a tool for layout generation

To demonstrate the combination of both FEM geometric simulation and visibility predictions from distorted images, unit cells are picked due to their independent cells, which simplifies the boundary conditions of the simulation. And with the visibility simulations, typical grating errors like the e-beam stitching zones can be reproduced (see fig. 4.9). The combination of both tools is supposed to demonstrate that mechanical simulations can be used as a fast prediction tool for grating layouting regarding their imaging performance.

As a showcase for this rapid prototyping approach, the complete setup of a unit cell design is simulated and its visibility map compared to results from the beamline. To simplify the deformation simulations, capillary forces between the unit cells are neglected, effectively isolating the cells from the outside. This isolation is used in the further processing, as only one cell is simulated and then copied to create results for large areas. In the examined case, a unit cell with  $4\text{ mm}^2$  area is investigated, but slightly larger areas would also be possible, up to an area of about  $1\text{ cm}^2$ . Above those, a drastic upgrade in computing power (especially memory) for the large matrices (about 10 Billion entries) is needed.

Real unit cell structures are measured at the Topo Tomo Beamline at the ANKA facility of the KIT [2]. Gratings with a period of  $2.4\text{ }\mu\text{m}$  are tested using a detector with an effective pixel size of  $6.6\text{ }\mu\text{m}$ , allowing a field of view of  $17\text{ mm} \times 10\text{ mm}^4$ . As its pixel size is rather small compared to the grating period, the setup is well suited for the characterization of small-to-medium sized errors in the range of only a few periods. Narrow x-ray bands with energies of  $1.5\text{ keV}$  to  $30\text{ keV}$  as well as the full spectrum can be used. The typical energy at this setup is  $25\text{ keV}$ . A two-grating imaging system is installed with the absorption grating placed in the first Talbot order. This

---

<sup>4</sup> The actual field of view for grating characterization also depends on the divergence of the beam, which for synchrotron sources is typically neglectable

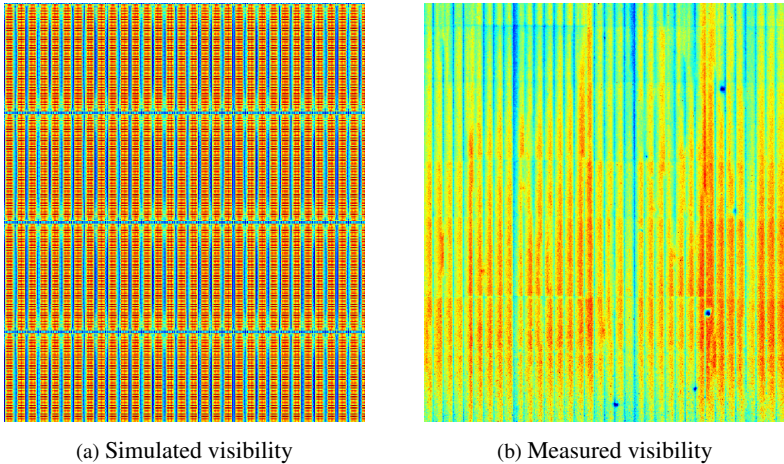


Figure 4.9: Comparison of a simulation of the visibility map of a unit cell geometry for a binning size of two periods per pixel (left) and real measurement results (right). The colorbars are scaled in arbitrary units, as for the experimental results the visibility is reduced by a range of additional factors that are not included in the simulation. The qualitative results match nicely, where also horizontal distortions are suppressed in contrast to vertical fringes. Unit cell size is 24 periods which corresponds to a grating area of  $60\ \mu\text{m} \times 600\ \mu\text{m}$  for a  $2.4\ \mu\text{m}$  grating.

beamline is used for continuous grating inspection and subsequent improvement steps [48].

A comparison of the simulated and measured results (see fig. 4.9) shows that the combination of mechanical simulation and artificial visibility calculations on semi-transparent 2D grating slices can be a valuable tool for the layout testing prior to mask and grating fabrication as it can predict visibility distributions beforehand. This will help to identify grating layouts that can withstand temperature differences during processing. But one also has to keep in mind that absolute visibility values cannot be drawn from those simulations, as a wide range of other factors is not accounted for. Those factors include tilting and bending of the gratings (can be included but has to be measured very carefully beforehand), local resist and mask errors, global

distortions in both gratings (large areas cannot be simulated mechanically) and especially x-ray tubes chromatic aberration as well as divergent beams.

## 4.9 Solutions against resist deformation

Over the years, a number of different approaches have been tested to meet the challenge of fabricating defect free high aspect ratio grating microstructures:

- Kenntner [62] investigated into highly resistant mechanical configurations of the resist mold to minimize deformation as well as to maximize the flux
- Meiser [58] as well as Kenntner were working on optimizing the lithography parameters to minimize stresses induced by the processing of the gratings prior to electroplating
- Koch [47] showed that by matching the CTE of mold and substrate via replacing silicon with polyimide or graphene, the CTE mismatch induced stresses during all process steps with elevated temperature could be reduced significantly.
- Marschall et al. introduced freeze drying [46] to x-ray phase contrast gratings and was able to demonstrate the flawless fabrication of gratings with extremely long unsupported lamellae. Unfortunately, these tended to bend during electroplating.
- Weitkamp et al. [91] demonstrated silicon molds for grating metalization, whose mechanical stiffness helped to overcome deformations. Nevertheless, high aspect ratio (>50) fabrication in silicon is yet not feasible, although the technique is much more mature due to the large MEMS industry and its use of anisotropic silicon etching.

Kenntner [45] also mentions a possible step towards defect free gratings. For a single grating, a gold electroplating bath operating close to room temperature has been tested and showed promising results. This was at least partly attributed to the reduced thermal stress exerted on the grating. But while the imaging results for that single grating looked promising, the electroplating results had a rather poor quality.

Therefore, one main aspect of the thesis is to prevent grating distortions by creating an electroplating bath that significantly reduces thermally induced strain in the grating. This is to be achieved by operating the electroplating bath at a temperature of 20 °C to 30 °C (i.e. room temperature).

A second step for a better understanding and control of grating fabrication is more and profound data on the resist material. For SU8 it was shown by Feng [24] that its mechanical parameters can vary strongly, depending on the process parameters. Furthermore, a modified version of SU-8 called mr-X has been used by Kenntner, Meiser and Koch that so far has only been tested very little concerning its fundamental mechanical parameters [51]. So, its confinement with SU-8 parameters has yet to be proven.

Finally, with the availability of the new, high contrast mr-X resist and to optimize the outcome of the electroplating process, a better understanding of the interplay of electroplating and the lithography parts is sought.



## 5 Mechanical resist behavior in the electroplating solution

A deeper understanding of the resist material and its behavior in different surroundings can help to suppress or overcome unwanted deformations. This chapter will first highlight a variety of test methods to gain insight into the mechanical properties of the new resist material mr-X. Afterwards, these findings will be discussed in regard to the fabrication of microstructures.

### 5.1 Tensile tests on mr-X resist

One of the very basic ways to gain information about the mechanical properties of a material is to perform tensile tests. In this test, specimen with normed shapes are pulled apart at a predefined speed while the resulting force is measured. Typical sizes for pull test samples (length and width in the range of a few cm, thicknesses larger than 1 mm) cannot be used in the case of tensile specimen fabricated by lithography, as the required thickness is not reachable with the LIGA process. Therefore, a testing machine specifically designed for measurements on sub-mm scale samples is employed. This testing machine for micro specimen has been reported and assembled by Teutsch [87].

The sample geometry to be put into the testing machine consists of flat resist specimen with a height of  $100\mu\text{m}$ , a bar width of  $300\mu\text{m}$  and a bar length of 2 mm with rather broad shoulders and short grip sections. The geometries are defined in such a way that they can be fabricated via LIGA or other lithography techniques (e.g. laser structuring or UV-LIGA). Tests on

smaller samples with 100  $\mu\text{m}$  bar width and slightly different geometry confirm that within the examined range there are no size specific dependencies of Young's Modulus or the other measured parameters.

The testing machine consists of a linear stepping motor, a 40N load cell and a long working distance microscope including a CCD camera. The stepping motor and the load cell apply and measure load and the microscope is supposed to measure strain. Image acquisition data from the CCD camera is linked with the load cell via a LabVIEW program to ensure temporal conformance between force and strain measurements. During one measurement run a motor speed of 5  $\frac{\mu\text{m}}{\text{s}}$  is set and the CCD camera and force measurements are started in parallel, with a rate of one dataset (image or force reading) per second. The strain rate is kept constant during the experiments as the correlation between strain rate and the mechanical behavior can be quite complex [74]. In order to evaluate the strain, image autocorrelation is applied to the set of pictures taken during one measurement.

In some samples, there is a small nonlinear deviation at the beginning, which is caused by minor relative movements of sample and clamp. To exclude any of those nonlinear effects, only the linear section in the region of 1 % to 3 % of elongation is used for the calculation of Young's Modulus. The running in regions are excluded from the calculations and also not taken into account for the correction factor for elongation. Also, a correction factor for the real size of the bar of each sample is factored in. Finally, Young's modulus is calculated from the graph as it can be approximated by the gradient of the stress strain graph in its first linear region. Further extracted parameters are ultimate tensile strength (UTS), which is calculated from the maximum value of stress reached, and maximum elongation which gives the maximum strain including deformation before failure.

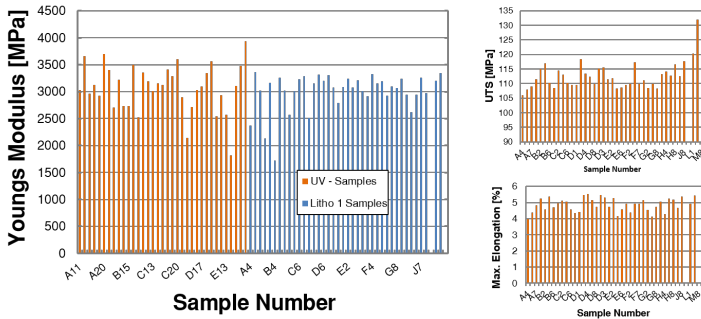


Figure 5.1: Comparison of Young's modulus, max. elongation and ultimate tensile strength for UV- and x-ray structured samples.

## 5.2 Mechanical parameters of mr-X resist

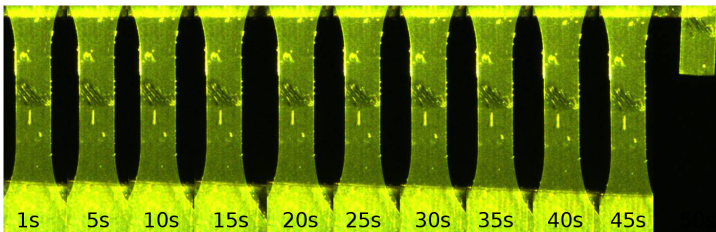
The first set of measurements is made with samples that have been fabricated via UV lithography with the direct laser writing technique. The samples differ in dose, having a total of 5 different dose values. However, as no correlation of dose and mechanical properties for UV laser lithography can be found (see fig. 5.1), this variable is disregarded from here on. The reason for not seeing any differences could be that for the patterning a dose threshold is exceeded even by the lowest exposition times used. Lowering the dose even further results in non-conformal structures that cannot be tested properly.

Even when reviewing just the results of one dose value, the samples scatter quite drastically with Young's Modulus going from 2000 MPa to 4000 MPa (see fig 5.1). Also, tensile strength and maximum elongation share an unexpectedly high standard deviation.

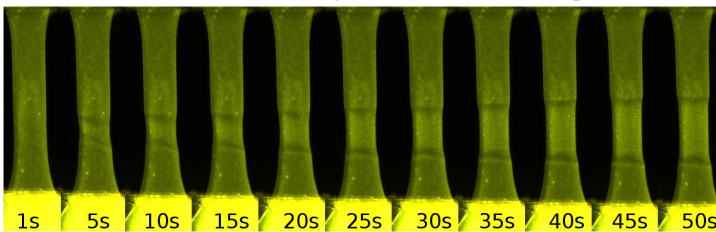
To determine whether intrinsic sample inhomogeneities or machine errors account for the variation, two measures are taken.

At first is to track visible damages on the samples surface and see if they have an impact on the data. Second is to examine the samples and to track

possible inhomogeneities that are optically visible in the fracture images. With this a contribution of intrinsic errors might be detected. Due to the small size of the samples manually handling them is difficult and thus some show scratches on their surface. Those marks are tracked in the image series of the measurement and a comparison between scratch and fracture position is made. Out of the 10 samples that show scratches on the surface, none has any correlation between crack appearance and fracture position. All fractures are happening in places that have before seemed unharmed. An example can be seen in the upper row of fig. 5.2.



(a) Time series of images from a scratched sample



(b) LIGA fabricated sample showing plastic deformation

Figure 5.2: Time series of two different pull test samples. The upper sample is a showcase that surface scratches do not alter the fracture behavior. The lower image series demonstrate necking and cold drawing of a sample.

Regarding inhomogeneities incorporated into the sample, a thorough investigation of all samples prior and during the measurement does not reveal a single set where a clear correlation between a visible inhomogeneity and the fracture behavior afterwards can be made. With both alternatives shown

to be unlikely, there are two more possible explanations: First are intrinsic inhomogeneities from either the resist material or inhomogeneous lithography. Both of them might produce samples with non-uniform mechanical properties that cannot be resolved optically. Alternatively, the spread could also hint to brittle fracture behavior [85]. In the following sections those aspect will be highlighted further.

As a consequence of this first set of experiments, it can be concluded that for a sufficiently accurate measurement at least 5 to 10 equally processed samples are needed for the extraction of mechanical properties. Young's modulus with  $3.0 \pm 0.5$  GPa in case of the UV structured samples is slightly higher than reported by Lemke [51], but it should be noted that the postbake temperature used ( $75^\circ\text{C}$ ) is higher than the  $65^\circ\text{C}$  reported. With 3.0 GPa it also matches the mechanical strength of SU-8 [24]. Tensile strength and max. elongation of mr-X have not been reported yet. Measured values of 4 % to 5 % of elongation are in the range of what has been reported for SU-8 (see table 4.1). Maximum tensile strength on the other hand is almost double for mr-X, with  $110 \pm 5$  MPa for mr-X and only 60 MPa for SU-8. This already gives a hint for the increased mechanical stability seen in grating production when switching from SU-8 to mr-X by Kenntner [45].

After the initial investigation of UV structured samples, x-ray crosslinked samples are examined to test whether these findings also apply for the process conditions found in grating fabrication. LIGA structures are produced at the *Litho 1* beamline using only one dose value which corresponds to the exposure conditions of gratings (bottom dose of  $140 \text{ mJ}/\text{mm}^2$  and a top dose of  $500 \text{ mJ}/\text{mm}^2$ ). Whilst Young's modulus and tensile strength have almost the same magnitude and only a fractionally smaller standard deviation (i.e. less spread between similar samples, see fig 5.1), the non-linear part of the stress strain graph reveals ductile behavior for about 50 % of the samples. It can be attributed to plastic deformation of semicrystalline mr-X components, as it's stress strain examination has some characteristic features [11]:

- Deformation at start is elastic until 3 % elongation (in case of mr-X)
- Two distinct yield points are visible
- Necking of the sample starts with the first yield point
- The necking region propagates along the specimen

This plastic behavior for the samples can be ascribed to localized strengthening due to the orientation of polymer chains along the drawing axis [9]. The mechanical properties of semicrystalline polymers is highly dependent on the degree of crystallinity.

As a control to test the setup for consistency, a third kind of samples is tested which have been exposed with higher energy x-rays but an equivalent dose at the *Litho 2* beamline. These samples (see fig 5.3b) have no signs of

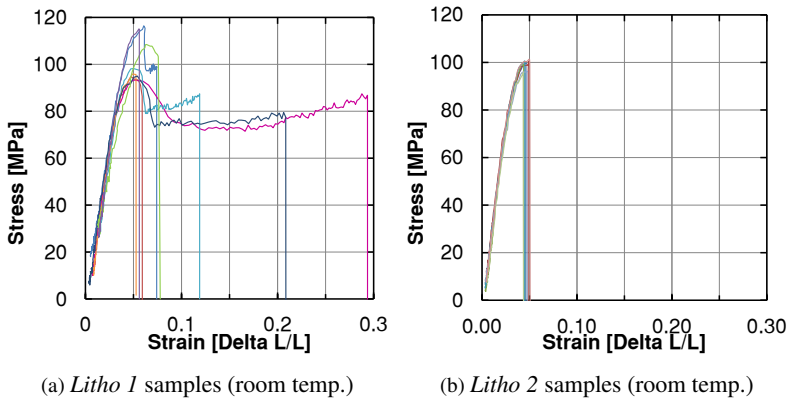


Figure 5.3: Stress strain graph of some samples exposed at the lower energy *Litho 1* and higher energy *Litho 2* beamline. *Litho 1* samples (left) show big variance with an additional change in material behavior. *Litho 2* samples (right) in contrast are extremely consistent.

necking or sheer yielding but only the typical linear elastic region of brittle polymers. So, specimen that have been treated exactly the same with the exception of the x-ray source show highly different mechanical behavior.

This leads to the conclusion that the root of these phenomena has to be the lithography step. The results from the stress-strain experiments also confirm that the measurement setup used is capable of repeatedly measuring tensile samples without much inner sample spread, as seen in the *Litho 2* samples. It can further be reasoned that strong variations in the mechanical properties, as seen in the UV samples, are most likely not due to inhomogeneities of the resist material. Instead, with some confidence the origin for mechanical variance is found in the exposure conditions especially at the low energy beamline *Litho 1*. One way to get mechanically better-defined resist material is to homogenize the exposure conditions.

To confirm the findings of the stress strain examinations, also the fracture surfaces (fig. 5.4b) are studied via scanning electron microscope (SEM). Whilst the brittle samples all show rolled up lamella of resist material, the others have two distinct regions with different appearance. The upper half (pointing towards the top of the resist) of the fracture surface usually appears smooth on a micrometer scale. In the lower part interference bands or stretches [75] can be seen, which are typical of brittle fracture of glassy polymers [28]. But also crazing and necking [11] can be observed in the SEM images of some samples. The fracture images indicate that complete resist failure is initiated at the lower surface. The resists bottom face is in contact with the substrate (oxidized Titanium sheet), which has a rather rough finish. This roughness creates a vast amount of nanometer sized notches into the resist which can act as stress concentrators. But the rough bottom surface cannot explain the spread in the measured parameters, as for the *Litho 2* samples the same substrate has been used.

In summary, it can be concluded that for samples from the low energy beamline *Litho 1*, different mechanical behavior can be observed. Within this sample set, brittle fracture as well as plastic deformation can be observed. Furthermore, the samples showing plastic deformation seem to incorporate two distinct regions of mechanical behavior, with brittle fracture in the part with higher exposure dose and plastic deformation for the part that has a

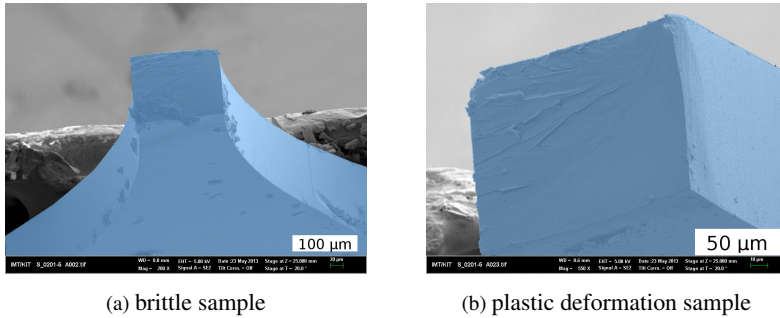


Figure 5.4: Comparison between a brittle sample and a sample showing plastic deformation. The right picture shows signs of necking, crazes and at least partly brittle fracture.

60 % lower exposure dose. These findings are typical for epoxy materials, as their mechanical behavior is dependent on the degree of crystallinity, which is directly linked to the crosslinkage ratio. And x-ray exposure of polymers typically leaves a gradient of exposure from top to bottom (called top-to-bottom ratio) [41]. So, the presumably harder upper parts show brittle fracture behavior and the less crosslinked lower parts are deforming plastically. It further seems that the dose used is at the threshold of the transformation from plastic deformation to brittle fracture, so that the variations in exposure and dose yield different mechanical behavior for samples with nominally identical exposure conditions. The *Litho 2* dose, while nominally smaller than the *Litho 1* samples dose<sup>1</sup>, in total exceeds this threshold, and therefore all of the samples processed there show brittle fracture.

At room temperature, the samples yield a Young's modulus of  $2.9 \pm 0.4$  GPa for both beamlines (with small differences in variance), which is slightly lower than the values found by Lemke [51]. Plastic deformation and also to a lesser extent tensile strength are dependent on the kind of sample. Higher

<sup>1</sup> It has to be noted that dose calculation for x-ray lithography has to be done indirectly, as several mechanisms are included in photoacid generation. As all these models have a rather large error margin, exact dose comparisons of both beamlines are not possible.

tensile strength is found in brittle samples and lower tensile strength in samples with a pronounced plastic deformation regime.

### **5.3 Impact of humidity on mechanical stability of mr-X resist**

Although it has been shown in section 4.6 that water incorporation does not contribute much to grating deformation, Schmid was able to demonstrate that even minuscule amounts of water can make a difference regarding the mechanical properties of SU-8 [80]. To test the influence of water on the mechanical performance of mr-X resist samples, a set of test structures from *Litho 1* is immersed in deionized water for different periods of time. For an estimation about the timescales necessary for these experiments, a small study on water uptake is done. To also detect evaporation of water molecules that have diffused into the mr-X matrix, the samples are taken out of the immersion bath after reaching saturation (two days of immersion or more) and their weight is measured until the initial value was reached again. In contrast to water uptake, evaporation is faster by several magnitudes (minutes instead of days), so for intermediate weight measurements drying and weighting times are kept as low as possible. Overall water uptake is 2 % to 3 % of the total mr-X mass. It shows that the saturation point for water uptake is after two days of immersion for 100  $\mu\text{m}$  thick samples. But as 90 % of weight gain occurs within the first day, this is chosen as the appropriate time scale for immersion. It also represents roughly the average time that gratings undergo immersion in the standard electroplating bath. Therefore, to analyze the mechanical input of water diffusion into resist, pull test samples are immersed into deionized water for one day and measured right after extracting them from the liquid without further drying. It is assumed that surface wetness has no effect on any of the examined mechanical parameters. For ease of handling, deionized water is used instead of electroplating solution. Additionally, samples after only one hour of im-

mersion and samples without immersion are tested to crosscheck the results. The results indicate that water uptake plays no role for the mechanical behavior of resist in a wet chemical surrounding like an electroplating bath. Young's modulus and UTS are not affected at all by immersion and only maximum elongation shows a slight increase, but still well within the error range. Overall, water itself as a chemical surrounding is not considered a special liability for the mechanical stability of mr-X microstructures.

## 5.4 Heated tensile tests on mr-X resist

To confirm the semicrystalline properties of the material, the temperature dependence of *Litho 1* tensile test specimen is investigated. The samples are heated indirectly through infrared radiation. The temperature sensor is placed in close proximity to the sample holder to ensure that only a small temperature difference between the sensor reading and the actual sample remains. As measurement times are usually in the range of 1 min to 3 min a temperature gradient between sensor specimen of  $\pm 1^\circ\text{C}$  is accepted for this span of time.

At room temperature, it has been shown that the samples feature significant standard deviation regarding their mechanical strength and approximately 50 % of the samples have some degree of plastic deformation. This behavior changes drastically when going to a temperature of  $50^\circ\text{C}$  or above, where all of the samples undergo plastic deformation and a high percentage even reaches the region of work hardening<sup>2</sup> (see fig. 5.5). Both Young's modulus and maximum elongation indicate systematic changes when going from  $50^\circ\text{C}$  to  $60^\circ\text{C}$  (see fig. 5.6). Young's modulus decreases slightly with increasing temperature where only the rate of decline grows for the  $50^\circ\text{C}$  to  $60^\circ\text{C}$  region. The most prominent change is observed in the percentage

---

<sup>2</sup> For polymers this effect is typically not called *strain hardening* but *drawing*, as it is utilized to strengthen polymer fibers during fabrication. But as the effect in this case closely resembles the deformation processes found in metals, *strain hardening* is used instead

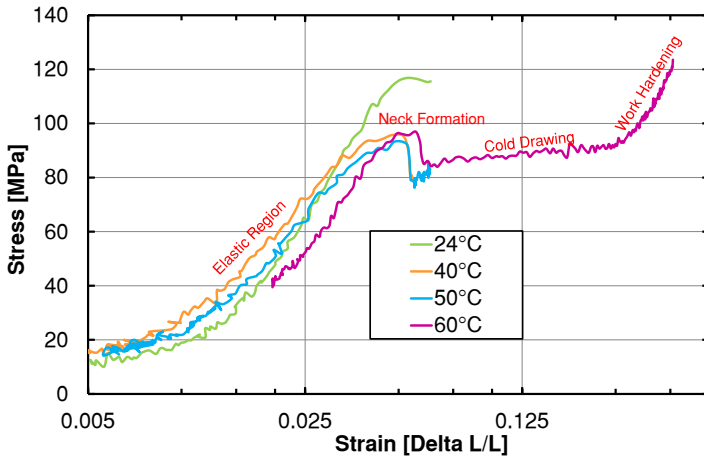


Figure 5.5: Four typical stress strain graphs for different temperatures, showing the continuous evolution of plastic deformation behavior with temperature

of samples breaking with plastic deformation. While only 30 % to 50 % of samples exhibit plastic deformation below 60 °C, this fracture behavior can be observed in all samples above this threshold.

This leads to the conclusion that between 50 °C to 60 °C the transition from brittle to ductile material can be observed with the tensile tests. This temperature range corresponds to the glass transition temperature of uncrosslinked mr-X and SU-8 [24], whereas  $T_G$  of fully crosslinked SU-8 is typically in the range of PEB or hardbake temperature. Those results clearly indicate that the current process parameters (especially time and temperature of the post bake as well as *Litho 1* lithography) yield samples that contain significant amounts of uncrosslinked material.

## 5.5 Thermal expansion of mr-X resist

As the special testing machine combines both accurate temperature readings as well as a precise elongation measurement, it is also employed to deter-

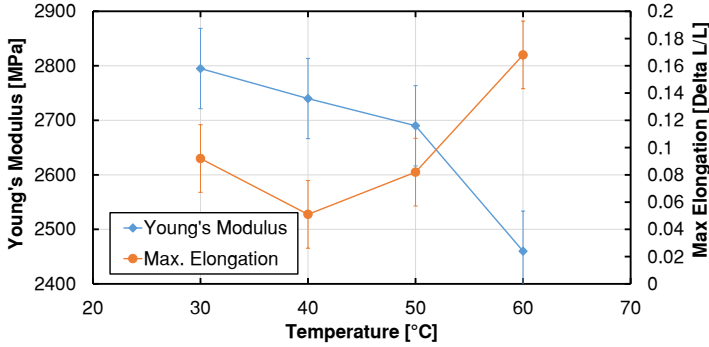


Figure 5.6: Temperature dependence of Young’s Modulus and Maximum Elongation for mr-X resist. A significant change in mechanical behavior at 60 °C can be seen.

mine the coefficient of thermal expansion (CTE) of crosslinked mr-X. For this purpose, the samples are only fixed in the upper holder so that the lower part can move freely. Then the heating lamp is switched on and the image recording is started. This test is redone several times to reduce inter-sample spread.

The coefficient of thermal expansion is calculated to be  $35 \pm 15$  ppm/K. For this calculation, it is assumed that the measured expansion of surface points corresponds to a linear expansion of the material due to the elongated sample shape (instead of a volumetric elongation). The blue strain graph in fig 5.7 shows a typical result for a sample undergoing thermal expansion in the testing machine. In this graph, additional periodic fluctuations are present which can be attributed to the image analysis system. As the expansion over the temperature range is rather small in absolute terms, minor variations in a single pixel already influence the calculated results and create those wavy graphs. This also highlights that the current setup is only just capable of measuring thermal expansion which also explains the rather large error margins. Nevertheless, the value corresponds to the thermal expansion coefficient of SU-8, which was reported as 52 ppm/K [54].

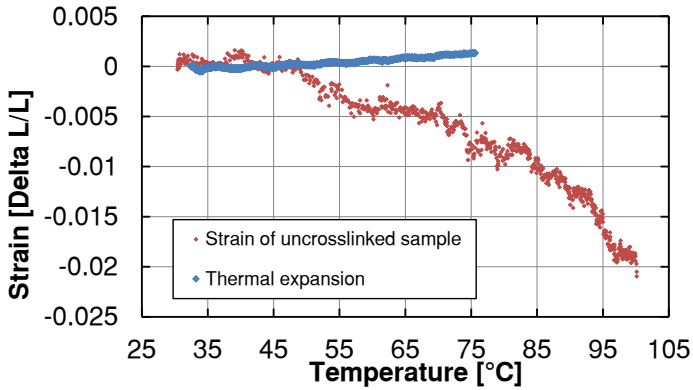


Figure 5.7: Strain graphs of two samples. Blue graph shows the thermal expansion of an already crosslinked sample with a slope of  $35 \pm 15$  ppm. The red graph is a sample undergoing thermal expansion and shrinkage at the same time.

One sample is also examined while being heating up, whereas for the other samples image acquisition has first been started when the peak temperature is reached. So, thermal expansion has only been measured during the cooling phase. This heated sample actually decreases in size during the heating up phase and its expansion is not linearly correlated with temperature. Contraction starts at around  $50^\circ\text{C}$  and its rate still grows when reaching a temperature of  $100^\circ\text{C}$  (see fig 5.7). And the effect is about one order of magnitude larger than the typical thermal expansion experienced in the other samples. But it is roughly in the same region as crosslinkage induced shrinkage. This behavior leads to the conclusion that for this sample additional crosslinkage with subsequent shrinkage of the resist can be seen. So, for this sample, the CTE measurement effectively acts as a second postbake step. To initiate crosslinkage in samples that have already seen the postbake step, two separate processes must have happened prior to the expansion experiment. First is the presence of uncrosslinked material which can move freely (see section 4.3.1). As discussed in chapter 5.2 the existence of uncrosslinked material

is considered to be likely. Second is the existence of enough residual photo acid to initiate crosslinkage. This photo acid can either be still remaining from the first exposure or it can be generated by additional unwanted exposure steps. If PAG that has not been activated by x-ray lithography is still existent in the material and there are sufficient sites to crosslink, additional polymer network will be generated. One particular process that applies dose in grating fabrication would be the additional reactive ion etching (RIE) before electroplating. During this step, the wafer is exposed to ions stemming from a plasma cloud. This plasma emits strong UV radiation which should well enough suffice for a release of photo acid in already developed parts. For grating fabrication and application, it has to be kept in mind that residual uncrosslinked polymer can still introduce resist shrinkage, which could lead to serious deformation even after electroplating.

## 5.6 Differential Scanning Calorimetry

To verify the results obtained in the previous chapter regarding the uncrosslinked material in the remaining resist pattern, Differential Scanning Calorimetry (DSC) measurements of exposed resist are performed. In a DSC experiment, the heat flux through a sample is measured during a heating or cooling process. Changes in the heat flux can be attributed to endo- or exothermal processes like chemical reactions (e.g. crosslinkage) or also physical processes like phase transitions (e.g. glass transition). Whilst mechanical pull tests can give insight into the physical state of the sample, DSC can be a tool to characterize the chemical state of the resist. This can be valuable, as there is a strong connection of mechanical properties and the chemical processes beforehand. Also, glass transition temperatures of unexposed and exposed material can be investigated with this method. But due to the change in heat flux during glass transition and the energy dissipation or consumption during a chemical reaction, glass temperature transition coupled with crosslinkage cannot be distinguished with this method. Nev-

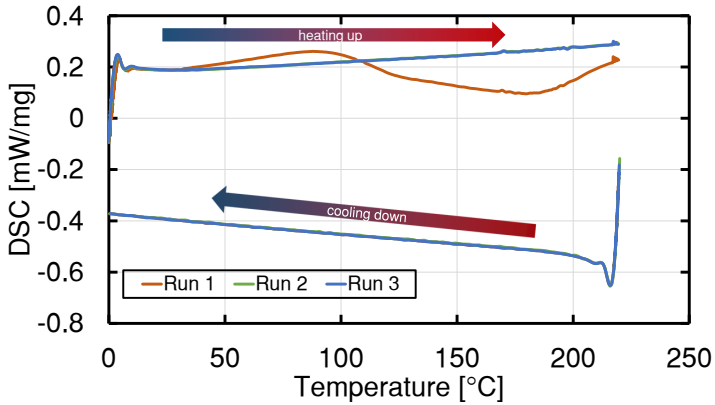


Figure 5.8: DSC measurement of mr-X resist samples. Three subsequent measurements are done (labeled run 1-3), each consisting of a heating and a cooling step. Only after the third cycle, the sample is extracted. Data from run 2 and 3 are almost identical, so only run 3 can be seen in the graph.

ertheless, it gives valuable information regarding the processes happening at elevated temperatures as well as molecular reactions when measuring the same sample with cyclic tests.

For the experiments about 7 mg of resist material are put into small beakers and then the change in heat flux in a Netzsch DSC 204 Phoenix calorimeter is measured. By using cyclic testing, remaining non-crosslinked material content can be detected. Each cycle consists of a temperature ramp up to 220 °C with a temperature rise of  $10 \frac{\text{K}}{\text{min}}$ , 5 min holding time and a reverse ramp down to 0 °C at a speed of  $-10 \frac{\text{K}}{\text{min}}$ . This cycle is repeated two more times to eliminate any remaining uncrosslinked material. The results from a sample exposed with standard dose at the *Litho 1* beamline show an endothermic reaction starting around 50 °C (see fig 5.8). It is superimposed by an exothermic peak around 100 °C during the first heating up ramp. The endothermic drop can be attributed to the glass transition of uncrosslinked or only partly crosslinked material. The peak is an exothermal reaction caused by a completion of the crosslinkage of the material, lasting until 200 °C,

where crosslinkage inhibition is reached [73]. All endo- and exothermal peaks vanish when the same sample is cooled down and scanned a second (and third) time, which is a clear sign for full crosslinkage after the first heating run. There is also no glass transition visible, therefore it can be concluded that during the first heating the sample is fully crosslinked within the holding time of 5 minutes, shifting  $T_G$  above the measurement range of 220 °C.

One drawback of the method is that the measurement signals for glass transition and thermal crosslinkage both start at roughly 50 °C, which makes it difficult to distinguish between both phenomena. But as they are chemically closely entangled, the appearance of one will always be a hint for the second, so it can be used for qualitative demonstrations of ongoing physico-chemical reactions. For a precise measurement of the amount of uncrosslinked material, a different method like thermogravimetric analysis would have to be used.

## 5.7 Demonstration of a gratings mechanical instability

As an example of how resist deformations can affect the x-ray imaging process itself, highly sensible structures are used in a phase contrast setup. The in-situ deformation of a resist only grating is done by thermal heating through the incident x-ray illumination. For this purpose, grating resist structures with a period of 5.4  $\mu\text{m}$  are employed as G1 in a symmetric three-grating setup (see section 7.4.1). The height of the resist structures (in this case acting as phase shifting structures) is 200  $\mu\text{m}$ , which corresponds to a phase shift of approximately  $4\pi$  at 20 keV. Its phase shifting capability can be seen in the stepping curve (see fig:5.10, top blue line) as well as the visibility map (fig. 5.9). As the top blue stepping curve resembles a sinusoidal signal, significant signal for phase shift measurements is available. Its mean visibility of 0.032 is only slightly smaller than those measured with other

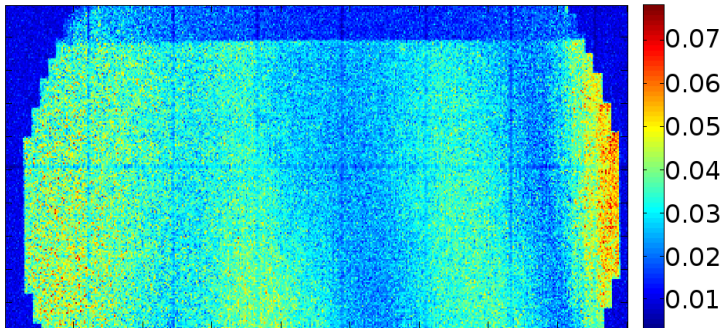


Figure 5.9: Visibility map for a grating setup using a G1 grating, where the grating lines are made of mr-X material instead of nickel. Mean visibility is only slightly smaller than comparable nickel G1 gratings.

Nickel gratings in that setup, which during this testing series typically have visibilities of 0.07 to 0.1 for well aligned configurations. The biggest factor leading to the small visibility is presumably the lack of control of the absolute resist height, as it has not been intentionally fabricated for the purpose of being used as a G1 grating.

When measuring the resist G1 grating for a prolonged time (up to 60 min with shutter open), visibility drops down and especially the sinusoidal shape of the stepping curves becomes increasingly chaotic. This can be seen in fig. 5.10, where with increasing illumination time (top blue line: starting with illumination, bottom blue line: 1h of continuous operation) the intensity signal is getting more and more noisy and thus visibility is reduced significantly. It can be assumed that due to structural deviations phase retrieval is no longer possible. Those results show that for thermally unstable layouts and no additional support like incorporated metal, the heat generated at G1 is already enough to deform a resist only thermo-labile structure. It once again highlights the need for careful thermal treatment of the samples during all process stages (in this case even including the measurement setup). Prolonged exposure to radiation can even damage metalized gratings, as can

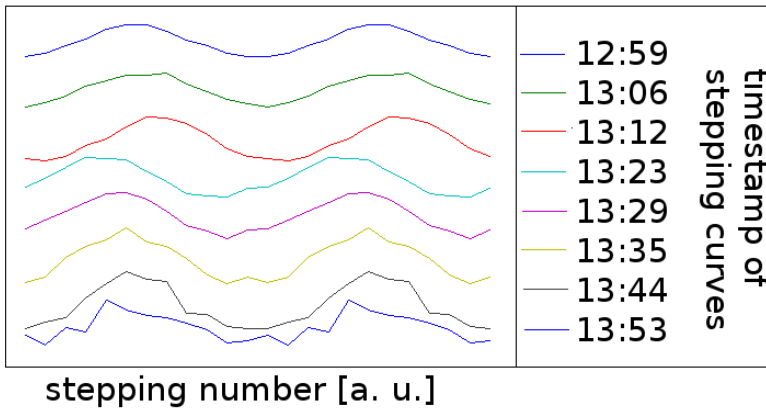


Figure 5.10: Series of stepping curves with their according timestamp. The y axis displays the x-ray intensity, but for better arrangement the stepping curves are plotted with an offset in the y-axis. All measurements are done within one hour with an almost complete loss of the sinusoidal shape of the stepping curve after one hour of continuous exposure.

be seen in fig. 5.11. This picture shows a grating that has been extensively used as a G0 grating in an imaging setup in close proximity to the x-ray source. The heat generated in the grating led to cracks and fractures, which were first observed as artifacts in imaging. For a future mass fabrication and application in medical diagnostics, it has to be ensured that material deformation (and also aging, which has not been a subject of this thesis) do not lead to a noticeable decrease in imaging performance.

## 5.8 Conclusions drawn from the mechanical characterization

The investigations on the basic mechanical properties of mr-X as well as its response to the physico-chemical surrounding found in the electroplating bath show that a tight connection between the resist processing and its

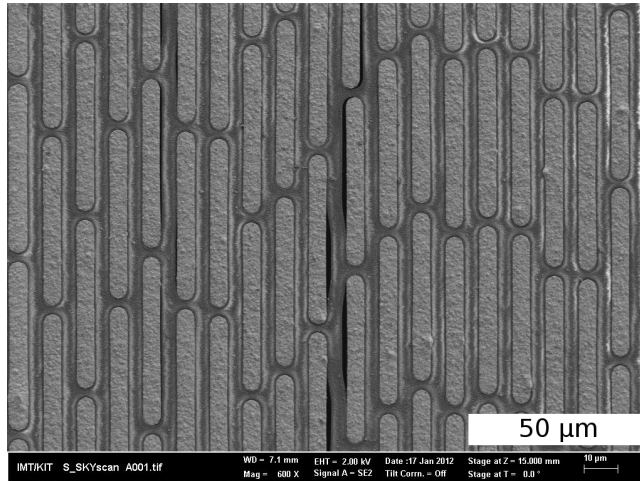


Figure 5.11: SEM picture of a grating showing deformations which first appeared during long time exposure to radiation when being used as a G0 grating.

behavior to the applied forces exists. Most notable for grating production is the pronounced two-region separation of mechanical properties found in *Litho 1* processed samples. As it has been tested thoroughly by Kenntner, Meiser and Koch that grating manufacturing at the *Litho 2* beamline is less favorable, it can be assumed that this material gradient is at least partly contributing to the preference for one beamline. For grating fabrication, partly uncrosslinked material with a slightly lower Young's modulus and the ability for plastic deformation can be of advantage. This softer material which is more likely to be found closer to the substrate helps in reducing interfacial stresses such as CTE mismatch or resist shrinkage. Similar to gluing of stress sensitive devices like MEMS [97], the existence of softer material close to the substrate can act as a stress relief region in the production of HAR gratings. It is accompanied by the stronger crosslinked upper part of the material, which yields enhanced mechanical stability for structural conformity. Only the combination of both mechanical zones might yield

structures that are best suited for HAR structure fabrication on substrates not CTE matched to the resist material [47].

This chapter has furthermore demonstrated that temperature has a strong impact on the mechanics of the crosslinked resist material. At a threshold of 50°, a change in the material is experienced, going from brittle to plastic deformation behavior. Even the heat generated in an x-ray setup is sufficient for material deformation. So, the development of an electroplating bath that operates well below the threshold of mechanical behavior change of 50 °C to 60 °C can be a significant step towards the fabrication of deviation free gratings. The liquid surrounding found in electroplating on the other hand has no significant impact on the mechanical properties of the resist.

In the following section, the electroplating bath's temperature will be tackled by demonstrating the development of an electroplating bath working close to room temperature to overcome thermal stress and deviations in the resist.

## 6 Room Temperature Gold Electroplating

With the LIGA technique, the absorbing part of the grating is produced via electroplating. To do this the substrate to be electroplated is placed in a solution containing dissolved metal ions. These ions are reduced by electrical current at the conductive surface to form a metallic layer on top of the substrate. With this technique, thick layers of metal can be grown, which makes it ideal for the electroforming of LIGA molds.

Electroplating of thick (larger than 20  $\mu\text{m}$ ) microstructures created by x-ray or UV lithography has some distinct differences to regular electroplating of unstructured surfaces. Plating as performed in the semiconductor [79] or surface finishing industry is optimized towards high optical quality (which is closely related with low surface roughness) and also towards defect free structures for small aspect ratios ( $<1$ ). LIGA electroplating on the other hand has to deal with strong diffusion limits in the resist mold cavities, which are getting harder to overcome with increasing aspect ratios [81]. Those large diffusion distances need specific countermeasures usually not seen in other plating fields [77]. After introducing the standard electroplating bath for LIGA parts at the IMT in chapter 6.1, issues concerning electroplating at low temperatures will be theoretically deduced in chapter 6.2.

Chapter 6.3.1 will furthermore highlight the impact of bath temperature variation on various plating processes and will present specific countermeasures to overcome the prevailing negative effects. In the final chapter 6.4, experi-

mental results for the electroplating of different samples will be shown and discussed regarding their plating quality.

## 6.1 Standard LIGA electroplating

The state-of-the-art LIGA electroplating bath used for grating fabrication has been described in detail by Dambrowsky [15]. The established gold bath has been in constant use for the fabrication of all grating structures except for phase gratings, which are electroplated in a nickel sulfamate bath. This standard gold bath exhibits excellent microscopic throwing power as well as fairly good macroscopic throwing power and a not too pronounced tendency for the bath tub effect. As a downside, the electroplating bath's operation temperature of 55 °C means that thermally driven stress can lead to deformed structures.

### 6.1.1 Micro throwing power

An electroplating bath used for the fabrication of microstructures needs to be able to electroplate structures without local and macroscopic variations in height. Local height variations are caused by the inability of a bath to level parallel growing surfaces in a microscopic area. This ability (or the absence of it) is called *micro throwing power*. If a bath has insufficient micro throwing power, microstructures that are composed of separated trenches or voids can show a blotched appearance macroscopically. This is caused by rapid growth of metal in some of the cavities, thus creating strongly differing metal heights over the entire plating area. In the case of blotched appearance of gold LIGA structures, the root cause can be:

- non-uniform nucleation at the electroplating start and subsequent different growth rates of the gold layer
- residual resist at the bottom of the trenches
- a bath operated at wrong plating conditions

For electroplating usually only samples that are optically almost flawless are chosen, which to a certain extent excludes faulty resist mold. But one has to keep in mind that most of the previous steps provide only limited access for grating inspection and not all issues can be surveyed optically. So, when seeing such a surface with large height variance, one has to keep in mind that this does not necessarily have to be down to bad micro-throwing power of the bath.

### 6.1.2 Macro Throwing power

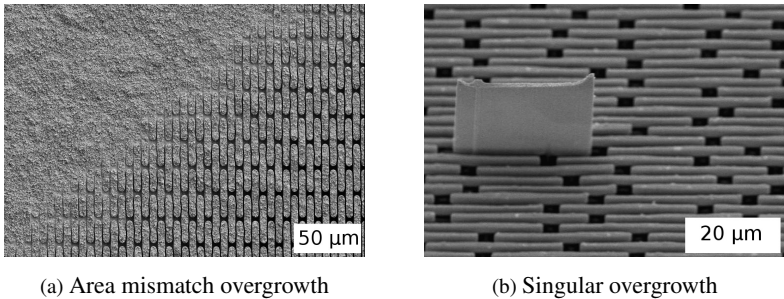


Figure 6.1: Two types of possible overgrown structures stemming from different error sources. Area overgrowth is caused by false estimations regarding the electroplating rate, whereas singular overgrowth is a result of a bath not suited properly for microstructure electroplating.

Whereas singular overgrowth (see fig. 6.1b) is strongly related to a bath's micro throwing power, *Macro Throwing Power* typically shows in the overgrowth of whole areas on a sample. Area overgrowth is a phenomenon mostly related to differences of calculated and real electroplating area, which is more likely in a lab environment with larger process tolerances. Depending on the duration of electroplating and the applied current, in some areas the metal will rise above the upper edge of the resist mold, spill onto the mold and cover the entire area (see fig. 6.1a). Overgrowth typically appears first at the borders of the structured area. As a rule of thumb,

electroplating has to be stopped when the calculated average electroplating height is 10 % to 30 % below the resist surface, depending on the typical height variation of an electroplating bath. As grating fabrication by the LIGA process is still on the lab scale, design-, substrate- and process variations are rather large. This leads to inevitable differences in the conformity of the electroplating mold which also increases the tolerances of total electroplating area. The main impact on metal structure overgrowth comes from fluctuations in duty cycle (both locally and between samples). Variance in DC between different grating samples is  $\pm 0.1$ , especially if they use different masks but the same nominal period and duty cycle. This directly leads to metal height variations of  $\pm 10\%$ . In the case of tapered or twisted sidewalls the electroplating area even changes with ongoing electroplating, which makes a prediction even harder. Up to now overgrowth can only be handled by careful observation of the electroplated sample and its metal filling height. With enough experience regarding the electroplating system and the samples, the process can be stopped before overgrowth happens. As this heavily relies on the operator, this is not a desired work flow for small scale mass production. One possible approach is to use an integrated anode. Preliminary results on this can be found in appendix A.5.

Partial overgrowth is also affected by macro throwing power [70]. The better the electrolytes ability to level over large distances, the smaller is the disposition of the bath to yield samples showing the so-called bathtub effect. This effect describes the tendency for faster growth of peripheral structures, leading to a height distribution that in general has the shape of a bathtub [15]. Like shown in figure 6.2, the difference in height between the flat inner part and the rim of the bathtub can by far exceed 100 % or more, which would limit the average metal height to less than half the height of the resist mold. Therefore, a suitable electroplating bath has to show little or no bathtub effect. To reduce this effect, apertures can be used.

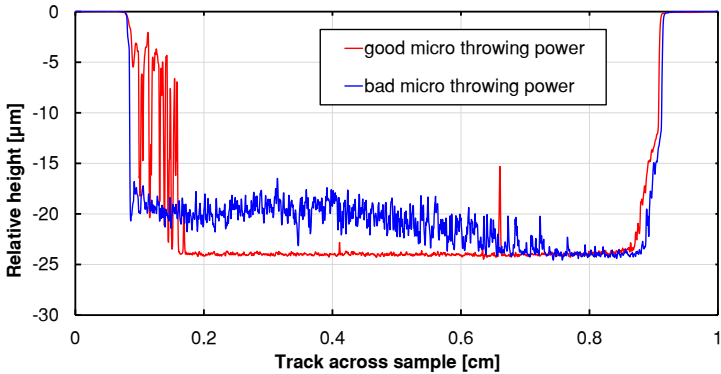


Figure 6.2: Cross section of height distribution of two electroplated samples measured with a line scanning height gauge. The two samples show the same macro- (both: bad) and micro- (red: good and blue: bad) throwing powers. Both samples exhibit a pronounced bathtub effect.

### 6.1.3 Standard bath composition

The standard gold electroplating solution is based on a commercial gold sodium sulfite solution containing  $100 \frac{\text{g}}{\text{L}}$  of  $\text{Au}^+$  and an undisclosed excess of  $\text{SO}_3^{2-}$ . To prepare the standard LIGA plating bath, 25 g/L of  $\text{Au}^+$ , 0.2 mol/L sodium sulfite, 0.1 mol/L Na-EDTA<sup>1</sup> and 0.3 mol/L of ethylenediamine (EDA) are added.

According to the standard a bath is set up like this:  $\text{Na}(\text{SO}_3)$  and Na-EDTA are dissolved in 1 L of deionized water. Ethylenediamine ( $\text{C}_2\text{H}_4(\text{NH}_2)_2$ ) is added under constant stirring. When the liquid has cleared, gold sodium sulfite solution is added. The plating bath is afterwards filtered with a 200 nm cellulose filter and subsequently heated to  $50^\circ\text{C}$  to reach the desired volume by evaporation. If any leveling agents or other additives are to be added, they are introduced after the standard bath preparation is completed. This usually also includes a running-in procedure with the electroplating of test

<sup>1</sup> Disodium salt of the ethylenediaminetetraacetic acid

microstructures to add additional contents of  $\text{Na}(\text{SO}_3)$  or Na-EDTA depending on the appearance of the electroplating <sup>2</sup>.

Ingredient	Concentration	Reason of addition
$\text{Na}_3[\text{Au}(\text{SO}_3)_2]$	$25 \frac{\text{g}}{\text{L}}$ of $\text{Au}^+$	main metal and conducting salt
$\text{Na}(\text{SO}_3)$	$30 + X \frac{\text{g}}{\text{L}}$	conducting salt, complex stabilizer, Redox-partner
EDTA	$30 + X \frac{\text{g}}{\text{L}}$	complexation of metal ions, complex stabilizer, leveling, conducting salt
ethylenediamine	$22.5 \frac{\text{mL}}{\text{L}}$	complex stabilizer, brightening agent

Table 6.1: Components of the standard electroplating bath

The operation parameters of the standard bath are as follows:

- Bath temperature is  $55^\circ\text{C}$
- Bath agitation is quite low, but not zero
- Current density is  $3.0 \text{ mA}/\text{mm}^2$
- Starting current is pulsed within the first three minutes to enhance nucleation.

With this bath, excellent plating results for most LIGA parts have been achieved. In case of grating fabrication, there are two drawbacks which make it necessary to develop a new electroplating bath: First, it yields deformed structures when parts are processed at the threshold of what is mechanically still stable after the development step. Thermal differences then lead to deformed structures. Second, the standard gold electrolyte cannot be operated at lower temperatures, as its micro throwing power is reduced dramatically, which leads to strong variations in grating lamella height.

<sup>2</sup> As this running-in procedure includes the addition of either  $\text{Na}(\text{SO}_3)$  or EDTA no exact value can be given for both contents.

## 6.2 Impact of lower temperatures on an electroplating bath

Despite being the main target for this thesis, lowering the working temperature of an electroplating bath is on no account an easy endeavor. The reason for being so challenging is the fact that temperature plays a major role in most of the critical processes involved in electroplating. Those processes are (amongst others) [3]:

1. Diffusion of the metal complex to the electroplating surface, especially in high aspect ratio (AR) structures
2. Metal absorption on the active surface
3. Surface diffusion of absorbed metal atoms
4. Reaction rate of the electroplating's redox reaction
5. Ion migration of all contained species
6. Conductivity of the electrolyte

In the following an estimation will be made concerning the prevailing effect when temperature is reduced for gold electroplating of microstructures. This should give a hint, what kind of adjustments are necessary for a working low temperature electroplating bath.

Diffusion is one of the most critical parameters for the electroplating of thick metal microstructures [52]. Especially in the case of high aspect ratios, agitation ceases at the resists upper edge, as current flow will not penetrate into the channels [68]. This diminishes the potential use of agitation to counter the temperature driven effects, as the diffusion distance is mainly defined by the depth of the grating and not by ion transport in the bulk solution. The limiting diffusion current  $j_{lim}$  governs the maximum current

allowed by diffusion for a single kind of ions and can be calculated via Fick's law [33]:

$$j_{lim} = nFD_{ion} \frac{c^0}{\delta_N} \quad (6.1)$$

where  $n$  is the amount of substance,  $F$  the Faradayic constant,  $D_{ion}$  the diffusion constant of a specimen,  $c^0$  the bulk solution concentration of the specimen and  $\delta_N$  the diffusion layer thickness.

This equation shows that with increasing diffusion distance the maximum current is decreasing, resulting in smaller process windows for high quality electroplating. This diffusion limitation also means that a plating bath designed for LIGA fabrication uses higher concentrations than regular electroplating baths of both metal and conducting salt [55]. This creates a stronger diffusion gradient and therefore enhances metal transport from the bulk solution to the cathode surface.

For an estimation about which factor is most affected by temperature changes, the diffusion distance is assumed to be constant with a thickness corresponding to the resist height. The only factor influenced by temperature would then be the diffusion coefficient  $D$  of the gold-sulfite complex. With its value measured to be  $1.75 \times 10^{-5} \frac{\text{cm}^2}{\text{s}}$  at  $55^\circ\text{C}$ , limiting diffusion current is calculated to be  $8 \frac{\text{mA}}{\text{cm}^2}$  [15]. However, as no temperature dependence is found in literature, Stokes-Einstein behavior is assumed [21]:

$$D = \frac{k_B T}{6\pi\eta R_0} \quad (6.2)$$

with  $k_B$  as Boltzmann constant,  $\eta$  the viscosity of the fluid and  $R_0$  the Stokes radius of the ion. With the simplification that the hydrodynamic radius does not change with temperature, the limiting diffusion current at room temperature is approximately 10% less than at  $50^\circ\text{C}$ . On the other hand, it is assumed that exchange current density doubles for a temperature increase of  $10^\circ\text{C}$  [14]. This means that a temperature reduction of  $30^\circ\text{C}$  should lead to an eight-fold decrease in reaction rate.

Monitoring the influence of agitation on thick microstructure samples is a fast test, whether transport or reaction inhibition govern low temperature gold electroplating. For the usual bath agitation in a magnetic stirrer, periodic signals in the cell voltage<sup>3</sup> with a frequency of some Hz (i.e. rotation frequency of the stirrer) are expected if transport limitation prevails [33]. When existent, it can be assumed that diffusion limitation is present as in this case minor flow disturbances cause a notable increase or decrease in cell voltage. This is surprising to a certain degree as limiting diffusion current is far less affected by temperature than anode or cathode reactions. It is further concluded that the diffusion layer thickness is equal to or larger than the resist thickness, as otherwise no agitation effects should be visible. If on the other hand no such influences would be seen, a reaction rate limitation is more likely. For the current gold electroplating bath operating at elevated temperature those periodic fluctuations can be observed, even if not microstructured samples are electroplated. This leads to the conclusion that at least one of the measures necessary should increase diffusive transport. Although equation 6.1 is only a rough approximation, it includes a way to overcome the negative effects implied by a temperature reduction. Whilst diffusion layer thickness  $\delta_N$  is governed by the resist height (and therefore fixed), gold ion concentration can be increased as a compensation for the reduced diffusive transport.

## 6.3 Low temperature gold sulfite plating bath for flat specimen

### 6.3.1 Approach for low temperature electroplating

As was shown in the previous section, temperature plays a major role in all crucial electroplating sub processes, so changing it also means that a new working parameter set is needed. But in the worst-case, an entirely new

---

<sup>3</sup> For electroplating, cell voltage corresponds to the voltage difference between anode (Pt mesh) and cathode (substrate) that can be measured outside of the beaker

bath setup will be needed. As even extensive parameter studies are easier and faster to perform than the development of an entirely new bath formulation, the starting point of the work is a thorough parameter analysis based on the existing standard gold electroplating bath introduced in section 6.1. Due to the change in chemical surrounding when going to HAR microstructure plating, a two-step approach is used to find the optimum bath composition. For a first evaluation, flat specimen and coarse microstructures are electroplated to refine the bath formulation. When a point is reached where the electroplating results for coarse microstructures are stable and promising, the focus will then be put on refining the parameters for the production of high AR gratings. In this way, a set of working parameters shall be deducted.

The parameters tested in this study are:

- Current density
- Pulsed electrodeposition
- Bath agitation
- Pulse length
- Pulse duty cycle
- Immersion time prior to electroplating
- Electroplating area
- Gold shortage in the bath due to gold consumption

Temperature is for most experiments controlled to  $30 \pm 1$  °C, as this is deemed to be the highest operating point where no temperature driven mechanical deformations should emerge. If temperatures below 30 °C are desired, a cooling system would be needed to make the bath robust against room temperature fluctuations.

The resulting deposits are characterized according to their optical surface, which is the easiest and most feasible evaluation criterion. It can be used

as a test, because the accessible information from optical inspection also correlates with the desired result features for microstructure electroplating. Flat, smooth and shiny plating areas are considered optimum surfaces because they are an indicator for little surface roughness as well as sufficient micro and macro throwing power.

The optical test consists of inspecting the sample regarding to: surface structuring, brightness, over- or dendritic- growth of the electroplating layers and delamination. Also, strong height variations across the electroplating can be detected by eye.

All those observations are gathered in seven different criteria, where for each sample only the appearance or the total absence of that specific criterion is noted. The parameters tested for are summarized in appendix A.1, together with their respective impact factor for quality assessment. All of these criteria can appear separately on the samples and usually are repeatable for a given parameter set. The samples quality is then evaluated by weighting each criterion for its impact on electroplating performance and summing up the criteria to gain a score representing the optically accessible surface quality.

### **6.3.2 Electroplating bath setup**

All electroplating experiments are performed with a standard beaker approach [15]. Smaller test baths usually consist of 200 mL of electrolyte, whereas the baths for grating fabrication are prepared in 3 L beakers containing 2 L of electrolyte. The beakers are placed on heatable magnetic stirrers to regulate agitation and temperature ( $\pm 1$  °C) of the bath. Temperatures tested for the low temperature electroplating approach are 25 °C to 40 °C, with a strong focus on 30 °C, as this seems to be an upper threshold where no mechanical deformations can be expected.

A four-quadrant power source (Keithley Source Meter 2601A) allows the application of both voltage- and current controlled pulses as well as pulse

sequences. Additionally, cell current or voltage can be measured simultaneously. Pulsed electrodeposition is introduced to enhance grain refinement, which should lead to more uniform microstructures [37].

A compilation of some of the bath compositions made during the parameter study can be seen in table 6.2. They are all based on a slightly modified standard electroplating bath as described in section 6.1. Bath composition itself was changed with varying contents of gold, Na-EDTA and ethylenediamine. Additionally, additives like Bi and Cu were added in some bath variations to act as catalysts, brighteners or for grain refinement [79].

Bath name	Bath volume	Gold content	additional $\text{Na}_2(\text{SO}_3)$	EDTA	Additives
AU_140808_AA	2L	25 $\frac{\text{g}}{\text{L}}$	30 $\frac{\text{g}}{\text{L}}$	30 $\frac{\text{g}}{\text{L}}$	Bi,Cu
AU_040711_A-G	1.4L	25 $\frac{\text{g}}{\text{L}}$	30 $\frac{\text{g}}{\text{L}}$ to 50 $\frac{\text{g}}{\text{L}}$	30 $\frac{\text{g}}{\text{L}}$ to 81 $\frac{\text{g}}{\text{L}}$	none
AU_050711_A	1.4L	25 $\frac{\text{g}}{\text{L}}$	50 $\frac{\text{g}}{\text{L}}$	81 $\frac{\text{g}}{\text{L}}$	Bi,Cu
AU_270812_A	0.2L	35 $\frac{\text{g}}{\text{L}}$	100 $\frac{\text{g}}{\text{L}}$	60 $\frac{\text{g}}{\text{L}}$	none
AU_110912_A	1.3L	35 $\frac{\text{g}}{\text{L}}$	180 $\frac{\text{g}}{\text{L}}$	120 $\frac{\text{g}}{\text{L}}$	none
<b>AU_100713_A</b>	2L	35 $\frac{\text{g}}{\text{L}}$	180 $\frac{\text{g}}{\text{L}}$	120 $\frac{\text{g}}{\text{L}}$	none

Table 6.2: Major electroplating bath formulations of this thesis. Ethylenediamine content ( $22 \frac{\text{ml}}{\text{L}}$ ) has not been changed in those major bath versions and is therefore not noted there. The bold marked bath is the favored bath formulation.

### 6.3.3 Additives in the gold sodium sulfite plating bath

As is known from various electroplating systems, additives can play a substantial role in tailoring the bath towards the desired plating results [70]. To test if those are beneficial for low temperature electroplating,  $\text{Bi}_3^+$  is added to the bath as it was shown that Bi can enhance gold electrodeposition from sulfite based electrolytes [78]. Bismuth ions as an additive can accelerate gold deposition at the cathode by depolarizing inhibiting species [43].

The findings of these test depositions are not conclusive as no systematic benefit could be achieved. For the low temperature, low gold content bath a

slight but not significant improvement of optical quality and micro-throwing power can be detected. However, the high gold content bath formulations show good working conditions even without Bi content, so the additive is left out for the studies of this work. As deposition times in low temperature plating are rather low, Bi addition might again be looked into to check for a significant reaction rate increase, if faster plating is of a concern.

### 6.3.4 Substrate materials for electroplating experiments

To investigate the performance of the electrolyte when going to lower temperatures, the first test substrates are brass Hull cells sheets [40]. For a defined electroplating area, they are electrically sealed by rubber tape ("green tape") to create open plating areas of  $1\text{ cm}^2$  to  $5\text{ cm}^2$ .

The best parameters found for the Hull cell plates are transferred to unpatterned  $\text{TiO}_{2-x}$  substrates [19]. The titania coated wafers are also used as substrates for UV- and x-ray lithography (see section 4.2.1). They are chosen because their rough surface area allows for optimum resist adhesion to the substrate. Furthermore, titanium is not affected by the electroplating solution, therefore no pre-treatment is necessary. And despite being composed mainly of titania, enough metallic titanium is present to achieve a sufficiently conductive surface. One drawback is the CTE mismatch of Si/Ti and most of the x-ray and UV resists. While silicon has a CTE of 2.6 ppm/K, most polymers are in a region of 30 ppm/K to 100 ppm/K. In case of temperature variation, this leads to significant tensions (mostly in the resist) which dramatically increases the risk of delamination.

Patterning of these wafers is executed as described in sections 4.2.2 and 4.4.1. For flat specimen electroplating, a single square opening of  $1\text{ cm}^2$  is patterned into mr-X resist to reduce one tolerance factor <sup>4</sup> for these experi-

---

<sup>4</sup> As the openings of the brass sheets are defined by rubber tape, their shape is not always exactly rectangular and a precise calculation of the electroplating surface sometimes not possible

ments. The mask for this layout is printed with a standard inkjet printer onto acetate sheets coated with a gelatin.

### 6.3.5 Enhanced starting growth via higher current densities

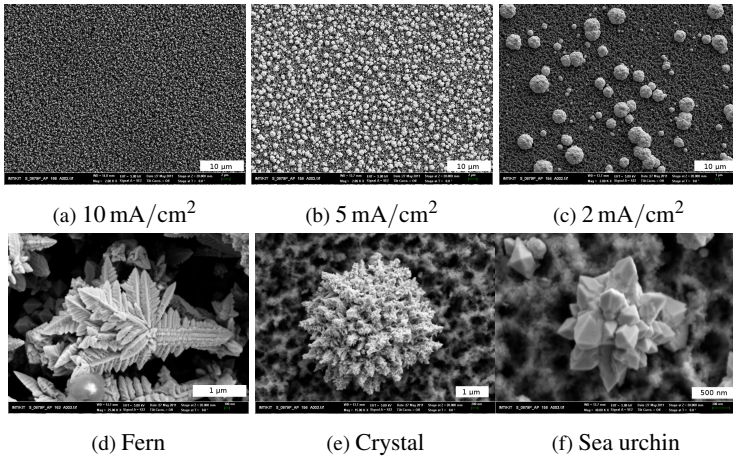


Figure 6.3: Various Gold Shapes that are created in the low temperature electroplating bath by varying current density, temperature or pulsed plating are shown.

One of the first observations going from Hull-Cell plates to  $\text{TiO}_x$  substrates is a clearly inferior starting behavior, which means a non-homogeneous coverage of the plated area. Starting growth is irregular, unpredictable and generally unstable, giving almost random results. Using the standard starting treatment for the electroplating of x-ray gratings, which consists of 3 min at elevated voltage does give better results but still shows instabilities. Therefore, a small test series is conducted to see if the biggest influence factor for electroplating - current density- also has an impact on starting behavior. Within this test range also temperature, agitation, pulsed and non-pulsed deposition and pulse length are changed to investigate their importance for good starting growth. All test samples share a common total charge density

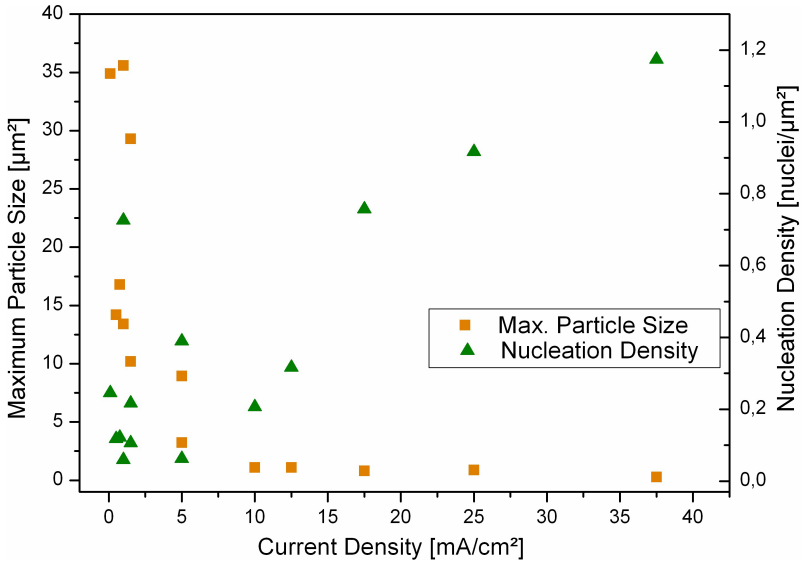


Figure 6.4: Gold particle size and nucleation density in dependence on the most influential parameter- current density, leading to dense grids of small particles at higher current densities

of  $200 \text{ mC/cm}^2$ , which corresponds to a homogeneous gold electroplating layer of 200 nm thickness. Out of the adjusted parameters, only current density has a significant impact on the starting behavior of the low temperature bath.

The improvement comes from the drastic reduction of particle sizes with increasing current density whilst creating a dense and uniform pattern (see figures 6.3a, 6.3b and 6.3c). High current density leads to an increase in the number of nucleation sites, and, even more importantly, to an equalized growth of the particles.

To evaluate the number of nucleation sites, SEM pictures of electroplated surfaces are taken and analyzed with a watershed filter for image processing and particle counting. The number and size of particles are then calculated

and plotted, as seen in fig. 6.4. It shows that when exceeding a threshold of  $10 \text{ mA/cm}^2$ , particle size and nucleation density clearly correlate. Above this threshold, only high numbers of small particles are created. In the regime below  $10 \text{ mA/cm}^2$ , both values are not as clearly linked and also depend on various other plating parameters, especially pulsed current.

So, in order to obtain homogeneous starting layers for grating fabrication, a starting current density of  $10 \text{ mA/cm}^2$  or above is proposed. As electroplating in thick resist layers is mainly limited by diffusion, a gold thickness of  $100 \mu\text{m}$  or above limits the average current density to  $1 \text{ mA/cm}^2$ . The limitation stems from hydrogen formation caused by the gold ion depletion of the diffusion layer, which has to be avoided as gas bubbles contained inside the resist structures will lead to voids in the metal parts. This limitation can be circumvented by applying short (smaller  $100 \text{ ms}$ ) pulses with high current densities but long off-times so that the mean current consumption is lower than  $1 \text{ mA/cm}^2$ .

An additional finding is that by changing plating parameters a wide array of gold particle shapes could be created. Each of them is representative for a specific parameter set and can be fabricated repeatedly. The shapes include spheres, cauliflowers, crystals, sea-urchins and fractals (see figures 6.3d, 6.3e and 6.3f). So, with one single bath a whole range of micro- or nanoscopic particles with vastly varying surface areas can be created which might for example be utilized in Surface Enhanced Raman Spectroscopy (SERS) [89] or as chemical sensors [39].

Regarding the low temperature electroplating, a standard set of parameters is found to reliably start the electroplating process with a highly homogeneous seed layer which is a crucial prerequisite for good electroplating results.

### 6.3.6 Observations for low temperature gold electroplating

When performing the parameter study of low temperature gold electroplating baths, a few general observations are made. As these are present in a sufficiently large number of samples, a few trends in low temperature electroplating can be seen:

- The bonding forces of the electroplated layer to the Hull Cell sheets can be an indirect tool for estimating the intrinsic stresses of the electroplating's layers. If they are too large, the samples start to detach from the brass sheet substrates. But when using Ti/TiO<sub>x</sub> coated wafers, not a single sample from more than 100 experiments shows any signs of detachment. This also demonstrates, that deformations in gratings are most probably not caused by metal delamination.
- The bathtub effect is an issue for some plating baths, but for most of the samples border overgrowth is not too strong and only limited to the boundary areas of the plating area and not to actual microstructure cavities. It is even further reduced in baths with higher gold concentrations.
- Small gold spheres are an indicator for insufficient leveling in the bath in combination with the current density being too high. This effect is among the first signs of a beginning dendritic growth when going to even higher currents. For baths with small macro throwing power, they also appear when electroplating microstructures. Typically, it is coupled with the growth of small gold spheres along the border of the conductive area. In this case, the chosen parameter set is unsuited for electroplating.
- Terraces (clearly differentiated heights with very steep ramps in between) in the gold surface are a specific problem of some bath variants. Typically, terrace levels exhibit different appearances, e.g. the

lower terraces (less gold height) having a rougher appearance and the top terrace showing a smooth gold surface. This effect is strongly correlated with bath agitation. The stronger the agitation, the more likely is the formation of those terraces. This phenomenon sets an upper limit to stronger bath agitation for enhanced diffusive transport by increasing the gold concentration close to the surface.

- Brilliance of the gold plating area is not of highest importance, as excellent (meaning nanometer sized roughness) micro throwing power is among the lesser factors for electroplating HAR structures. Nevertheless, a golden color is tried to achieve as it corresponds to a surface roughness in the sub  $\mu\text{m}$  scale. Brown finishes in contrast have a roughness exceeding  $10\ \mu\text{m}$ . In some unadapted baths, smooth and brilliant samples also show quite deep notches which sometimes have a flushed-out like appearance. It is assumed that those are places where the current flow is initially perturbed and an error zone starts to grow.

### 6.3.7 Stability of the electroplating bath and bath aging

All electroplating baths (and at the end of bath lifetime also the electroformed structures) suffer from bath aging. This effect comes into play when more and more metal has been leached out of the bath either by electroplating or also through precipitation. During the development of the low temperature gold bath, gold precipitation has been optically monitored. Some bath formulations show excessive precipitation which rules them out from further evaluation. For the standard plating bath, a gold leach of  $2.5\ \frac{\text{g}}{\text{L}}$  through electroplating is considered acceptable during its operation. If the gold loss exceeds this amount, additional gold sodium sulfite solution is added to the bath to retain the original gold concentration of  $25\ \frac{\text{g}}{\text{L}}$ .

Gold precipitation in contrast can lead to an increase in  $\text{SO}_4^{2-}$ , as elemental gold precipitate is formed by the oxidization of  $\text{SO}_3^{2-}$  on air and the

simultaneous reduction of  $\text{Au}^+$  to elemental Au. As  $\text{Na}_2\text{SO}_4$  has a much lower solubility than  $\text{Na}_2\text{SO}_3$ , saturation and therefore precipitation in the bath can be reached much faster. If small transparent needles from  $\text{Na}_2\text{SO}_4$  precipitates are observed in the bath, it typically is considered as no longer suitable for reprocessing.

The standard electroplating bath is quite resistant to bath aging and has typically to be redone after  $10 \frac{\text{g}}{\text{L}}$  of Au is extracted from the bath (including Au refilling). So, for any of the new bath formulations attention is paid to sudden, but lasting changes in electroplating results, increased gold precipitation or in the worst-case needle like crystallites in the bath.

### 6.3.8 Parameter study on brass and Titania substrates

To identify important parameters during a wide spread parameter study, one way of retaining process windows is to look for distinct clusters of good samples in the n-dimensional parameter space with little or no bad samples in the same region. This is found, amongst others, in the combination of plots for Au, EDTA and  $\text{Na}_2\text{SO}_3$  concentrations. For illustration purposes, the combination of Au, EDTA and  $\text{Na}_2\text{SO}_3$  concentration (x and y axis) in combination with sample quality (color) is plotted in three separate graphs (see fig: 6.5). Sample quality is color coded, going from red (bad) to green (good sample). The quality is assigned from the quality parameters defined in section 6.3.1. Two of these graphs show distinct areas with strong populations of good samples. Favorable combinations can be found for both high concentrations of sulfite and gold in the bath. One important reason has been deduced in chap. 6.2, where it has been demonstrated that diffusion is among the most critical processes in HAR electroplating and it can be seen from equation 6.1 that when increasing the concentration by a factor of 1/3, transport current limit goes up also roughly 30%. This cannot balance the loss of transport current through temperature completely, therefore the other process parameters (especially current density) have to be adjusted

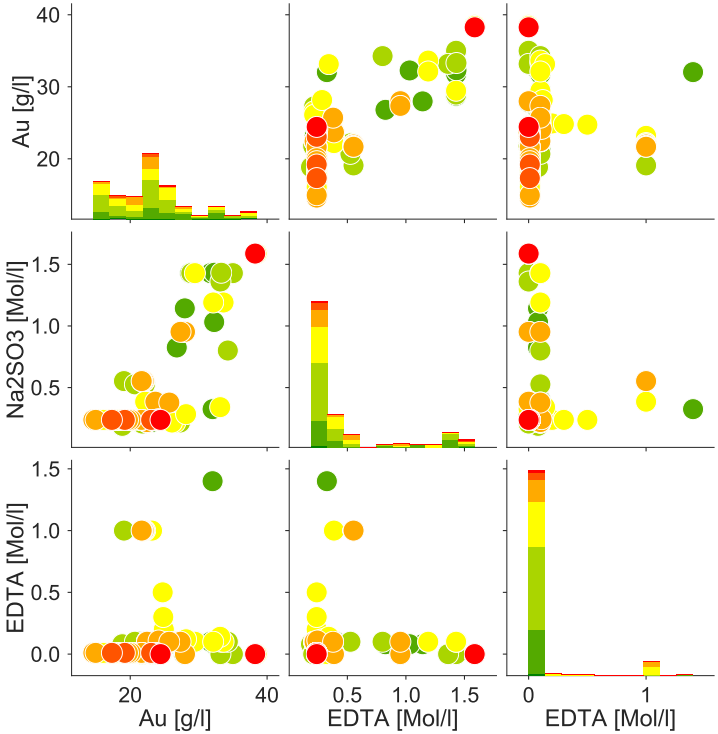


Figure 6.5: Scatterplot matrix of the bath concentration variation. Au, EDTA and Na<sub>2</sub>SO<sub>3</sub> contents are plotted against each other and dot color just like in fig. 6.6 represents the plating quality

accordingly. In fig. 6.5, one also sees that EDTA content does not play any significant role, as there are no distinct patterns of good samples.

Fig. 6.6 summarizes most parts of the parameter study to identify suitable electroplating conditions for all parameters investigated. In this graph, all parameters of this study are plotted against each other. The scatterplot matrix can nicely illustrate the span of parameters changed during the study and highlight the combinations with the strongest impact on plating quality. This is used to find a working parameter set.

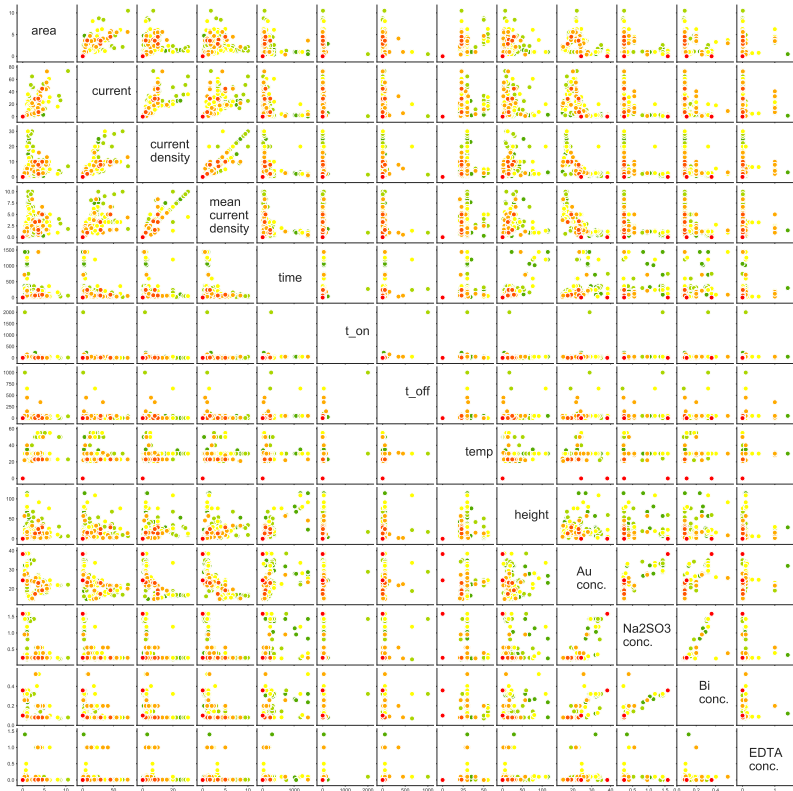


Figure 6.6: Scatterplot matrix of some of the varied parameters. The matrix displays the quality of the electroplating results (color coded from green=good to red=bad) in dependence on 2 parameters each. For a specific graph, the x and y axis are defined by the boxes written in the corresponding column and row. It gives a first overview of the parameter range used in this work. A more detailed analysis can be found in section 6.3.8.

So, after evaluating all the data gathered from the parameter study the following bath formulation and plating parameters have been gathered as a new standard for low temperature gold electroplating of high AR parts:

- Gold content is set to  $35 \frac{g}{L}$ . No stronger precipitation than in the standard plating bath could be observed

- EDTA content is set to  $120 \frac{\text{g}}{\text{L}}$ .
- $180 \frac{\text{g}}{\text{L}}$  of  $\text{Na}_2(\text{SO}_3)$  are added.
- No bismuth additive is used.
- Mean current density (excluding the starting phase) is  $0.35 \frac{\text{mA}}{\text{cm}^2}$  with pulse on and off times of 50 ms each

The stability of the electroplating bath against aging is not tested in particular, but the electroplating baths are continuously monitored concerning any kind of precipitation or sudden changes in electrodeposition results. For all baths, and the aforementioned bath setup in particular, it can be stated that they exhibit excellent aging resistance, working flawlessly even after long periods (>several month) of no use. Precipitation of elemental gold is low and can be further decreased if the beaker is sealed shut, for which already parafilm foil suffices. When going to higher gold, sulfite and EDTA concentrations, the baths become slightly more sensitive to bath volume decrease, showing sulfate precipitation after 10 % to 20 % of volume loss through evaporation. Whilst for the fabrication baths, volume changes are only in a 1 % to 5 % range, the investigated bath with their laboratory beaker handling are exceeding the aforementioned quota sometimes. If sulfate precipitation happens but the amount is very small (less than  $10 \frac{\text{g}}{\text{L}}$ ), the bath can be reused by filtering, as this also adds enough water to fall well below the solubility limit of  $\text{Na}_2\text{SO}_4$ . When those precautions are kept, the high concentration electroplating bath shows excellent aging stability and due to the highly increased  $\text{SO}_3^{-2}$  content also exhibits significantly less gold precipitation. No data has so far been gained on long term stability concerning gold replenishing, but first experiments demonstrate that the bath can also handle significant gold extraction (up to  $5 \frac{\text{g}}{\text{L}}$  without having a strong impact on the electroplating results).

To confirm the current efficiency of the gold plating baths, samples are weighted before and after plating. The results indicate 97 % to 100 % ef-

iciency, which corresponds nicely to reported values [15].

Overall, gold bath stability can be assured and only long-time bath operation is to be seen in future work.

## 6.4 Low temperature electroplating of UV- and x-ray samples

The aforementioned electroplating baths are continuously tested with microstructured samples to detect deviations in the electroplating of flat specimen and microstructured substrates at an early stage. Besides x-ray gratings also UV LIGA samples are used as these enable to fabricate moderate aspect ratios which should increase the impact of diffusion on the electroplating.

### 6.4.1 Layouts for UV-exposure

With the knowledge that the electroplating of flat, unstructured specimen exhibits different requirements on the electroplating bath than electroplated microstructures [66], an intermediate step between flat area and grating electrodeposition is needed. A design addressing this should include separated voids prohibiting stronger influences of agitation as the high aspect ratio (HAR) structures exclude any flow near the anode surface. This is mimicked by an inverted square pattern, cutting  $50\ \mu\text{m} \times 50\ \mu\text{m}$  sized holes into the resist in an  $80\ \mu\text{m} \times 80\ \mu\text{m}$  pitch. With a resist height of  $100\ \mu\text{m}$ , this gives  $50\ \mu\text{m} \times 50\ \mu\text{m} \times 100\ \mu\text{m}$  empty pillars in the resist mold distributed over an area of  $1\ \text{cm} \times 1\ \text{cm}$ . Having an aspect ratio (AR) of two in both dimensions perpendicular to the growth direction, the influence of convection is reduced significantly [13] and diffusive transport has to play a bigger role. Those structures are used to get a first knowledge about micro- and macro-throwing power as well as the starting and wetting<sup>5</sup> behavior of the new bath formulation and the suiting plating parameters.

---

<sup>5</sup> Wetting in this case is defined as the ease of manually inserting the structures into the bath without trapping air inside closed cavities which create voids during electroplating

To further increase the challenge for electroplating, for a few tests more complex finger shaped microstructures are used. Main focus is on the throwing power, as the layout contains both negative and positive tone sections. Those are helpful to determine height distributions across smaller and wider cavities as well as the growing behavior along resist borders as some bath setups produced strong tendencies towards border region overgrowth. Depending on the macro- and micro throwing power of the bath, this can include both the border of the patterned area as well as the interfaces of the patterning itself [20].

### 6.4.2 Electroplating of UV-Liga Parts

Most parameters that have resulted in moderate or good electroplating results from the parameter study are also tested with the aforementioned UV-LIGA structures. Temperature for all experiments is kept at  $30 \pm 1$  °C, as this set point has shown both reasonable plating results as well as little or no thermally induced defects. Typically pulse height is in the range of  $1 \frac{\text{mA}}{\text{cm}^2}$  to  $2.5 \frac{\text{mA}}{\text{cm}^2}$  with a symmetrical pulse duty cycle (ratio of on time to entire pulse period) of 0.5 and a pulse length of 50 ms. Current density is varied between  $0.1 \frac{\text{mA}}{\text{cm}^2}$  to  $50 \frac{\text{mA}}{\text{cm}^2}$ .

The pillar shaped microstructures can also be evaluated optically, as they allow for an easy assessment of height distribution both locally within one microstructure and macroscopically over the entire patterned area.

When electroplating microstructured specimen, none of the bath formulations with a gold concentration of  $25 \frac{\text{g}}{\text{L}}$  and working parameters which yield smooth surfaces for unstructured specimen did give proper microstructures. The most common problem of those deposits is bad micro throwing power, resulting in heavily fluctuating gold heights (see fig 6.7 a) and b)). The structures have a strong bathtub effect within the cavity as well as irregular height distributions across the sample. Those defects seem to be related to bath agitation, which again supports to the conclusion that a bath tempera-

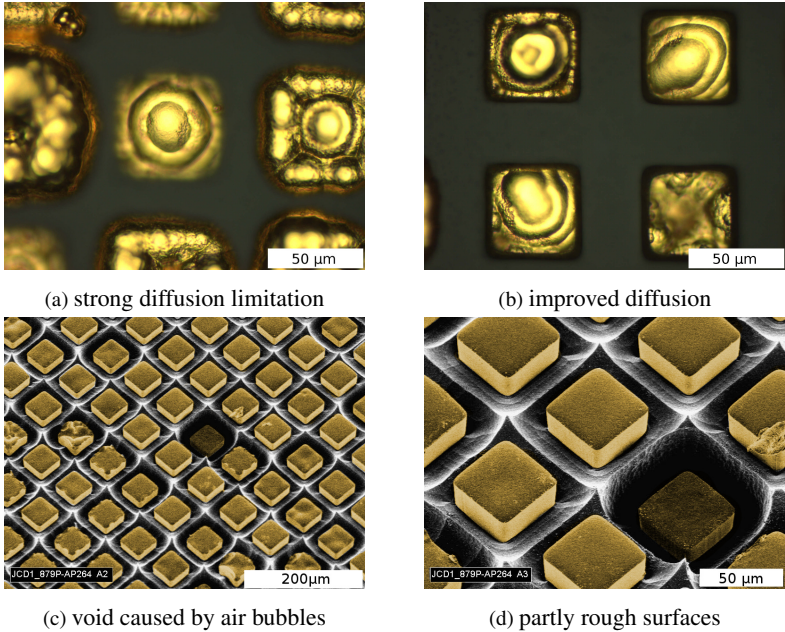


Figure 6.7: Electroplating result for the standard (upper row) and high Au concentration plating bath (lower row), showing the initial problems of the electroplating baths. Those have been bad micro throwing power due to diffusion limits and air incorporation because of insufficient wetting behavior.

ture of  $30^\circ$  means operating very close to the limiting diffusion current.

Going to a bath formulation with  $35 \frac{g}{L}$  of gold produces entirely different electroplating samples. Those are smooth in the micrometer scale, level across both the single cavity as well as the entire plating area and allow for reasonable plating speeds. But to achieve these level surfaces and to overcome the bathtub effect, also EDTA and  $Na_2SO_3$  content have to be raised significantly. Sample pretreatment with Isopropanol rinsing is performed to minimize air entrapment in the resist features.

The resulting structures are void free and show perfect height distribution over the entire area of  $1 \text{ cm} \times 1 \text{ cm}$  (see fig 6.8). Furthermore, this bath for-

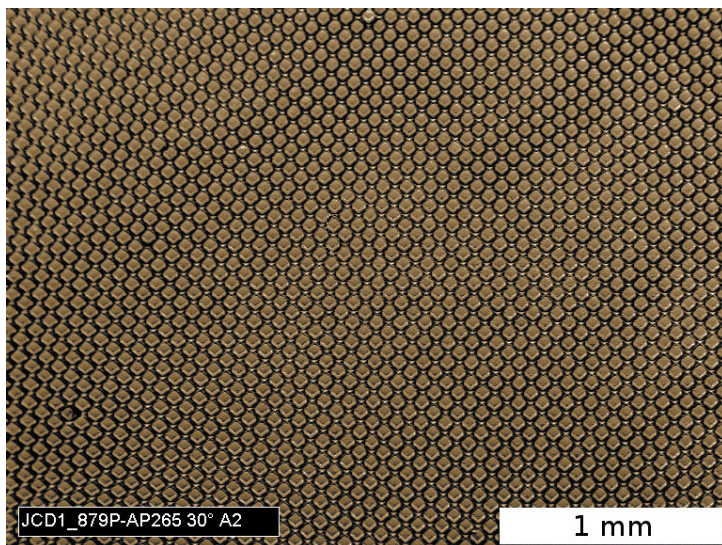


Figure 6.8: Electroplating samples showing no air cavities, good height distribution and surface smoothness, hinting for a good micro- and macro-throwing power

mulation also features a very limited bathtub effect, which can be seen both in fig. 6.8 as well as in the figures 6.9b and 6.9a. Especially of note is picture 6.9b, where the field of view covers the edges of two  $2\text{ mm} \times 1\text{ mm}$  plating areas, which usually would have shown significant bath tub effect if the macro throwing power is not sufficient.

### 6.4.3 Electrochemical Cell Monitoring

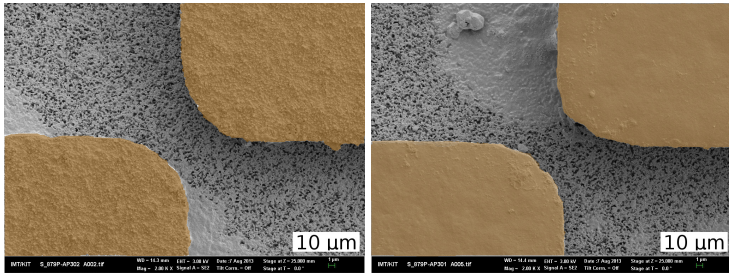
When comparing cell voltage with the samples appearance, it is found that a number of effects during electroplating are detectable via the long-term cell voltage monitoring. The measured voltage is a sum of the potential difference of both electrodes as well as ohmic resistance and impedance of the electrolyte. With the assumption that the counter electrode reaction does not change over time, one can gain certain information about charge trans-

port and the reactions at the anode. Whilst this approach cannot be used for a thorough and in-depth analysis of an electrochemical system, it can deliver certain information for well-known baths. Incidences like overgrowth, leveling, area mismatch and poor electroplating parameters all have corresponding trends in the monitored voltage. By constantly monitoring the bath and the outcome, those patterns can be allocated to the aforementioned phenomena. To make cell voltage a valuable tool, one has to record cell voltage and correlate its progression to the physical state of the sample.

To measure and record the cell voltages, two separate tools are used. For short time observations, especially for pulsed deposition, measurements of the voltage between cathode and anode via an oscilloscope are done, sampling one or a few pulse cycles. This gives information about the leveling state, pulse times and general plating condition via the voltages at the end of the current pulse ( $V_{\text{on}}$ ) and the end of the off-state ( $V_{\text{off}}$ ). Those measurements are repeated continuously throughout the experiment, especially if changes to the previous state are detected.

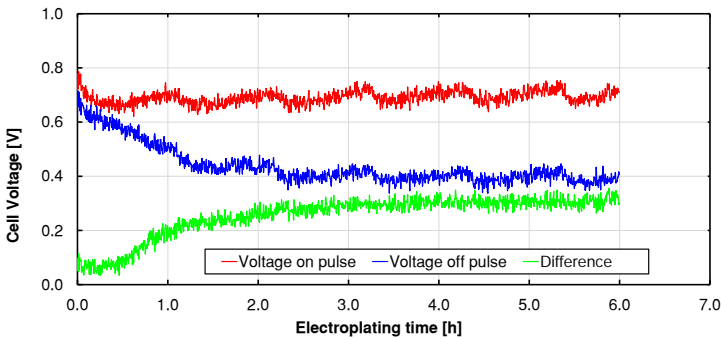
As a second information, cell voltage is measured at specific time intervals with the four-quadrant power sources. For this measurement, cell voltage at the end of the on and off pulses during the entire electroplating time is recorded, so that long term drifts can be detected. By recording cell voltages and pulse shapes, different states of electrodeposition can be characterized so that even without optical access to the electroplating result (which is important for the electroplating of small microstructures with high AR) one can gain some information about the current state of electrodeposition as well as the depositions chronological progress. This helps to analyze the course of electroplating in the hindsight.

One characteristic pattern, which is observed in all samples (see fig. 6.9c) is a periodic oscillation of  $V_{\text{on}}$  and  $V_{\text{off}}$  voltage with a periodicity of one hour or even more. This periodicity can be empirically linked to the temperature fluctuations in the electroplating bath. During operation, the heating and cooling is controlled by a heatable magnetic stirrer. This setup



(a) Rough state during leveling

(b) Smooth state



(c) Cell voltage record of a sample with leveling

Figure 6.9: Images a) and b) are SEM images taken before (a) and after (b) leveling. In the bottom graph the cell monitoring record for this microscopic leveling can be seen. It can be observed, that the leveling process has a very large time constant.

allows for temperature fluctuations of about  $\pm 1^\circ\text{C}$  (at  $30^\circ\text{C}$ ) which then correspond to voltage fluctuations of up to  $\pm 100\text{mV}$ . The extent differs, depending on the absolute bath temperature (with stronger fluctuations for higher temperatures) and the heating-up time prior to electroplating. If the bath is heated up right before the actual electroplating, the fluctuations are stronger than for a bath that has been running for a longer period of time. Cell voltages of  $0.7\text{V}$  at the end of the on pulses are found, which is typical for electroplating parameter sets with good results on flat or coarsely structured samples. For those samples where cell voltage is significantly lower

or higher than 0.7 V, the throwing power decreases significantly. It has been found empirically that bath operation outside a corridor of  $700 \pm 150$  mV will result in insufficient micro- and macro-throwing power. So, cell voltage can act as a guideline to check if the electroplating is running well within its borders or if some specific problem arises. Thermal instabilities resulting in cell voltage fluctuations of  $\pm 100$  mV are already at the border of being acceptable. For low temperature electroplating, an even tighter temperature control might be advisable.

A number of samples also shows reasonable delayed leveling<sup>6</sup> effects during electroplating. This leveling effect is quite characteristic, as it usually takes between 15 min and 45 min to appear in the cell voltage and some additional minutes until it can also be seen optically (figures 6.9a and 6.9b). The effect emerges as a drop in the off-time voltage (see fig. 6.9c). The drop is quite significant with almost 400 mV in difference in  $V_{on}$  and  $V_{off}$  between the rough and the leveled state. This effect is not only visible in the cell voltage signal, the surface of the structures also changes noticeably when leveling. At the beginning, the gold surface is still rough and usually of brown color, which could be a heritage from the substrate, as its surface is highly fractal. After it has reached this steady state of leveling, the surface appears smooth and gold-colored. This can also be seen in figures 6.9a and 6.9b.

This effect can also be demonstrated for UV-micropatterned samples with high gold content baths, but not for grating structures, which points to a dependency on ion transport for this leveling effect. As also samples with gold in the voids can show delayed leveling (e.g. after inspection for structural conformity), the titania substrate can be excluded as a root cause. The long time span of 15 min to 30 min until it appears in the cell voltage signal is an indicator for an absorption driven process, as diffusion happens on much shorter timescales in this size regime. As anodic and cathodic processes are

---

<sup>6</sup> The effect is called leveling, as for the first samples, where this effect has been observed, a notable brightening of the sample has been observed. Brightness of those metalized samples is strongly correlated to surface roughness.

rather complex regarding the actual reaction steps [38], it is hard to deduct the actual inhibiting reaction steps of the leveling.

Typically, the aforementioned  $0.7 \pm 0.1$  V are the targeted cell voltage, but for microstructured samples, this value changes according to resist height. Finally, with this target value it is possible to detect large discrepancies in calculated and real plating area and allows to correct the plating parameters on line during electroplating.

As a conclusion, cell monitoring can give valuable information about the state of low temperature electroplating and can be used to tailor the plating parameters according to the given circumstances, circumventing the problem of insufficient inspection methods beforehand. For a further refined low temperature electroplating bath, the leveling effect should be studied in more detail to make it applicable for all structures.

#### **6.4.4 Low temperature electroplating process for grating fabrication**

Just like the transition from unstructured to coarsely structured samples, low temperature electroplating of gratings is expected to need some further adjustments. Main point is to overcome the strongly increased ion transport limitation. Another challenge are process fluctuations, which result (among others) in closed or partly closed openings ("skin effect") [18] or crosslinked resist that can be found both in the middle of the lamella void and at the bottom [45]. As this resist cannot be detected prior to electroplating, irregularities in electroplating are sometimes hard to distinguish from unavoidable lithographic process fluctuations. All in all, one has to keep in mind that the results have to be interpreted by partly guessing the origin of deviations being from lithography or electroplating.

All grating samples electroplated in the low gold content ( $25 \frac{\text{g}}{\text{L}}$ ) electroplating bath show the known features: they all have signs of diffusion limitation in the bath. Most characteristic are strong fluctuations in height, presumably

caused by positive feedback coupling of flow disturbances, initial height deviations and a concentration of the electric field on the highest parts of the metal microstructures. For some of these gratings height fluctuations of  $80\ \mu\text{m}$  with a total electroplating height of  $100\ \mu\text{m}$  are found, which cannot be attributed to the bathtub effect. So, the baths of these samples show bad throwing power both across the entire surface (typically in the cm range) as well as within a single lamella ( $\mu\text{m}$  range). All of these gratings also have in common that mean current density has to be lowered by approximately 10 % to 50 % in order to obtain samples with similar surface micro structure compared to UV structured specimen.

For the final high gold content ( $35\ \frac{\text{g}}{\text{L}}$ ) bath however, reasonable plating results are found. This parameter set applies the same plating conditions as are used for flat area samples and sub-mm and micrometer sized structures. This also helps for the electroplating of structures that include large open spaces<sup>7</sup>. Lower mean currents (and thus longer electroplating times) have to be used in comparison to the standard high temperature baths to achieve similar plating results. This can be explained with stronger diffusion limitation, so the mean current density has to be adjusted to a decreased ion transport rate. To demonstrate the excellent leveling ability of this new bath formulation seen in the UV lithography samples, a grating that is far from perfect is chosen for electroplating. This  $2.4\ \mu\text{m}$  period grating with a layout, where the bridges are statistically distributed has strong deviations of the lamella positions. A gold height of  $45\ \mu\text{m}$  is to be electroplated in  $70\ \mu\text{m}$  resist structures.

The cell voltage record yields an on-pulse voltage of  $0.7\ \text{V}$ , but no sign of the characteristic voltage drop. In a SEM inspection (see figures 6.10a and 6.10b) after partial resist etch it can be observed that the height distribution over the sample is well within the variation range of the standard LIGA

---

<sup>7</sup> Early grating designs (and other LIGA structures) have large areas surrounding the actual structured region to shield the structures from uneven current distributions, like they can be found in an electroplating beaker. The compensation structures act just like an aperture.

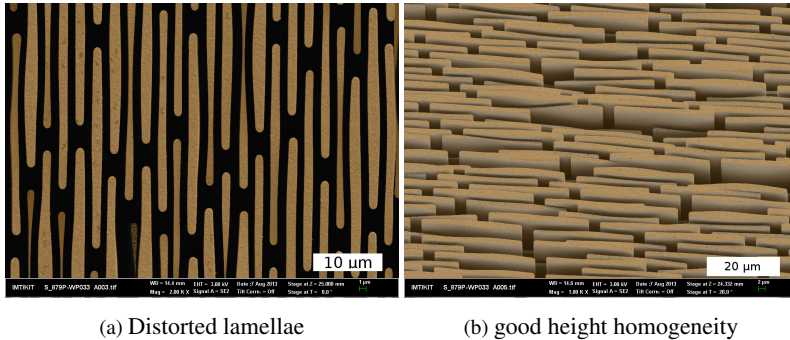


Figure 6.10: Distorted sample electroplated in a bath with high gold content. This bath formulation clearly has good throwing power as resist structures are highly irregularly formed and still level electroplating structures are formed. Deformation in resist has already been present beforehand, so no conclusion for stability improvements can be drawn.

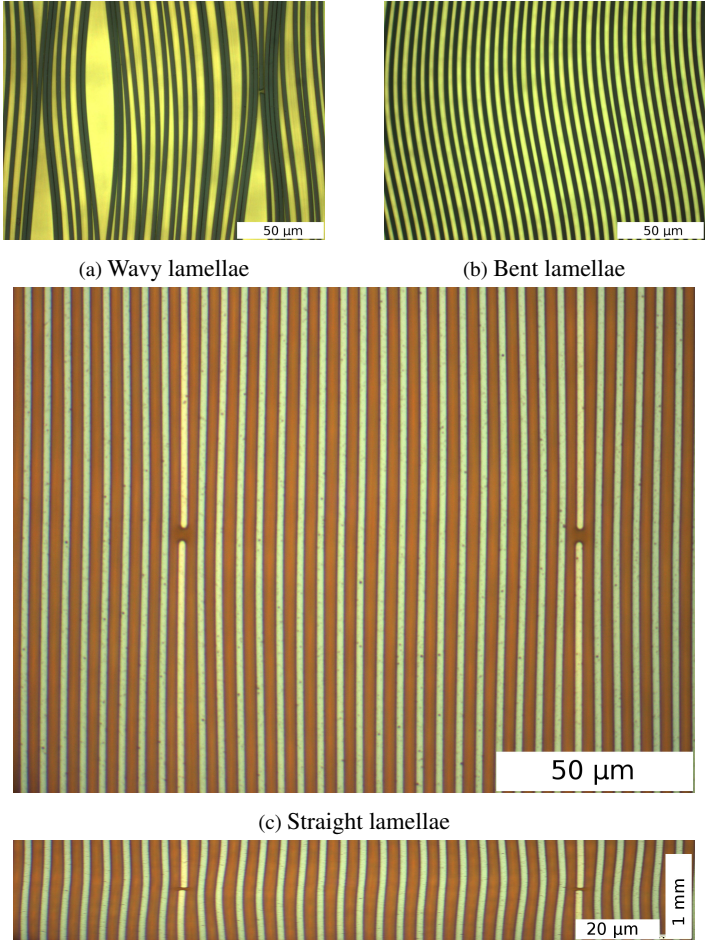
bath, showing a lamella to lamella deviation of about  $\pm 5 \mu\text{m}$  whilst having only little overgrowth along the borders. With regard to the electroplating performance of the final bath formulation it can be demonstrated that geometric variations in duty cycle and lamella width are not interfering with electroplating results, which makes the bath a good choice for microstructure electroplating. All of the low temperature baths with lower gold content however and to a certain extent also the standard electroplating bath have produced strong overgrowth along openings like trenches and the e-beam stitching areas.

After demonstrating that the new formulation produces very level surfaces even for non-uniform samples, the enhanced geometric conformity as a result of the new bath is highlighted. For these freeze-dried structures [58] [56] with a period of  $5.4 \mu\text{m}$  and a height of  $55 \mu\text{m}$  with continuous lamellae are electroplated. In combination with the standard plating bath those structures are bent or wavy after immersion and electroplating (see figures 6.11b and 6.11a). The deformation is a result of the CTE mismatch of substrate and resist and cannot be overcome by changing lithographic parameters (an

alternative solution is the use of CTE adjusted substrates, as demonstrated by Koch [47]). When electroplated in the low temperature bath, the freeze-dried sample has very little deviations except for the ends of the lamellae (see fig. 6.11d). These small deviations can be strongly overemphasized when shrinking the image 6.11c along the lamella direction, so that the microscope pictures have a width-to-height ratio of 10 or more (see fig. 6.11d; note the different scale bars for both directions). The distorted images reveal that there is still some waviness inside the lamellae, but in combination with the usual pixel sizes the deviations are negligible.

Overall, those gratings are so far the closest representation of a line and space structure produced with the LIGA technique. Low temperature electroplating allows the filling of highly unstable structures that will bend under very minor thermal loads. In the standard electroplating bath, those structures cannot be made (see figures 6.11a and 6.11b). But up to now the PEB after freeze drying does not allow to fabricate gratings with a height of more than 50  $\mu\text{m}$ . This reduces the number of possible applications as they can only be integrated into low energy x-ray setups.

To sum up, a gold electroplating bath working at 30 °C has been developed. For fast parameter screening large area samples and samples with small features has been used. It is demonstrated, that increasing gold and EDTA content is the key parameter to overcome temperature induced changes. The bath formulation has good structural conformity and excellent macro- and micro throwing power, which has been demonstrated on UV-structured samples.. With additional parameter adjustments this bath formulation also works for gratings fabrication. Tests on highly fragile structures show that this bath is the most promising option for a stress free electroplating process to fabricate high AR gratings.



(d) Rescaled low temperature grating to overemphasize distortions

Figure 6.11: Three typical examples of freeze-dried long continuous lamellae electroplated at elevated temperatures (a and b) and at 30° (c and d). Picture d) has been rescaled along the lamella direction to overemphasize the distortions still found

## **7 Low temperature gratings used in phase contrast imaging**

To demonstrate the high structural conformity of the low temperature gratings experiments at DPCI setups will be presented in the upcoming chapter. Where applicable, a comparison with simulations will be drawn.

### **7.1 Characterization of gratings at x-ray sources**

When the gratings are finished optical and microscope inspections can only give minor information about the quality of a fabricated grating (see also appendix A.3). To illustrate long-range deviations in geometry (in this case long range equals to distances larger than approximately 1 mm; this already covers up to 4000 periods) interferometric analysis is an ideal characterization method. The best tool to evaluate grating quality is to measure visibility and signal to noise ratio at x-ray facilities. For this kind of characterization, both synchrotron setups and conventional x-ray tubes are used. Those measurements at the x-ray facilities are of highest significance, as only by applying the gratings in a real setup, 3D deformations, grating imperfections and long-range aberrations can be measured and visualized. As grating interferometry heavily relies on long range conformity, this proves to be the only tool to measure or at least visualize those effects. One major drawback of this technique is that for grating characterization at least one or two almost ideal gratings are needed for detailed error analysis. Understanding effects in visibility maps from a combination of two or three deformed gratings is

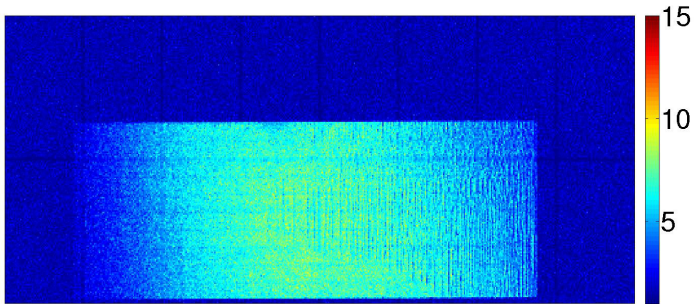
rather challenging as the 'symptoms' heavily superimpose each other. And because the beamlines and x-ray tubes are quite different in their setups, gratings are usually only comparable within one set of measurements. All of these setups are very prone to alignment changes, which makes comparisons difficult even between different measurement campaigns at the same facility.

## 7.2 Tools for grating quality evaluations

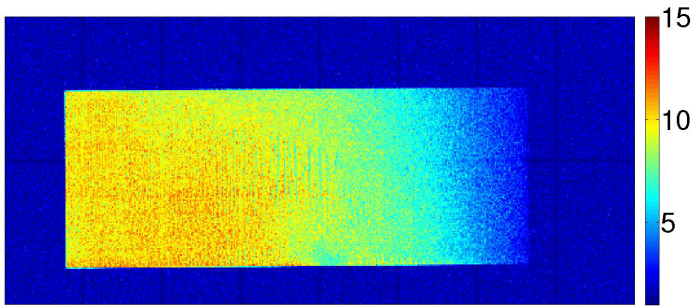
Visibility plots [22] of the grating area are the most widely used method to evaluate grating quality. However, one has to be aware that in the case of low photon flux the visibility can be putatively high <sup>1</sup>. Typically, those noise related artifacts only appear in the outer parts of an image, as flux for lab setups without biological samples can be easily adjusted and SNR increased. Therefore, these artifacts are cut away (by cropping the images) or suppressed to 0. In case of the analysis of dose limited biological samples, more time-consuming algorithms can be used to suppress noise related peaks. If not given by a color bar in the plot, visibility maps are color coded to a minimum and maximum visibility of 0 (blue) and 0.5 (red) respectively. Another quality criterion of gratings in a setup is the Signal-to-Noise Ratio of a setup, which is proportional to visibility and the square root of the flux (see equation 4.5). This factor also includes the transmission of the gratings, something which is usually not accounted for in grating characterization. So, especially gratings on thin substrates show significantly better flux but no improvements in visibility. If only visibility was used as a standard for grating quality, it would be ignored that gratings with higher SNR but lower visibility will yield overall better imaging performances unless illumination time or dose are not an issue. An example of an SNR map can be seen in image 7.1.

---

<sup>1</sup> If SNR is close to 1, noise can overlay the visibility signal significantly and noise peaks are counted as a maximum, arbitrarily increasing the visibility without physical significance



(a) SNR map of a regular bridged grating



(b) SNR map of a low temp. electroplated grating

Figure 7.1: SNR maps of a bridged (top) and a low temp. electroplated grating (bottom). For an SNR comparison, both were illuminated with the same exposure time of 1 s

The phase of a particular pixel is calculated as the crossing point of the sinusoidal intensity data with the mean value, which is shown in fig. 4.2. To measure the phase difference, the relative phase of a pixel in the object image is subtracted from a second phase measured without an object (also called flat field image). For a more robust signal, both negative and positive crossing of the stepping curve with the mean value<sup>2</sup> are evaluated separately to determine the phase difference between reference and sample.

<sup>2</sup> for a regular sine wave, this would be the points at  $\pi$  (negative) and  $2\pi$  (positive)

This improvement also removes some unwanted fringes in the phase contrast reconstruction images.

In some cases, the simulations from section 4.7 are used to understand unexpected visibility results. They are especially of use if a grating has deformations that are observable via the microscope. Examples would be deformed long continuous lamella gratings or contorted unit cell of gratings with bridges.

Their application is illustrated with the impact of strong gold height variations on the visibility. These variations have been in common for all low temperature grating samples electroplated in a 25  $\frac{g}{L}$  gold bath (section 6.1.2). For the simulations, a grating with a uniform height distribution equaling 50% of transmission through the gold lamellae is compared to a second grating with equal mean height, but a height spread of  $\pm 30\%$ . The simulated visibilities (see fig 7.2) show that for both gratings the mean visibility is within the same range<sup>3</sup>. What can furthermore be seen is that for decreasing binning size, the homogeneity of the visibility maps also decreases. But the effect is stronger for the perfect gratings, as more and more the gratings structure (in this case the bridges) creates superimposed signals in the visibility. For a lab environment, no significant impact on the imaging performance of the gratings is expected, as there is no visibility decrease and the additional noise can be compensated by longer acquisition times.

### 7.3 Measurements at the HAR-WI II beamline

With the simulation showing that height varied gratings are to operate similar to regular gratings, they are also tested at the HAR-WI II beamline at the DESY (*Deutsches Elektronen Synchrotron*) facility of the Helmholtz-Zentrum Geesthacht [6] to confirm the increased geometric conformity of

---

<sup>3</sup> The small visibility increase seen in the data (especially for small binning sizes) is presumably due to statistical variations generated by the gratings mean height value.

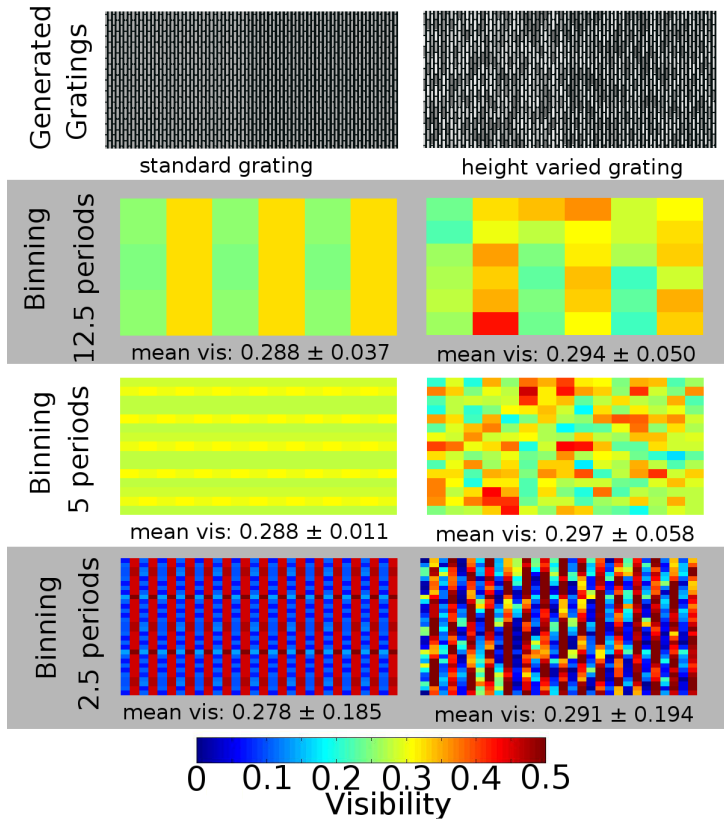


Figure 7.2: Simulated visibility maps (rows 2 to 4) for a bridged grating (left column) with a transmission of 50 % through the gold lamellae (gray) and a grating with strong height variations (right column) and a mean transmission of 50 %.

the low temperature bath electroplating. The beamline (including its three-grating set-up) has already been described by Herzen[34].

The height variation in the lamellae reaches up to 100 % of the gratings mean gold thickness of  $55 \mu\text{m}$ . G2 period is  $2.4 \mu\text{m}$  and the typical energy is 32 keV, but can be tuned in the range from 18 keV to 85 keV.

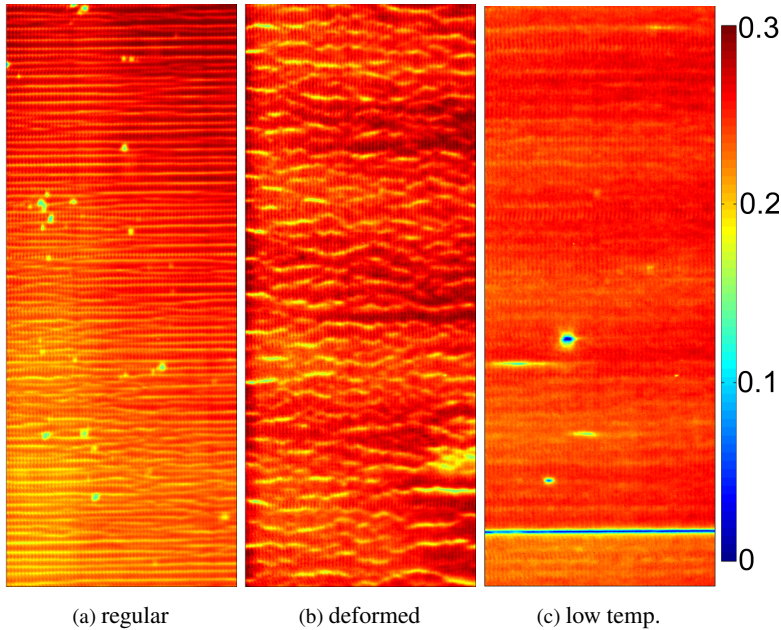


Figure 7.3: Visibility maps of three bridged gratings measured at the HARWI-II beamline at DESY. Left image is a regular grating ( $60\ \mu\text{m}$ ), the middle a distorted grating ( $75\ \mu\text{m}$ ) and the right a low temperature grating ( $55\ \mu\text{m}$ )

Fig. 7.3 shows the visibility maps of three bridged gratings (equal height:  $60\ \mu\text{m}$  to  $75\ \mu\text{m}$ ), where the right column depicts a low temperature grating, the middle a grating with many defects and the left column one with few observable flaws. Both gratings from the regular bath exhibit strong horizontal stripes in visibility. All gratings have superimposed vertical stripes, which are caused by the bridges of the gratings (can also be seen in fig. 7.2). The homogeneous appearance of the low temperature grating (c) is accredited to the absence of grating trenches and high structural conformity. So, even with strongly varying gold height, low temperature gold gratings can reach equal visibility.

## 7.4 Visibility measurements at the x-ray tube at TUM

### 7.4.1 X-ray tube setup at the TUM

As the fabrication of x-ray phase contrast gratings with a low temperature electroplating bath has been successfully demonstrated, the aim in the following section will be to show the impact of these gratings on the imaging performance.

Most grating visibility measurements are done at the A1 setup at the Lehrstuhl für Biomedizinische Physik of Prof. Pfeiffer from TUM [35][95][92]. The setup consists of three gratings with a period of  $5.4\ \mu\text{m}$  placed in a symmetrical arrangement in combination with a highly sensitive but low spatial resolution Dectris Pilatus detector (pixel size is  $170\ \mu\text{m}$ ). Additionally, it allows for a close to full area<sup>4</sup> visibility map, which is the main reason for choosing this setup for grating characterization.

When going to an x-ray tube setup, one more difficulty arises in comparison to typical synchrotron set-ups: due to the need for two absorption gratings (G0 and G2), two (possibly) distorted gratings are superimposed, which makes attributing error sources to a single grating a challenge. Distortions in the phase shifting gratings are not even factored in, although they are surely present as well (e.g. in the case of slight height variations in nickel).

### 7.4.2 Low temperature grating performance

To demonstrate the imaging performance of low temperature grating, they are tested at the setup against the best available gratings. So, the long continuous lamella gratings (see section 6.4.4) are measured at the x-ray tube at TUM and compared to both sunray and bridged gratings. Both grating types have higher gold fillings than the long continuous lamellas, but also employ more distortions from the reinforcement structures. The first test is

---

<sup>4</sup> maximum grating area was 5 cm x 5 cm in 2013

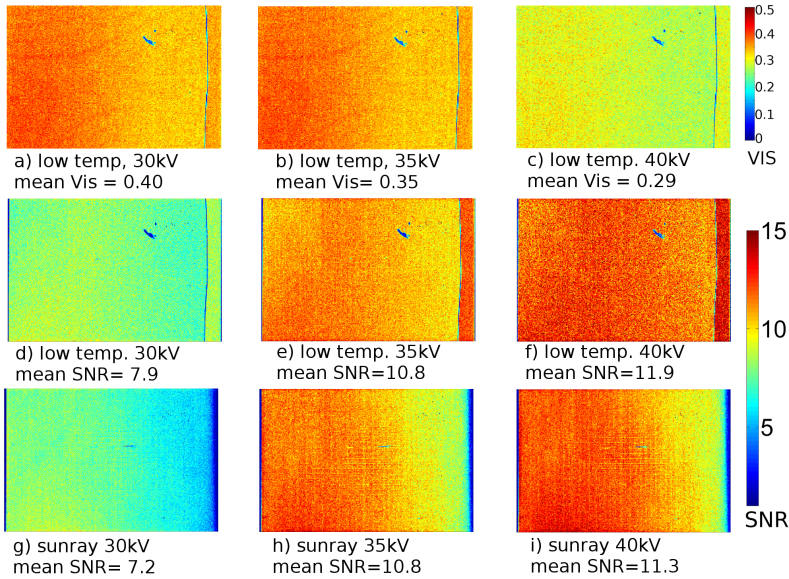


Figure 7.4: SNR map comparison for the long continuous lamella grating electroplated in a low temperature electroplating bath and a sunray grating. SNR values are for acceleration voltages of 30 kV, 35 kV and 40 kV from left to right. SNR increase from left to right for low temp is mainly due to flux increase. Exposure times are 3 s for each image.

a comparison against the best available grating up to date, an 80  $\mu\text{m}$  sunray grating. Visibility for both gratings in all images are in the range of 0.3 to 0.5. Both gratings have low absorbing 200  $\mu\text{m}$  silicon substrates, which increases their SNR significantly. The relative<sup>5</sup>SNR factor maps (see fig. 7.4) shows that the SNR of the low temperature grating for all acceleration voltages is equal to or higher than the best sunray grating. And this is despite the fact, that the long lamella grating has only half the height of the sunray gratings, which increases residual transmission through the gold from less than 1 % to 10 % at the design energy of 20 keV. The increase in SNR with

<sup>5</sup> Only flux and visibility are factored in for this SNR calculation. As illumination times is kept constant at 3 s for all grating measurements, those can be compared.

rising acceleration voltage can be explained by a compensation of the gratings visibility decrease at high voltages (due to its low height of  $45 \pm 5 \mu\text{m}$ ) with a strongly increased flux. The visibility for lower energies are among the best that have been reported so far for this energy range at laboratory x-ray sources (45 to 50)[7].

Consequently, all other gratings, especially the bridged gratings on standard  $550 \mu\text{m}$  wafer substrates (or even thicker versions) are outclassed, in some cases by a factor of 10 concerning the SNR. The fact that the long continuous lamella grating performs better than a sunray grating with the same substrate thickness and a thicker gold electroplating height can be explained by two different theories: It could be possible that sunray gratings have deviations below the surface that so far have not been detected. Or with a higher or lower duty cycle of the long lamella grating, the sensitivity of the setup changes in comparison to the sunray variant. This could also lead to a higher overall performance [90]. As these gratings are supposed to be used afterwards, resist removal is not possible. So, the duty cycle or geometric distortions cannot be measured via SEM and optical inspection is not precise enough. On the other hand, no defects or deformations in sunray gratings have been measured, therefore there is not enough data to support either of the two theories.

In summary, long continuous lamella gratings have shown, that for highest SNR enhanced geometric conformity can counter lower gold height of up to 50 %, which opens up an entirely new path for grating fabrication for low or medium x-ray energy setups.

## **7.5 Comparison of gratings from low temperature and regular electroplating bath**

After testing the low temperature bath on the most fragile grating structures to demonstrate its ability to produce highly conformal structures, it is also used on sunray grating structures. This will highlight the limits for fur-

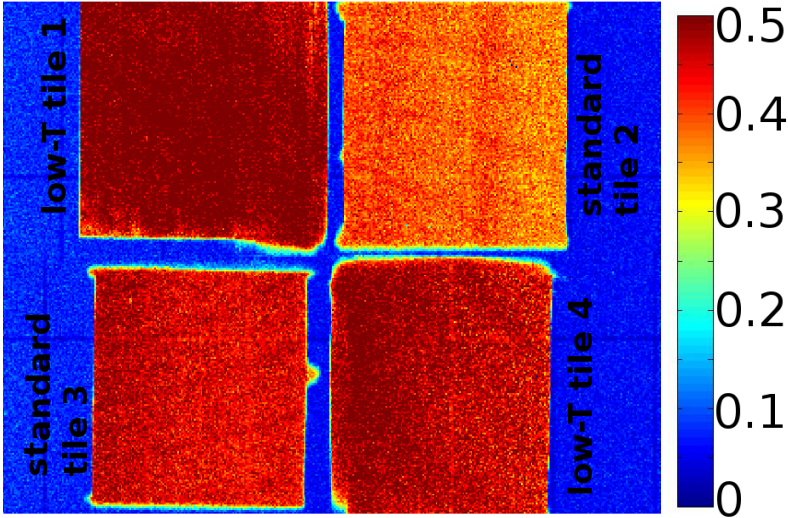


Figure 7.5: Visibility map for a grating cut in four tiles. Upper left and lower right grating tiles are processed with the low temperature electroplating, lower left and upper right gratings in the standard electroplating bath. Although aligned to give maximum visibility in tile 3, both low temperature bath tiles show higher visibilities.

ther improvement, as the mechanical stability of sunray gratings is already the highest for all grating layouts. To directly compare the impact of low temperature electroplating, a single, good looking sunray grating is cut into 4 separate pieces after development, which all have the same lithographic history. All grating tiles look homogeneous after development, so equal mechanical stability in the resist of all four sectors is assumed. After drying and inspection, two of those gratings are electroplated in the regular plating bath and the other two in a low temperature electroplating process. All four have an electroplating height of  $70\ \mu\text{m}$  to  $80\ \mu\text{m}$ , which at x-ray tube acceleration voltages of 30 kV to 40 kV equals full absorption.

To easily measure all four tiles, they are just pushed together, using a blank  $550\ \mu\text{m}$  wafer as a substrate. This not only makes the alignment of all four fields to each other less perfect [82], but also reduces SNR to an uncharac-

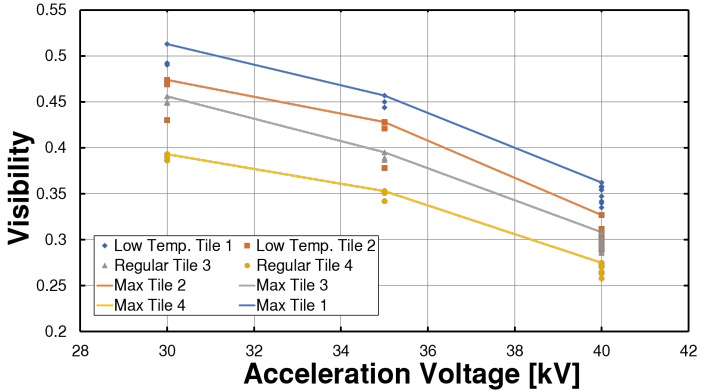


Figure 7.6: Mean visibility of the grating area and its max. value of all 4 fields of the wafer shown in fig. 7.5 for a set of different alignments. Each set of points is optimized for one of the 4 grating tiles whilst others have a small degree of misalignment.

teristically low value, therefore visibility is compared in this case. To compensate this alignment error in the visibility maps, the following procedure is used: one of the four tiles is aligned perfectly and all four fields are measured simultaneously by creating one visibility map. The corresponding visibilities for all four fields are calculated as the mean value of their respective areas. Once completed, the next of the four fields is aligned perfectly and again all are measured simultaneously. This is done for all four fields, which gives a set of maximum visibilities for all kinds of alignment. A visibility map of these gratings can be seen in fig. 7.5. Maximum visibility of all fields as well as the other visibility values for the wrongly aligned positions are plotted in fig. 7.6.

As can be seen, the low temperature electroplating bath (tiles 1 and 4) perform better than the regular plating bath (tiles 2 and 3). Whilst at 40 kV the deviations could be explained by small variations in height, at 30 kV transmission is so low that height differences can be dismissed while structural errors still have to be accounted. These measurements show that the

use of low temperature electroplating is also beneficial for samples that are already previously considered as mechanically stable. And again, it demonstrates the benefit of visibility mappings for grating characterization, as the small geometric deviations, that create the little differences in visibility between the samples with and without low temperature electroplating could not be observed by any other means.

## 7.6 X-ray imaging with low Temp. electroplating gratings

To illustrate the use of low temperature gratings for image acquisition, a set of tomographic reconstructions as well as some projection images have been taken. For all setups used in imaging, typically no difference can be seen between low temperature electroplating gratings and regular gratings.

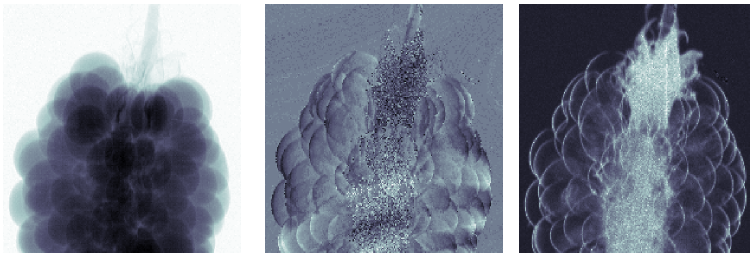


Figure 7.7: Absorption (left), differential phase (middle) and dark field image (right) of a blackberry taken in a setup using a low temperature grating as G2.

## 8 Summary and outlook

In the wake of this thesis, a gold electroplating bath has been developed that allows the metalization of highly fragile resist microstructures. Operating the bath at a temperature of 30 °C minimizes thermal stress in resist structures caused by temperature differences during the various LIGA process steps. As a prime example, this bath was used for the forming of absorption gratings which are employed in x-ray phase contrast imaging. When applying this electroplating method in combination with freeze drying during development, it has been possible for the first time to electroplate continuous lamella structures without any further reinforcement patterns. It could also be demonstrated that standard layout structures (bridged and sunray) for x-ray gratings can be fabricated more precisely, increasing their visibility performance in x-ray imaging setups and ultimately increasing signal-to-noise ratio.

The bath working temperature was chosen close to room temperature, as this operation point is deemed uncritical regarding the CTE mismatch of substrate and resist. To reduce the variable field a wide choice of process parameters (including current density, pulsing on and off times, bath composition, agitation and more) was scanned through by electroplating non-structured flat specimen, which were picked to speed up the process variation. As a result, it could be showed that current density as well as  $\text{Au}^-$  and EDTA content are the factors with the highest impact. The resulting bath formulation was used on microstructured samples and yielded mixed results. By refining the gold and EDTA content and decreasing the plating current density, a bath could be formulated that allows for the successful

fabrication of large area ( $50\ \mu\text{m} \times 50\ \mu\text{m}$ ) microstructures with aspect ratios smaller than two. These experiments demonstrated that for a bath working at  $30\ ^\circ\text{C}$  the most important factor is diffusion limitation, which is getting even more challenging in high aspect ratio grating structures. This diffusion limitation could be overcome by reducing the mean current density (but using pulsed current for increased working currents) and most importantly by increasing gold (from  $25\ \frac{\text{g}}{\text{L}}$  to  $35\ \frac{\text{g}}{\text{L}}$ ) and EDTA content of the electroplating bath. In a bath with  $35\ \frac{\text{g}}{\text{L}}$  of gold, grating structures could be fabricated that showed no deformation as well as good electroplating performance regarding micro-throwing power, bathtub effect and void free operation.

With this bath it was possible for the first time to electroplate defect free continuous lamella gratings with aspect ratios larger than 15. These gratings are not stabilized by any supporting structures and therefore represent the closest approximation of a perfect grating. For higher aspect ratios, freeze drying, necessary to develop the structures, or post exposure bake already generate large geometric deviations, which currently limits the wider introduction of these gratings.

But also a better understanding of the resist behavior along the full process chain including exposure, post bake, development and electroforming can help to circumvent these limitations. Previously most effort has been put into the lithography and patterning activities at the IMT, to such a scale that ultimately the limits of a well-established electroplating process were reached. In this work, a number of influencing factors were looked into by mechanical characterization to find the best lever for higher conformity in the final electroplated structures.

When examining the fracture surfaces of pull tests performed with tensile specimen made of mr-X, it could be proven that a horizontal decrease of crosslinkage in the material leads to softer resist close to the titania coated substrate and a harder region at the top of the resist. The gradient allows grating structures to deform slightly to decrease stress levels, similar to a soft die attach. This could also be demonstrated by the pull tests, which

showed a big spread in results due to inhomogeneous lithography along the beam axis. Especially when increasing temperature to 60°, all samples undergo plastic deformation. At room temperature in contrast, only one half of the samples had plastic deformation regions, all others showed brittle behavior. The spread of mechanical behavior vanishes, if lithography is performed at *Litho 2*, which leads to the conclusion that top-to-bottom ratio might be linked with the material properties. With dynamic scanning calorimetry, it was furthermore possible to prove that standard resist processing leaves uncrosslinked material in the bulk of the polymer, which then is not able to reach its highest possible strength. By using simulations, it could also be shown that temperature differences in the various processes are the most likely candidate for grating deformation. On the other hand, water uptake of the resist could be ruled out as a prominent factor for structural deviation in the gratings. At last, it was shown directly in the phase contrast imaging process that temperature (induced by radiation) can deform resist structures. Depending on the amount of deformation, this could, even when filled with gold, alter the geometry to the point where they are no longer usable for imaging.

This increased knowledge about the material has to be put to use in case of a future mass fabrication of gratings for commercial medical imaging setups. With regard to the gratings durability, they have to be tailored to withstand prolonged exposure to radiation. This will increase the need for gratings with minimal internal stresses, which could be accomplished by using low CTE mismatch substrates like polyimide in combination with low temperature electroplating. Ideally the resist polymer should be removed completely after electroplating, as its degradation has been proven to decrease imaging performance. The long continuous lamella gratings can be an interesting starting point for future grating layouts, as grating structure stabilization in imaging operation can be reached with metal reinforcement structures instead of polymer bridges or supporting structures. In this case, substrates like titanium or graphite are again the material of choice, as they have a bet-

ter CTE match to gold than polymer substrate foils. And due to lower CTE induced warpage and lamella deformation, low temperature electroplating allows to use thinner substrates, which can reduce dose in the application. The enhanced performance of low temperature electroplated gratings was shown in various imaging setups. Their imaging capability is on par or better than the best currently available gratings electroplated in the regular bath. Especially the long continuous lamella gratings outperform all other known gratings layout concerning the SNR, as they allow for both high visibility as well as high photon flux. So, despite their current height limitation of less than 50  $\mu\text{m}$  they can already be used in low energy x-ray imaging with photon energies of 25 keV. But even for putative sturdy structures like the sunray layout, improvements in SNR and visibility could be made with low temperature electroplating.

When highest SNR is of importance, e.g. in medical imaging, low temperature electroplating of gratings can enhance the performance of the interferometric set-up also in the case of structures stabilized with resist. Only when highest SNR is not an issue, for example in material characterization where illumination times can be increased to enhance the signal, the drawback of low temperature plating (twofold increase in plating time) has to be also taken into account when choosing the fabrication technique.

Due to their favorable SNR, it can therefore be concluded that low temperature continuous lamella gratings are ready for the implementation into imaging setups. For future grating developments, increasing the structural conformance even further could be an alternative path to increasing grating height, as even the best-known layouts still show room for improvement of both flux and visibility. Concerning a possible mass fabrication of gratings for future medical x-ray imaging instruments, the reduction of mean current density also points to the one big disadvantage of this bath formulation, which is the prolonged electroplating time. The bath improves yield due to the reduction of thermally induced deformations, but the output has to be increased by additional measures. These could include a further decrease of

pulse times to partially overcome localized diffusion limitations or the use of advanced flow control along the channels for enhanced ion transport.



# A Appendix

## A.1 Performance criterion table

<b>Criterion</b>	golden color	brilliance	no bath tub effect	no blotchy surface	no terraces	no spherical (over-)growth	no notches	substrate adhesion
<b>Impact Factor</b>	5	2	6	2	4	2	4	10

Table A.1: Table of the quality parameter for flat specimen and the parameters impact factor which is used to quantify the quality of a sample

## A.2 Duty cycle correction

Five years of x-ray grating fabrication has shown that creating gratings with a duty cycle in the final grating that matches the desired value (which is usually 0.5) often seems to involve random variations not necessarily depending on processing parameters. So especially for gratings with periods less than  $10\mu\text{m}$  the error in desired and actual duty cycle is increasing rapidly. In order to investigate the duty cycle behavior, a test layout is created, covering a total of 9 periods ranging from  $2.4\mu\text{m}$  to  $10\mu\text{m}$ . Each of the periods itself consists of 16 separate writing fields that have a predefined deviation from lamella width, where DC varies between 0.4 and 0.6. By first writ-

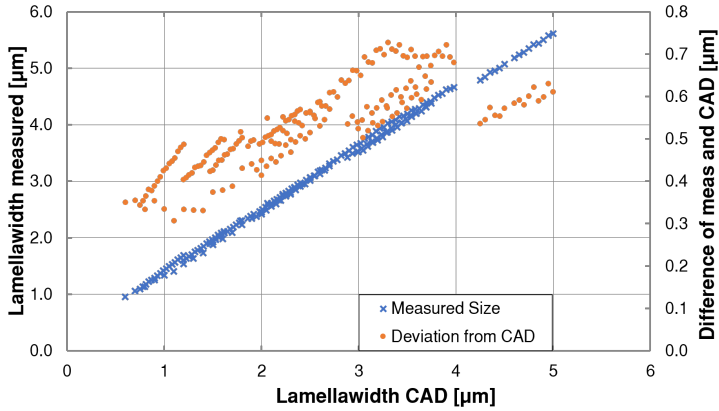


Figure A.1: Comparison of the difference of linewidth of grating structures with their originally designed CAD linewidth

ing and analyzing the lamella linewidth of this small grating sections on the mask created by e-beam lithography and later on characterizing the final structures made with either an intermediate or working mask, one is able to follow the DC along the process chain of intermediate mask fabrication (e-beam), working mask fabrication (LIGA) and grating fabrication (LIGA). After all relevant fabrication steps, SEM pictures of the separate fields are taken in three magnifications and the resulting pictures are analyzed using automatic image processing which yields duty cycle and linewidth of each field.

Data from the test layout shows an almost linear correlation between final grating structure size and CAD dimensions (see A.1). This finally makes it possible to pinpoint the exact dimension for the CAD layout to create a matching duty cycle for the intermediate mask. So as an example, to obtain a duty cycle of 0.5 in the final grating structures with a period of  $2.4\ \mu\text{m}$  (which equals a linewidth of  $1.2\ \mu\text{m}$ ), the intermediate mask has to have a linewidth of  $1.5\ \mu\text{m}$ . However, as a dependence of the DC on grating height is experienced, the problem still remains that for specific heights a bias of

the e-beam linewidth would have to be included. So, with one single mask only a small range in resist height can be fabricated with a matching duty cycle.

### A.3 Interferometric investigation of grating period and grating errors

An alternative method for the local detection a gratings duty cycle is evaluated. This method uses the interferometric reflection pattern of a grating that appears when a laser shines on the gratings surface. The pattern consists of a series of spots with equal angular distance. Those are all arranged in a line perpendicular to the grating lamellae, as those spots are the Fourier space representation of a grating with infinitely long lamellae without any bridges or intersections. Whilst the angular spacing is proportional to the gratings period, the intensity of the interference spots is defined by the gratings duty cycle. So, the intensity function of a single slit acts as an envelope for the gratings interference pattern. By measuring the intensity of the gratings interference spots and fitting a single slit envelope function

$$I(\varphi) \propto \text{sinc}^2 \left( \frac{D * \sin(\varphi)}{\lambda} \right) \quad (\text{A.1})$$

it would be possible to determine the Duty Cycle of a grating, as the period is assumed to be well known and could also be calculated from interference spot angular spacing. Whilst this technique does work for the gratings initially tested (grating period  $5.4 \mu\text{m}$ , it can be calculated that for the smallest gratings with a period of  $2.4 \mu\text{m}$ , the number of interference spots is too small to get a reasonably good fit. For a red laser, perpendicular incidence and a  $2.4 \mu\text{m}$  grating, only 4 orders of interference are visible, which then are fed into a fit function, that has at least one point of (virtual) total extinction within the angular range of those 4 points. With these specifications, no proper fit is possible and therefor also no DC measurement.

As the technique was supposed to be suitable for all gratings, a different approach is searched to test basic mechanical characteristics of the resist material. But the effort was not useless, as it turned out that the interference pattern is highly sensitive to the rotational angle of the grating and can be used for grating orientation when stitching.

## **A.4 Starting growth behavior in nickel electroplating**

As starting behavior proves to be crucial for the electroplating of thick gold layers, also nickel electroforming for phase gratings is investigated to see if it can also be improved there. Main concern in nickel electroplating has been the bath tub effect and a non-constant growth of nickel during the first phase of the electroplating, making a precise height control of those structures nearly impossible with the existing setup. But height control for nickel is an essential part of grating fabrication, as the phase shift is directly correlated to nickel height which implies that the deviation should not be larger than 5%.

To see any influences during the initial state of electroplating, again cell voltage is monitored. The results (see fig. A.2) show that the nickel electroplating process when using a standard nickel-sulfamate bath consists of 3 distinct phases with two clearly separated plateau phases. After a steep initial rise and a short drop afterwards, a plateau follows for 10 min up to 1 h. Afterwards, voltage increases about 100 mV within 15 min and then keeps that level until the end of electroplating. When correlating the data for the height deviation of the gratings produced with the length of plateau 1, it becomes evident, that both effects are correlated. Examining gratings whose electroplating has been stopped during plateau 1 phase show very little nickel coverage, less than what could have been expected for this amount of charge. SEM images also reveal that nickel coverage of the surface is correlated with an increase in cell voltage. When assuming a reduced current

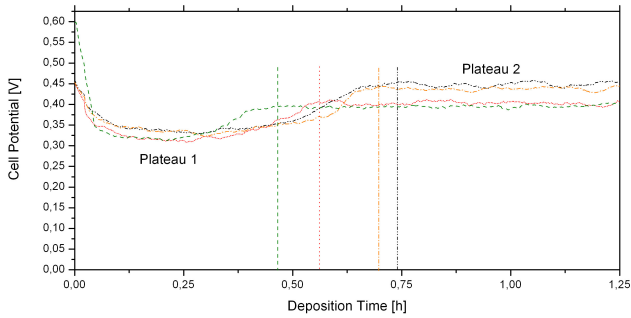


Figure A.2: Cell voltage monitoring for nickel electroplating showing three distinct sections. The length of plateau 1 coincides with the difference in nickel height

efficiency during plateau 1 and 100 % current efficiency during plateau 2 the nickel height can be fitted perfectly. It is therefore concluded that competitive processes at the  $\text{Ti}/\text{TiO}_x$  cathode are responsible for the current density loss. So, when cell voltage is monitored and the electroplating time adapted to the length of plateau 1, nickel height can be adjusted significantly better than without monitoring (see fig. A.3). The residual uncertainty is in the range of other possible error sources like small variations in duty cycle or overall electroplating area which cannot be controlled without extensive measures.

## A.5 Integrated Anodes for more homogeneous current distributions

It is well known that for electrodeposition current distribution and its contribution on growth rate is one of the key limiting factors. For a typical microstructure deposition, bath and sample geometry create the *bathtub effect*, a macroscopic height distribution over the entire microstructured area

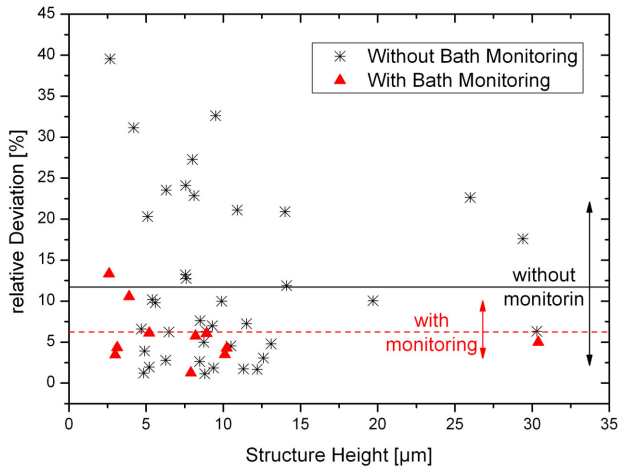


Figure A.3: Height deviation of nickel gratings with and without cell voltage monitoring, showing that adapting on the plateau 1 phase allows for more precise height control

where the border regions are 20 to 100 % higher than the region in the middle of the patterned area [45]. So, in the worst case, either 50 % of the resist height cannot be used for large parts of the mold or significant parts of the microstructure are overgrown. The effect highly depends on the electrolyte and the plating parameters, but can never be avoided when the usual plating cell geometries are used. In the case of the conventional gold-sulfite electrolyte applied to fabricate x-ray gratings, a height difference of  $20\ \mu\text{m}$  for  $100\ \mu\text{m}$  structures is experienced.

In order to use the entire mold height, a different approach is proposed, where the anode is integrated into the mold structure by fabricating it right on top of the mold and using the same pattern as the final microstructures. This concept can only be applied for resist structures that are shaped like

a closed mesh, as otherwise not all parts of the anode can be electrically connected. It works best for highly symmetric structures with small features and no large openings, such as x-ray gratings with a layout containing bridges.

This concept has some distinct advantages over the regular electroplating setup. The first is the most important one as well:

- + The Integrated Anode prohibits overgrowth of metal above the resist surface as immediately after reaching the surface an electrical short circuit is created, neglecting any further electrodeposition at this site.
- + Current density is concentrating only locally within the single lamellae of the mold and not over the entire electroplated area of the wafer. This removes any unwanted macro-throwing power of the bath (including the bath tub effect)
- + As current distribution reaches uniformity shortly below the channels' top, electroplating works like using excellently tailored apertures.
- + Depending on the conductivity and micro-throwing power, it is also possible that other lamellae can grow to the top even if the first has already reached the surface. This would make it possible to use the entire resist height for a metal filling
- On the negative side, sample preparation becomes increasingly laborious and needs very careful sample inspection
- Small grating errors can already stop this technique from being used on a regular scale

In order to demonstrate the capability of the Integrated Anode method to provide more homogeneous and advantageous current densities compared to the usual beaker setup, simulations of the current density for a simple electrical model are made. The simulations are done in Comsol Multiphysics 4.2a,

using only the electrical currents module. For simplification, all boundary effects and reaction inhibitions on both electrodes are neglected and the current distribution only depends on setup geometry and the conductivity of the electrolyte and the materials used.

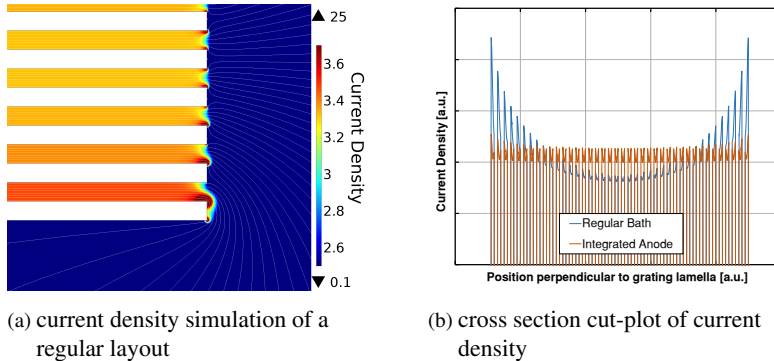


Figure A.4: The left image displays the simulated primary current distribution for a regular bath geometry. Grating bars are shown in white. In the regions close to the gratings border there is increased current density due to geometric shading. The right graph represents a linear section perpendicular to the grating lamellae 0.1 % of lamella height below the resists top surface. Additionally, the current distribution for an integrated anode layout is shown to highlight the current density leveling.

As can be seen in fig. A.4b, the current density in the case of integrated anodes is very homogeneously distributed across the grating surface, whereas the regular setup shows an increase along the outer sections of the structured area. The magnitude of this effect gets more pronounced for larger electroplating areas, so strong boundary overgrowth has to be expected. This means, when going to larger surfaces the integrated anode technique can yield significant bonuses for the electroplating by avoiding large scale boundary overgrowth. Also, if gratings are supposed to be stitched together [59], boundary overgrowth should be kept minimal, which would again be addressed by the integrated anode.

The production of samples with an integrated anode contains one crucial step, which is the fabrication of a conductive layer on top of the molded

resist. Direct patterning by the LIGA process would be possible, but as the LIGA technique is a highly time-consuming and costly process double exposures are to be avoided if possible. Patterning by UV on the other side is prohibited by the sputtered metal (gold) layer. To obtain the desired patterned conductive layer, gold is sputter deposited onto the final, already patterned, mold structures within a commercial sputter machine. If unmodified, the sputtered gold particles hit the substrate due to the chambers geometry under a wide range of angles, thus also covering the sidewalls of the mold, which short-circuits the  $\text{TiO}_{2-x}$  layer and the integrated anode. To remove or avoid this sidewall coating, there are two possible ways.

The first way is to sputter deposit gold on a tilted sample so that gold can no longer penetrate into the channels. This is only applicable for structures with high aspect ratios and, what is even more important, fails entirely if the sample contains holes with aspect ratios of 1 or less. This also includes mask defects. On those hole sites, gold sidewall coating will still appear and create massive short circuiting.

To circumvent these limitations, one can also combine a perpendicular sputtering step with a subsequent gold etching step. To etch the metalized sample a gold etching solution consisting of 4 g potassiumiodide, 1g iodine and 100 ml deionized water is used. The gold thickness on the sidewalls is mainly influenced by geometrically shielding 50 % of the sputtered particles as well as a prolongation of the sputtered surface, due to projecting the angular particle flux onto a nearly parallel surface, leaving highly increased surface areas for the same amount of gold particle flux per angle. This significant drop in thickness can then be used to free the entire sidewalls from gold while leaving enough of it on top to maintain sufficient conductivity. To further increase the anodes conductivity, it can be electroplated after the etching, which increases the anodes thickness. When the desired gold height is reached, Integrated Anode and cathode can be wired reversely (i.e. wired as usual) to start the electroforming of the microstructures. If desired, the gold coated surface on top can be removed by a second etching step after the

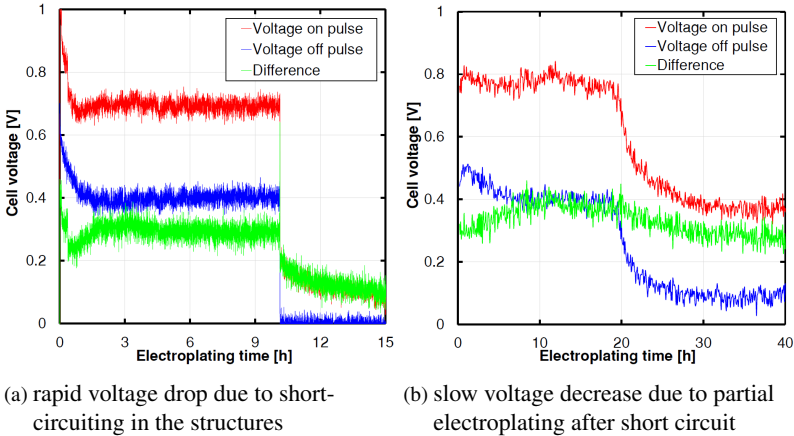


Figure A.5: Cell voltages of Integrated Anode tests showing short circuit (a) or aftergrowth (b)

end of microstructure electroplating. As the gold gratings are usually higher than 20  $\mu\text{m}$  no significant amount of gold inside the mold structures would be removed by this step. To detect a possible coating of the grating sidewalls by gold sputtering, prior to electroplating a measurement of the ohmic resistance between top and bottom electrode is done. For small resist heights and no etching, a resistance in the range of a few  $\text{M}\Omega$  can be found. This shows that a small gold covering along the sidewall exists which will lead to a short-circuit during electroplating within minutes. If no conductance can be measured with a standard multimeter, there is already enough separation between anode and cathode and the sample can be electroplated. During electroplating, also cell voltage is recorded. From this data, the exact gold filling can be extracted as well as the breakdown behavior. For the first samples with a non-perfect electroplating solution, sudden voltage drops down to 0 V shortly after start are common. This is due to the insufficient throwing power of the early baths, leading to strong local overgrowth and finally to a large area short-circuit. With enhanced throwing power in the later electro-

plating baths, the overgrowth can be decreased drastically, which enabled the growth of large area structuring to the top electrode. As growth rates are still not 100 % equal (due to stirring, structure height, starting behavior), some of the structures are already electrically connected whereas in others there is still electrodeposition until also there the anode is reached. This can be seen in fig. A.5 where there is no sharp voltage drop due to a large scale short circuit but instead more and more single gold lamellae reach the top electrode, leading to a steady decrease in cell voltage.

But when performing several electrodeposition experiments, it becomes obvious that the initial claim that the integrated anode makes it possible to grow metal structures up to the very top of the resist cannot be confirmed. Whilst early experiments are lacking a bath with suitable macro-throwing power, later experiments show that also baths with medium to good macro throwing power are not be able to complete electroplating until the top surface. This is presumably being caused by inhomogeneities in resist processing (as well as substrate bumpiness) with a non-uniform height distribution over the wafer, which creates local flaws in the electrical potential. Those are enhanced by the close distance between anode and cathode and lead to variations in gold growth that are too large, so that the desired effect cannot come about.

But the second effect, which eliminates a long-term problem for microstructure electroplating can be confirmed. With the adoption of the Integrated Anode technique, overgrowth can no longer occur. In the entire sample set with an integrated anode, not one showed any signs of overgrowth in any particular area, although all had deposition times that by far would have overgrown the entire area. So, for all of them the short circuiting works to stop electroplating.

Concerning the fabrication technique, no conclusive results can be made of the etched samples. It is demonstrated that small leak currents between anode and cathode after the sputtering (resulting in a resistance of a few  $M\Omega$ ) can be eliminated, breaking the leakage paths and therefor insulating anode

and cathode. But afterwards, no regular plating can be resumed, as usually short circuiting occurs within an hour. It is assumed that the etching time window is too narrow to erase all sidewall gold fillings but still leave intact top anode structures. Additionally, problems might also be created when filling the trenches with the etching solution, as trapped air bubbles in combination with short etching times will lead to great differences in absolute etching depth.

For samples with HAR on the other hand, inclined sputtering could be demonstrated to work flawlessly, as long as the structures have no significant trenches or holes inside the structured area. Samples with such a sputtering layer can be grown almost to the top (typically reaching medium heights in the range of what is feasible in regular electroplating for the same resist height. One example for such a grating structure can be seen in fig. 7.5, where the lower right tile has been fabricated using the Integrated Anode technique. The entire grating area (about  $2\text{ cm} \times 2\text{ cm}$ ) could be electroplated to a height of  $80\text{ }\mu\text{m}$ . As all 4 gratings are supposed to share the same height, electroplating is stopped at that height without trying to reach the top surface.

In conclusion, it is shown that the Integrated Anode technique is a tool to overcome both bathtub effect as well as structural overgrowth. Both are problems that are frequently experienced in grating fabrication due to process tolerances. But statistics also show that the yield is far from optimum, with approx. 20 % to 30 % of the samples actually being fully electroplated. So, the outcome of the experiments is, that instead of decreasing the dependence of electroplating on the previous fabrication steps (which mainly influences partial overgrowth), it increases the dependence even further. It might be a tool to obtain optimal electroplating results, but only after close sample inspection and greatly increased preparation time for electroplating. Whilst for grating "mass" fabrication the process is regarded as too fragile, for critical single samples where overgrowth is to be avoided at all costs it can be a valuable tool in electroplating.

# Bibliography

- [1] ALS-NIELSEN, Jens ; MCMORROW, Des: *Elements of modern X-ray physics*. second. John Wiley & Sons, 2011. <http://dx.doi.org/978-0-470-97395-0>. <http://dx.doi.org/978-0-470-97395-0>
- [2] ALTAPOVA, V. ; BUTZER, J. ; ROLO, T.d.S. ; VAGOVIC, P. ; CECILIA, A. ; MOOSMANN, J. ; KENNTNER, J. ; MOHR, J. ; PELLICCIA, D. ; PICHUGIN, V.F. ; BAUMBACH, T.: X-ray phase-contrast radiography using a filtered white beam with a grating interferometer. In: *Nuclear Instruments and Methods in Physics Research Section A: Accelerators, Spectrometers, Detectors and Associated Equipment* 648 (2011), S. S42–S45. <http://dx.doi.org/10.1016/j.nima.2010.12.218>. – DOI 10.1016/j.nima.2010.12.218. – ISSN 01689002
- [3] BARD, Allen J. ; FAULKNER, Larry R.: *Electrochemical Methods: Fundamentals and Applications*. New York : John Wiley & Sons, 2000. – ISBN 0471043729
- [4] BECH, Martin ; JENSEN, Torben H. ; FEIDENHANS'L, Robert ; BUNK, Oliver ; DAVID, Christian ; PFEIFFER, Franz: Soft-tissue phase-contrast tomography with an x-ray tube source. In: *Physics in Medicine and Biology* 54 (2009), Nr. 9, S. 2747–2753. <http://dx.doi.org/10.1088/0031-9155/54/9/010>. – DOI 10.1088/0031-9155/54/9/010. – ISSN 00319155
- [5] BECKER, E. W. ; EHRFELD, W. ; HAGMANN, P. ; MANER, A. ; MÜNCHMEYER, D.: Fabrication of microstructures with high

- aspect ratios and great structural heights by synchrotron radiation lithography, galvanofforming, and plastic moulding (LIGA process). In: *Microelectronic Engineering* 4 (1986), may, Nr. 1, S. 35–56. [http://dx.doi.org/10.1016/0167-9317\(86\)90004-3](http://dx.doi.org/10.1016/0167-9317(86)90004-3). – DOI 10.1016/0167-9317(86)90004-3. – ISSN 01679317
- [6] BECKMANN, Felix ; LIPPMANN, Thomas ; METGE, Joachim ; DOSE, Thomas ; TISCHER, Markus ; LISS, Klaus D. ; SCHREYER, Andreas: HARWI-II , The New High-Energy Beamline for Materials Science at HASYLAB / DESY. In: *AIP Conference Proceedings* 705, 2004. – ISBN 0735401802, S. 392–395
- [7] BIRNBACHER, Lorenz ; WILLNER, Marian ; VELROYEN, Astrid ; MARSCHNER, Mathias ; HIPPE, Alexander ; MEISER, Jan ; KOCH, Frieder ; SCHRÖTER, Tobias ; KUNKA, Danays ; MOHR, Jürgen ; PFEIFFER, Franz ; HERZEN, Julia: Experimental Realisation of High-sensitivity Laboratory X-ray Grating-based Phase-contrast Computed Tomography. In: *Scientific reports* 6 (2016), Nr. October 2015, S. 24022. <http://dx.doi.org/10.1038/srep24022>. – DOI 10.1038/srep24022. – ISSN 2045-2322
- [8] BÖGER, Thorsten ; DILGER, Klaus ; SCHMÖLGER, Gerhard: FE-Simulation der Klebstoffschwindung während des Aushärtvorgangs. In: *Adhäsion Kleben und Dichten* 10 (2001), Nr. 01
- [9] BOWDEN, P. B. ; HAWARD, Robert N. (Hrsg.) ; YOUNG, R. J. (Hrsg.): *The physics of glassy polymers*. 2. ed. London : Chapman & Hall, 1997. – ISBN 0-412-62460-5
- [10] BRAVIN, Alberto ; COAN, Paola ; SUORTTI, Pekka: X-ray phase-contrast imaging: from pre-clinical applications towards clinics. In: *Physics in Medicine and Biology* 58 (2013), S. 1–35. <http://dx.doi.org/10.1088/0031-9155/58/1/R1>. – DOI 10.1088/0031-9155/58/1/R1

- [11] CALLISTER, William D. J. ; RETHWISCH, David G.: *Materials Science and Engineering: An Introduction*. 7th. John Wiley & Sons, Inc., 2007. – 975 S. – ISBN 9780471736967
- [12] CAMPO, A. del ; GREINER, C.: SU-8: a photoresist for high-aspect-ratio and 3D submicron lithography. In: *Journal of Micromechanics and Microengineering* 17 (2007), Nr. 6, S. R81. <http://dx.doi.org/10.1088/0960-1317/17/6/R01>. – DOI 10.1088/0960-1317/17/6/R01
- [13] CHEN, Zhaohui ; LIU, Sheng: Simulation of copper electroplating fill process of through silicon via. In: *International Conference on Electronic Packaging Technology and High Density Packaging, ICEPT-HDP* (2010), Nr. 3, S. 433–437. <http://dx.doi.org/10.1109/ICEPT.2010.5583828>. – DOI 10.1109/ICEPT.2010.5583828. ISBN 9781424481422
- [14] CONNORS, Kenneth: *Chemical Kinetics: The Study of Reaction Rates in Solution*. VCH Publishers, 1990. – ISBN 978-0-471-72020-1
- [15] DAMBROWSKY, Nina: *Goldgalvanik in der Mikrosystemtechnik*, Universität Karlsruhe, PhD Thesis, 2007. – 122 S.
- [16] DAVID, C. ; BRUDER, J. ; ROHBECK, T. ; GRU, C ; KOTTLER, C. ; DIAZ, A. ; BUNK, O. ; PFEIFFER, F. ; GRÜNZWEIG, C.: Fabrication of diffraction gratings for hard X-ray phase contrast imaging. In: *Microelectronic Engineering* 84 (2007), may, Nr. 5-8, 1172–1177. <http://dx.doi.org/10.1016/j.mee.2007.01.151>. – DOI 10.1016/j.mee.2007.01.151. – ISSN 01679317
- [17] DAVID, Christian ; NÖHAMMER, B. ; SOLAK, H. H. ; ZIEGLER, E.: Differential x-ray phase contrast imaging using a shearing interferometer. In: *Applied Physics Letters* 81 (2002), Nr. 17, 3287–3289. <http://dx.doi.org/10.1063/1.1516611>. – DOI 10.1063/1.1516611. – ISSN 00036951

- [18] DENTINGER, Paul M. ; KRAFCIK, Karen L. ; SIMISON, Kelby L. ; JANEK, Richard P. ; HACHMAN, John: High aspect ratio patterning with a proximity ultraviolet source. In: *Microelectronic Engineering* 61-62 (2002), S. 1001–1007. [http://dx.doi.org/10.1016/S0167-9317\(02\)00491-4](http://dx.doi.org/10.1016/S0167-9317(02)00491-4). – DOI 10.1016/S0167-9317(02)00491-4. ISBN 0167-9317
- [19] DESTA, Yohannes M.: *Fabrication of high Aspect Ratio vibrating Cylinder Microgyroscope structures by use of the LIGA process*, Louisiana State University, Diss., 2005. – 163 S.
- [20] DRESE, Klaus S.: Design Rules for Electroforming in the LIGA Process. In: *Journal of The Electrochemical Society* 151 (2004), jun, Nr. 6, S. D39–D45. <http://dx.doi.org/10.1149/1.1739220>. – DOI 10.1149/1.1739220
- [21] EINSTEIN, A.: Über die von der molekularkinetischen Theorie der Wärme geforderte Bewegung von in ruhenden Flüssigkeiten suspendierten Teilchen. In: *Analen der Physik* 17 (1905), S. 549–560
- [22] ENGELHARDT, Martin ; KOTTLER, Christian ; BUNK, Oliver ; DAVID, Christian ; SCHROER, Christian G. ; BAUMANN, Joachim ; SCHUSTER, Manfred ; PFEIFFER, Franz: The fractional Talbot effect in differential x-ray phase-contrast imaging for extended and polychromatic x-ray sources. In: *Journal of Microscopy* 232 (2008), Nr. 1, S. 145–157. <http://dx.doi.org/10.1111/j.1365-2818.2008.02072.x>. – DOI 10.1111/j.1365-2818.2008.02072.x. – ISSN 1365-2818
- [23] FENG, Ru ; FARRIS, Richard J.: The characterization of thermal and elastic constants for an epoxy photoresist SU8 coating. In: *Journal of Materials Science* 37 (2002), S. 4793–4799. <http://dx.doi.org/10.1023/A:1020862129948>. – DOI 10.1023/A:1020862129948

- [24] FENG, Ru ; FARRIS, Richard J.: Influence of processing conditions on the thermal and mechanical properties of SU8 negative photoresist coatings. In: *Journal of Micromechanics and Microengineering* 13 (2003), jan, Nr. 1, S. 80–88. <http://dx.doi.org/10.1088/0960-1317/13/1/312>. – DOI 10.1088/0960-1317/13/1/312. – ISSN 0960-1317
- [25] GALE, Robert ; PETER, M.D. ; LAX, Eric: *Radiation: What It Is, What You Need to Know*. New York, NY : Alfred A. Knopf., 2013. – ISBN 978-0307950208
- [26] GENOLET, Grégoire ; LORENZ, Hubert: UV-LIGA: From Development to Commercialization. In: *Micromachines* 5 (2014), Nr. 3, S. 486–495. <http://dx.doi.org/10.3390/mi5030486>. – DOI 10.3390/mi5030486. – ISSN 2072-666X
- [27] GOETTERT, Jost ; LEMKE, Stephanie ; RUDOLPH, I. ; SELIGER, T. ; LOECHEL, B.: Soft X-Ray Lithography for High-Aspect Ratio Sub-Micrometer Structures. In: *Nanotechnology*. Santa Clara, CA, 2012. – ISBN 978-1-4665-6275-2, S. 188–191
- [28] GOGOLEWSKI, S. ; PENNINGS, A. J.: Crystallization of polyamides under elevated pressure. In: *Polymer* 118 (1977), Nr. 7, 647–666. Gogol1977
- [29] GRIFFITHS, S. K. ; CROWELL, J. A. W. ; KISTLER, B. L. ; DRYDEN, A. S.: Dimensional errors in LIGA-produced metal structures due to thermal expansion and swelling of PMMA. In: *Journal of Micromechanics and Microengineering* 14 (2004), Nr. 11, 1548–1557. <http://dx.doi.org/10.1088/0960-1317/14/11/017>. – DOI 10.1088/0960-1317/14/11/017
- [30] GRUND, Thomas ; KENNTNER, Johannes ; LAST, Arndt ; MOHR, Jürgen ; SIMON, Markus ; NAZMOV, Vladimir: *Resiststruktur zur Herstellung einer röntgenoptischen Gitterstruktur*. 2012

- [31] GUERIN, L. J. ; BOSSEL, M ; DEMIERRE, M ; CALMES, S ; RENAUD, P: Simple and low cost fabrication of embedded micro-channels by using a new thick-film photoplastic. In: *Solid State Sensors and Actuators*, 1997 Bd. 2, 1997, S. 1419–1422 vol.2
- [32] GUREYEV, Timur E. ; NESTERETS, Yakov I. ; STEVENSON, Andrew W. ; MILLER, Peter R. ; POGANY, Andrew ; WILKINS, Stephen W.: Some simple rules for contrast, signal-to-noise and resolution in in-line x-ray phase-contrast imaging. In: *Optics express* 16 (2008), Nr. 5, S. 3223–3241. <http://dx.doi.org/10.1364/OE.16.003223>. – DOI 10.1364/OE.16.003223. – ISBN 1094–4087
- [33] HAMANN, Carl H. ; VIELSTICH, Wolf.: *Elektrochemie*. Weinheim : Wiley-VCH, 2005. – ISBN 9783527310685 3527310681
- [34] HERZEN, Julia: *A grating interferometer for materials science imaging at a second-generation synchrotron radiation source*, Universität Hamburg, PhD, 2010
- [35] HIPPEL, Alexander ; WILLNER, Marian ; HERZEN, Julia ; AUWETER, Sigrid D. ; CHABIOR, Michael ; MEISER, Jan ; ACHTERHOLD, Klaus ; MOHR, Jürgen ; PFEIFFER, Franz: Energy-resolved visibility analysis of grating interferometers operated at polychromatic X-ray sources. In: *Optics Express* 22 (2014), Nr. 25, 30394. <http://dx.doi.org/10.1364/OE.22.030394>. – DOI 10.1364/OE.22.030394. – ISSN 1094–4087
- [36] HOHEISEL, Martin: Review of medical imaging with emphasis on X-ray detectors. In: *Nuclear Instruments and Methods in Physics Research Section A: Accelerators, Spectrometers, Detectors and Associated Equipment* 563 (2006), Nr. 1, S. 215–224. <http://dx.doi.org/http://dx.doi.org/10.1016/j.nima.2006.01.123>. – DOI <http://dx.doi.org/10.1016/j.nima.2006.01.123>. – ISSN 0168–9002

- [37] HORKANS, Jean: Pulsed Potentiostatic Deposition of Gold from Solutions of the Au(I) Sulfite Complex. In: *Journal of The Electrochemical Society* 124 (1977), oct, Nr. 10, 1499. <http://dx.doi.org/10.1149/1.2133100>. – DOI 10.1149/1.2133100. – ISSN 00134651
- [38] HORKANS, Jean ; ROMANKIW, L. T.: Pulsed Potentiostatic Deposition of Gold from Solutions of the Au(I) Sulfite Complex. In: *Journal of The Electrochemical Society* 124 (1977), oct, Nr. 10, S. 1499–1505. <http://dx.doi.org/10.1149/1.2133100>. – DOI 10.1149/1.2133100. – ISSN 00134651
- [39] HUANG, Xing-Jiu ; YARIMAGA, Oktay ; KIM, Ju-Hyun ; CHOI, Yang-Kyu: Substrate surface roughness-dependent 3-D complex nanoarchitectures of gold particles from directed electrodeposition. In: *Journal of Materials Chemistry* 19 (2009), dec, Nr. 4, S. 478. <http://dx.doi.org/10.1039/b816835k>. – DOI 10.1039/b816835k. – ISSN 0959-9428
- [40] HULL, R.O.: Current Density Range Characteristics, their Determination and Application. In: *Proceedings of the American Electroplaters Society* 27 (1939)
- [41] *Kapitel 2*. In: JACKSON, Mark J.: *Microfabrication Using X-ray Lithography*. First. Boston, MA : Springer US, 2007. – ISBN 978-0-387-26132-4, S. 55–98
- [42] JERJEN, Iwan ; REVOL, Vincent ; KOTTLER, Christian ; KAUFMANN, Rolf ; URBAN, Claus ; LUETHI, Thomas ; SENNHAUSER, Urs: The Benefits and Challenges of Differential Phase Contrast Imaging for Material Science. In: *International Symposium on Digital Industrial Radiology and Computed Tomography*. Berlin : DGZfP, 2011, 1–8
- [43] JOSELL, D. ; MOFFAT, T. P.: Superfilling Damascene Trenches with Gold in a Sulfite Electrolyte. In: *Journal of the Electrochemical Society* 160 (2013), apr, Nr. 12, D3009–D3014. <http://dx.doi.org/>

- 10.1149/2.003312jes. – DOI 10.1149/2.003312jes. – ISSN 0013–4651
- [44] KELLER, Stephan ; BLAGOI, Gabriela ; LILLEMÖSE, Michael ; HAEFLIGER, Daniel ; BOISEN, Anja: Processing of thin SU-8 films. In: *Journal of Micromechanics and Microengineering* 18 (2008), dec, Nr. 12, S. 125020. <http://dx.doi.org/10.1088/0960-1317/18/12/125020>. – DOI 10.1088/0960-1317/18/12/125020. ISBN 0960-1317
- [45] KENNTNER, Johannes: *Herstellung von Gitterstrukturen mit Aspektverhältnis 100 für die Phasenkontrastbildgebung in einem Talbot-Interferometer*. Karlsruhe, Karlsruher Institut für Technologie (KIT), PhD Thesis, 2013. – 214 S
- [46] KOCH, F. ; MARSCHALL, F. ; MEISER, J. ; MÁRKUS, O. ; FAISAL, A. ; SCHRÖTER, T. ; MEYER, P. ; KUNKA, D. ; LAST, A. ; MOHR, J.: Increasing the aperture of x-ray mosaic lenses by freeze drying. In: *Journal of Micromechanics and Microengineering* 25 (2015), Nr. 7, S. 75015. <http://dx.doi.org/10.1088/0960-1317/25/7/075015>. – DOI 10.1088/0960-1317/25/7/075015
- [47] KOCH, Frieder: *X-ray optics made by X-ray lithography: Process optimization and quality control*, Karlsruher Institut fuer Technologie, Diss., 2017
- [48] KUNKA, Danays ; MOHR, Jürgen ; NAZMOV, Vladimir ; MEISER, Jan ; MEYER, Pascal ; AMBERGER, Maximilian ; KOCH, Frieder ; SCHULZ, Joachim ; WALTER, Marco ; DUTTENHOFER, Thomas ; VOIGT, Anja ; AHRENS, Gisela ; GRÜTZNER, Gabi: Characterization method for new resist formulations for HAR patterns made by X-ray lithography. In: *Microsystem Technologies* 20 (2014), Nr. 10, S. 2023–2029. <http://dx.doi.org/10.1007/s00542-013-2055-x>. – DOI 10.1007/s00542-013-2055-x. – ISSN 1432-1858

- [49] LABIANCA, N. ; DELORME, J.: High Aspect ratio resist for thick film applications. In: *Proceedings of the SPIE* 2438 (1995), S. 846–852
- [50] LAU, E.: Beugungserscheinungen an Doppelrastern. In: *Annalen der Physik* 437 (1948), Nr. 7-8, S. 417–423. <http://dx.doi.org/10.1002/andp.19484370709>. – DOI 10.1002/andp.19484370709
- [51] LEMKE, Stephanie: *Charakterisierung modifizierter Negativresiste für die Röntgentiefenlithographie*, Technische Universität Berlin, Diss., 2011. – 163 S.
- [52] LISINENKOVA, M.: *Megaschallunterstützter Stofftransport in LIGA-Mikrostrukturen*, Universität Karlsruhe (TH), Diss., 2008
- [53] LORENZ, Hubert ; DESPONT, M. ; FAHRNI, M. ; LABIANCA, N. ; VETTIGER, P. ; RENAUD, P.: SU-8: a low-cost negative resist for MEM. In: *Journal of Micromechanics and Microengineering* 7 (1997), Nr. 3, S. 121–124. <http://dx.doi.org/10.1088/0960-1317/7/3/010>. – DOI 10.1088/0960-1317/7/3/010
- [54] LORENZ, Hubert ; DESPONT, M. ; FAHRNI, N. ; BRUGGER, J. ; VETTIGER, P. ; RENAUD, P.: High-aspect-ratio, ultrathick, negative-tone near-UV photoresist and its applications for MEMS. In: *Sensors and Actuators A: Physical* 64 (1998), jan, Nr. 1, S. 33–39. [http://dx.doi.org/10.1016/S0924-4247\(98\)80055-1](http://dx.doi.org/10.1016/S0924-4247(98)80055-1). – DOI 10.1016/S0924-4247(98)80055-1. – ISSN 09244247
- [55] MADOU, Marc J.: *Fundamentals of Microfabrication: The Science of Miniaturization*. 2nd. CRC Press, 2002. – 757 S. – ISBN 0849308267
- [56] MARSCHALL, Felix: *Entwicklung eines Röntgenmikroskops für Photonenergien von 15 keV bis 30 keV*, Karlsruher Institut fuer Technologie (KIT), Diss., 2014. <http://dx.doi.org/10.5445/KSP/1000043064>. – DOI 10.5445/KSP/1000043064. – 126 S

- [57] MARSCHNER, M ; BIRNBACHER, Lorenz ; MECHLEM, K ; NOICHL, W ; FEHRINGER, A ; WILLNER, M ; SCHERER, K ; HERZEN, Julia ; NOËL, P B. ; PFEIFFER, Franz: Two-shot X-ray dark-field imaging. In: *Opt. Express* 24 (2016), nov, Nr. 23, S. 27032–27045. <http://dx.doi.org/10.1364/OE.24.027032>. – DOI 10.1364/OE.24.027032
- [58] MEISER, Jan: *Großflächige Röntgengitter*, Karlsruher Institut für Technologie, Diss., 2016. <http://dx.doi.org/10.5445/IR/1000073592>. – DOI 10.5445/IR/1000073592. – 106 S.
- [59] MEISER, Jan ; WILLNER, Marian ; SCHRÖTER, Tobias ; HOFMANN, A. ; RIEGER, Jens ; KOCH, F. ; BIRNBACHER, Lorenz ; SCHÜTLER, Markus ; KUNKA, Danays ; MEYER, Pascal ; FAISAL, A. ; AMBERGER, Maximilian ; DUTTENHOFER, T. ; WEBER, T. ; HIPPEL, Alexander ; EHN, S. ; WALTER, Marco ; HERZEN, Julia ; SCHULZ, Joachim ; PFEIFFER, Franz ; MOHR, Jürgen: Increasing the field of view in grating based X-ray phase contrast imaging using stitched gratings. In: *Journal of X-Ray Science and Technology* 24 (2016), Nr. 3, S. 379–388. <http://dx.doi.org/10.3233/XST-160552>. – DOI 10.3233/XST-160552
- [60] MICROCHEM: SU-8 3000 Permanent Epoxy. In: *Product Datasheet* 20 (2000). <http://dx.doi.org/10.1146/annurev.matsci.28.1.153>. – DOI 10.1146/annurev.matsci.28.1.153. – ISBN 008466000846600
- [61] MICROCHEMICALS: *Electroplating with Photoresist Masks*. 2014
- [62] MOHR, J ; LAST, A ; NAZMOV, V ; SIMON, M ; GRUND, T ; KENNTNER, J: *Resist structure for producing an x-ray optical grating structure*. 2012
- [63] MOHR, Jürgen ; EHRFELD, W. ; MÜNCHMEYER, D. ; STUTZ, A.: Requirements on resist layers in deep-etch synchrotron radiation lithog-

- raphy. In: *Journal of Vacuum Science and Technology* B6 (1988), Nr. 6, S. 2264–2267
- [64] MOMOSE, Atsushi: Recent Advances in X-ray Phase Imaging. In: *Japanese Journal of Applied Physics* 44 (2005), Nr. 9A, S. 6355–6367. <http://dx.doi.org/10.1143/JJAP.44.6355>. – DOI 10.1143/JJAP.44.6355. ISBN 0021–4922
- [65] MOMOSE, Atsushi: Development toward high-resolution X-ray phase imaging. In: *Microscopy* 66 (2017), Nr. 3, S. 155. <http://dx.doi.org/10.1093/jmicro/dfx013>. – DOI 10.1093/jmicro/dfx013
- [66] NISHI, Yoshio (Hrsg.) ; DOERING, Robert (Hrsg.): *Handbook of Semiconductor Manufacturing Technology*. Second Edi. CRC Press, 2007. – 1720 S. – ISBN 9781574446753
- [67] NORDT, Sawa: *Analytik von Novolak-Epoxidharzen für die Resistentwicklung in der Mikrosystemtechnik*, Technische Universität Darmstadt, PhD Thesis, 2010. <http://tuprints.ulb.tu-darmstadt.de/2361/1/Dissertation{ }SawaNordt.pdf>. – 116 S.
- [68] OCCHIALINI, J. M. ; HIGDON, J. J. L.: Convective Mass Transport from Rectangular Cavities in Viscous Flow. In: *Journal of The Electrochemical Society* 139 (1992), oct, Nr. 10, 2845–2855. <http://dx.doi.org/10.1149/1.2068991>. – DOI 10.1149/1.2068991. – ISSN 00134651
- [69] PAUL, Steele: NHS Imaging and Radiodiagnostic activity in England / National Health Service of England. Version: 2013. <https://www.england.nhs.uk/statistics/wp-content/uploads/sites/2/2013/04/KH12-release-2012-13.pdf>. 2013. – Forschungsbericht. – 1–6 S.
- [70] PAUNOVIC, Milan ; SCHLESINGER, Mordechay: *Fundamentals of Electrochemical Deposition*. Bd. 5. 2006. – 49 S. <http://>

- [//dx.doi.org/2005058421](http://dx.doi.org/2005058421). <http://dx.doi.org/2005058421>.  
– ISBN 9780471712213
- [71] PFEIFFER, F ; BECH, M ; BUNK, O ; KRAFT, P ; EIKENBERRY, E F ; BRÖNNIMANN, Ch ; GRÜNZWEIG, C ; DAVID, C: Hard-X-ray dark-field imaging using a grating interferometer. In: *Nature materials* 7 (2008), feb, Nr. 2, 134–7. <http://dx.doi.org/10.1038/nmat2096>. – DOI 10.1038/nmat2096. – ISSN 1476–1122
- [72] PFEIFFER, Franz ; WEITKAMP, Timm ; BUNK, Oliver ; DAVID, Christian: Phase retrieval and differential phase-contrast imaging with low-brilliance X-ray sources. In: *Nature Physics* 2 (2006), mar, Nr. 4, 258–261. <http://dx.doi.org/10.1038/nphys265>. – DOI 10.1038/nphys265. – ISSN 1745–2473
- [73] PONCE, Daniel R. ; LOZANO, Karen ; EUBANKS, Thomas ; HARB, Ahmad ; FERRER, Domingo ; LIN, Yuankun: Thermophysical Analysis of SU8-Modified Microstructures Created by Visible Light Lithography. In: *Journal of Polymer Science: Part B: Polymer Physics* 48 (2010), S. 47–54. <http://dx.doi.org/10.1002/POLB>. – DOI 10.1002/POLB
- [74] RICHTON, J. ; AHZI, S. ; VECCHIO, K.S. ; JIANG, F.C. ; ADHARAPURAPU, R.R.: Influence of temperature and strain rate on the mechanical behavior of three amorphous polymers: Characterization and modeling of the compressive yield stress. In: *International Journal of Solids and Structures* 43 (2006), apr, Nr. 7-8, 2318–2335. <http://dx.doi.org/10.1016/j.ijso1str.2005.06.040>. – DOI 10.1016/j.ijso1str.2005.06.040. – ISSN 00207683
- [75] ROBIN, C. J. ; VISHNOI, Aakansha ; JONNALAGADDA, Krishna N.: Mechanical Behavior and Anisotropy of Spin-Coated SU-8 Thin Films for MEMS. In: *Journal of Microelectromechanical Systems* (2013), Nr. 5. <http://dx.doi.org/10.1109/JMEMS.2013.2264341>. – DOI 10.1109/JMEMS.2013.2264341

- [76] ROENTGEN, Wilhem C.: Ueber eine neue Art von Strahlen. In: *Aus den Sitzungsberichten der Wuerzburger Physik.-med. Gesellschaft* (1895)
- [77] ROMANKIW, L T.: A path : from electroplating through lithographic masks in electronics to LIGA in MEMS. In: *Electrochimica Acta* 42 (1997), Nr. 20-22, S. 2985–3005. [http://dx.doi.org/10.1016/S0013-4686\(97\)00146-1](http://dx.doi.org/10.1016/S0013-4686(97)00146-1). – DOI 10.1016/S0013-4686(97)00146-1. – ISSN 00134686
- [78] RUEBEL, Susanne ; STUEMKE, Manfred: ( 19 ) *United States* ( 12 ) *Patent Application Publication* ( 10 ) *Pub . No .: US 2010 / 0041620 A1 Publication Classi ? cation 6 Weak Followup Patent Application Publication*. 2004
- [79] SCHLESINGER, Mordechay ; SCHLESINGER, Mordechay [ . (Hrsg.): *Modern electroplating*. 5. ed. Hoboken, NJ : Wiley, 2010 (The ECS series of texts and monographs ; 52). – ISBN 978-0-470-16778-6
- [80] SCHMID, S ; KÜHNE, S ; HIEROLD, C: Influence of air humidity on polymeric microresonators. In: *Journal of Micromechanics and Microengineering* 19 (2009), jun, Nr. 6, S. 065018. <http://dx.doi.org/10.1088/0960-1317/19/6/065018>. – DOI 10.1088/0960-1317/19/6/065018. – ISSN 0960-1317
- [81] SCHMUKI, Patrik (Hrsg.) ; SANNAKAISA, Virtanen (Hrsg.): *Electrochemistry at the Nanoscale*. Springer. <http://dx.doi.org/10.1007/978-0-387-73582-5>. <http://dx.doi.org/10.1007/978-0-387-73582-5>. – ISBN 978-0-387-73581-8
- [82] SCHRÖTER, Tobias J. ; KOCH, Frieder ; MEYER, Pascal ; BAUMANN, Martin ; MÜNCH, Daniel ; KUNKA, Danays ; ENGELHARDT, Sabine ; ZUBER, Marcus ; BAUMBACH, Tilo ; MOHR, Jürgen: Large area gratings by x-ray LIGA dynamic exposure for x-ray phase-contrast imaging. In: *Journal of Micro/Nanolithography, MEMS, and MOEMS* 16

- (2017), Nr. 1, S. 13501. <http://dx.doi.org/10.1117/1.JMM.16.1.013501>. – DOI 10.1117/1.JMM.16.1.013501. ISBN 1932–5150
- [83] SCHÜTZ, Antje: *Untersuchungen zum Einsatz des Negativresistmaterials SU-8 in der LIGA-Technik*, Technische Universität Berlin, PhD, 2004. <http://opus4.kobv.de/opus4-tuberlin/frontdoor/index/index/docId/724>. – 1–105 S.
- [84] SIMON, Markus: *Röntgenlinsen mit großer Apertur*, Karlsruher Institut für Technologie, Diss., 2010. – 101 S
- [85] *Kapitel 8*. In: STROBL, Gert R.: *Deformation, Yielding and Fracture*. Berlin, Heidelberg : Springer Berlin Heidelberg, 2007. – ISBN 978–3–540–68411–4, S. 415–461
- [86] TALBOT, H. F.: Facts relating to optical science. In: *Philosophical Magazine Series 3 9* (1836), Nr. 56, S. 401–407. <http://dx.doi.org/10.1080/14786443608649032>. – DOI 10.1080/14786443608649032
- [87] TEUTSCH, Michael: *Entwicklung von Hochtemperatur-MEMS-Anwendungen*, Karlsruher Institut für Technologie (KIT), Diss., 2013
- [88] THUERING, T ; STAMPANONI, M: Performance and optimization of X-ray grating interferometry. In: *Philosophical transactions. Series A, Mathematical, physical, and engineering sciences* 372 (2014), Nr. 2010, S. 20130027. <http://dx.doi.org/10.1098/rsta.2013.0027>. – DOI 10.1098/rsta.2013.0027. – ISSN 1364–503X
- [89] TIAN, Furong ; BONNIER, Franck ; CASEY, Alan ; SHANAHAN, Anne E. ; BYRNE, Hugh J.: Surface enhanced Raman scattering with gold nanoparticles: effect of particle shape. In: *Anal. Methods* 6 (2014), Nr. 22, 9116–9123. <http://dx.doi.org/10.1039/C4AY02112F>. – DOI 10.1039/C4AY02112F

- [90] WEITKAMP, Timm ; DAVID, Christian ; KOTTLER, Christian ; BUNK, Oliver ; PFEIFFER, Franz: Tomography with grating interferometers at low-brilliance sources. In: *Proc. SPIE 6318, Developments in X-Ray Tomography V* Bd. 6318. San Diego, 2006, S. 63180S–63180S–10
- [91] WEITKAMP, Timm ; DIAZ, Ana ; DAVID, Christian ; PFEIFFER, Franz ; STAMPANONI, Marco ; CLOETENS, Peter ; ZIEGLER, Eric: X-ray phase imaging with a grating interferometer. In: *Optics express* 13 (2005), S. 6296–6304. <http://dx.doi.org/10.1364/OPEX.13.006296>. – DOI 10.1364/OPEX.13.006296. ISBN 1094–4087
- [92] WILLNER, Marian S.: *Quantitative phase-contrast computed tomography for biomedical applications*, Technische Universität München, Diss., 2017
- [93] WOUTERS, K. ; PUERS, R.: Accurate measurement of the steady-state swelling behavior of SU-8 negative photo resist. In: *Procedia Chemistry* 1 (2009), Nr. 1, 60–63. <http://dx.doi.org/10.1016/j.proche.2009.07.015>. – DOI 10.1016/j.proche.2009.07.015
- [94] WOUTERS, K. ; PUERS, R.: Diffusing and swelling in SU-8: insight in material properties and processing. In: *Journal of Micromechanics and Microengineering* 20 (2010), sep, Nr. 9, 095013. <http://dx.doi.org/10.1088/0960-1317/20/9/095013>. – DOI 10.1088/0960–1317/20/9/095013. – ISSN 0960–1317
- [95] YAROSHENKO, Andre ; BECH, Martin ; POTDEVIN, Guillaume ; MALECKI, Andreas ; BIERNATH, Thomas ; WOLF, Johannes ; TAPFER, Arne ; SCHÜTTLER, Markus ; MEISER, Jan ; KUNKA, Danays ; AMBERGER, Maximilian ; MOHR, Juergen ; PFEIFFER, Franz: Non-binary phase gratings for x-ray imaging with a compact Talbot interferometer. In: *Optics Express* 22 (2014), Nr. 1, S. 547. <http://dx.doi.org/10.1364/OE.22.000547>. – DOI 10.1364/OE.22.000547. ISBN 1094–4087

- [96] ZERNIKE, F: Phase contrast, a new method for the microscopic observation of transparent objects. In: *Physica* 9 (1942), Nr. 7, S. 686–698. [http://dx.doi.org/10.1016/S0031-8914\(42\)80035-X](http://dx.doi.org/10.1016/S0031-8914(42)80035-X). – DOI 10.1016/S0031-8914(42)80035-X. – ISSN 0031-8914
- [97] ZHOU, Wu ; PENG, Bei ; YU, Hui J. ; HE, Xiao P. ; DU, Lian M. ; PENG, Peng: The Influence of Die-Attach Adhesives on the Packaging of MEMS Accelerometer. In: *Micro-Nano Technology XVI* Bd. 645, Trans Tech Publications, 2015 (Key Engineering Materials), S. 533–537